CHAPTER 5

LOW TEMPERATURE – CONDENSED MATTER PHYSICS

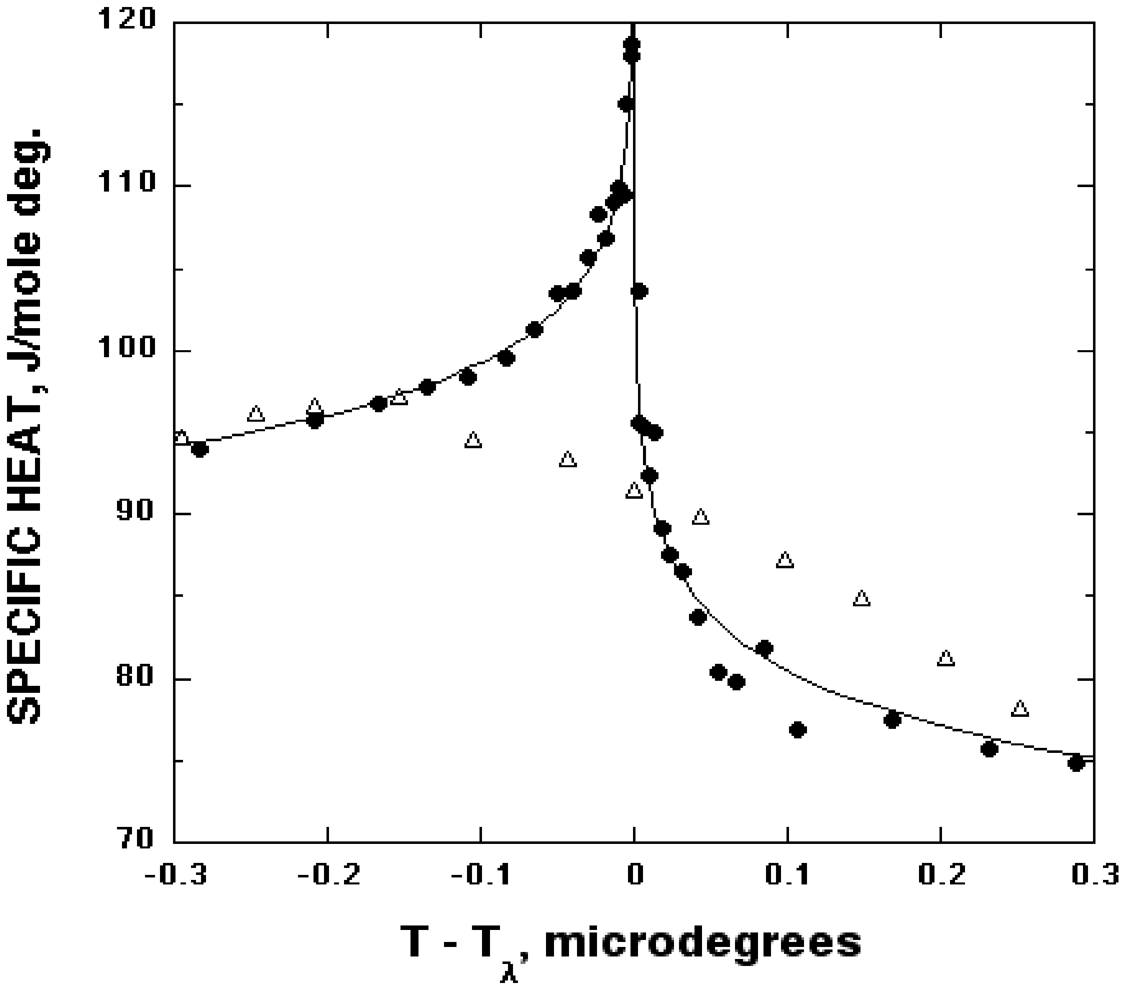

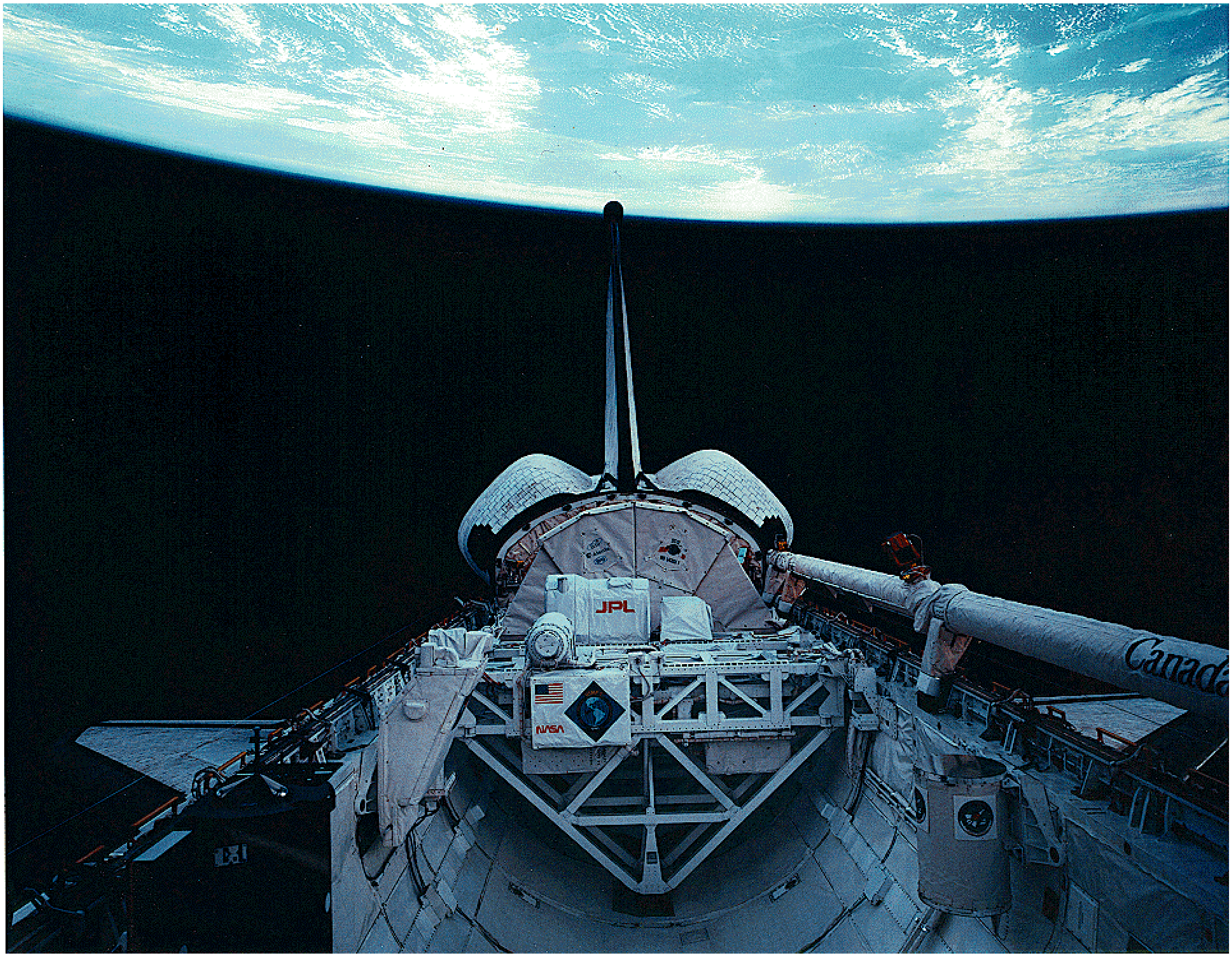
JPL
NASA
Canada

Progress in the Development of the MISTE Flight Experiment

M. Barmatz, Inseob Hahn and F. Zhong

Jet Propulsion Laboratory, California Institute of Technology
4800 Oak Grove Drive, Pasadena, CA 91109

The MISTE flight experiment plans to measure the specific heat at constant volume, C_V, and isothermal susceptibility, χ_T, near the ^{3}He liquid-gas critical point. Precision ground-based experiments have been performed in the crossover region away from the critical point in preparation for this flight. A new method for precisely determining the critical temperature is being evaluated and will be presented. A sweep electrostriction method was also demonstrated for obtaining the isothermal susceptibility close to the critical point. We have been able to demonstrate that the chemical potential can be obtained from these electrostriction measurements. Pressure versus density measurements along isotherms below the critical temperature were performed to determine the isothermal susceptibility along the coexistence curve. These measurements are compared to susceptibility data obtained along the critical isochore above the transition.

1. INTRODUCTION

The MISTE flight experiment plans to perform heat capacity at constant volume, C_V, isothermal susceptibility, χ_T, and PVT measurements in the same experimental cell near the liquid-gas critical point of ^{3}He. These experiments, performed in a microgravity environment, will provide measurements in the asymptotic region two decades in reduced temperature closer to the transition than obtained on earth. The fluctuation-induced constant-volume heat capacity along the critical isochore and the isothermal susceptibility along the critical isochore and coexistence curve are expected to satisfy the following theoretical expressions:

$$\begin{aligned} C_V^{\pm *} &= (T_c \rho_c / P_c) C_V^{\pm} \\ &= A_0^{\pm} |t|^{-\alpha} [1 + A_1^{\pm} |t|^{\Delta_s} + ...] + B_{\mathrm{cr}}, \end{aligned} \tag{1}$$

$$\begin{aligned} \chi_T^{\pm *} &= (P_c / \rho_c^2) \chi_T^{\pm} \\ &= \Gamma_0^{\pm} |t|^{-\gamma} [1 + \Gamma_1^{\pm} |t|^{\Delta_s} + ...], \end{aligned} \tag{2}$$

where $\alpha \simeq 0.11$ and $\gamma \simeq 1.24$ are universal critical exponents and $A_0^{\pm}$ and $\Gamma_0^{\pm}$ are system-dependent critical amplitudes. The superscripts "+" and "–" correspond to positive and negative reduced temperatures $t \equiv (T - T_{\mathrm{c}})/T_{\mathrm{c}}$, respectively. The isothermal susceptibility along the coexistence curve is given by χ_T^{-*}. The system-dependent critical parameters are T_c, ρ_c, and P_c, and B_{cr} is a fluctuation-induced, constant term. The confluent singularity expansion in the brackets includes an independent universal correction-to-scaling exponent,[1] $\Delta_s = 0.52 \pm 0.02$ and system-dependent amplitudes $A_1^{\pm}$ and $\Gamma_1^{\pm}$. Analytic background terms must also be included in analyzing heat-capacity measurements.

Critical phenomena theories can predict critical exponents and universal amplitude ratios. However, an exact determination of the asymptotic region cannot be made theoretically since the leading critical amplitudes and the amplitudes associated with correction-to-scaling confluent singularities are system dependent. The MISTE flight experiment should permit an accurate determination of the leading system-dependent asymptotic critical amplitudes for ^{3}He. A knowledge of these asymptotic amplitudes will permit a more accurate analysis of crossover measurements farther away from the transition. Ground-based studies are now being performed in the crossover region[2] in preparation for this future flight experiment. The results of some of these studies will be reported in this paper.

2. GROUND–BASED EXPERIMENTS

Ground-based measurements were performed in a flat pancake fluid cell shown in Fig. 1. The cell temperature was measured using a $\mathrm{GdCl_3}$ high resolution thermometer (HRT) with a sensitivity of ~ 1 nK near the ^{3}He critical point ($T_{\mathrm{c}} = 3.31$ K). The density sensor was a parallel plate capacitor situated half way between the top and bottom of the cell. The density was determined from the measurement of the dielectric constant using the Clausius-Mossotti equation. A Straty-Adams type pressure sensor was also situated at the midplane of the cell. This sensor consisted of a parallel plate

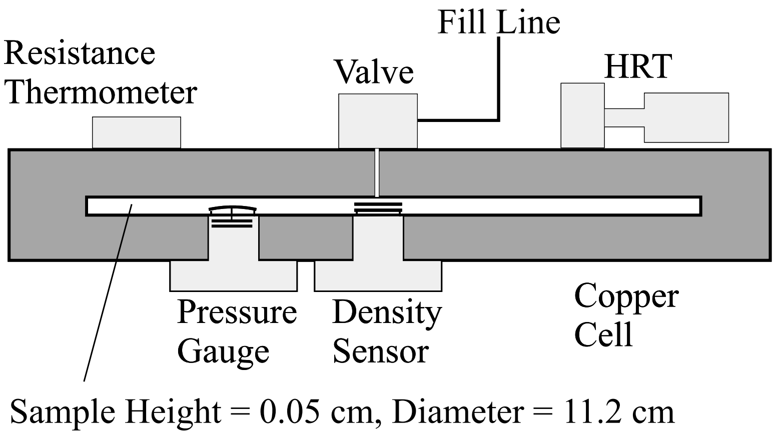

Fig. 1. Schematic of ground-based cell for measuring heat capacity and susceptibility.

capacitor with one plate attached to a flexible diaphragm that sensed pressure changes in the cell. This experimental configuration has the advantage that pressure, density, and temperature data can be simultaneously obtained in the same cell while heat capacity and susceptibility measurements were being performed.

The isothermal susceptibility, $\chi_T = \rho(\partial\rho/\partial P)_T$, was measured along isotherms both above and below the critical temperature. This was achieved by initially overfilling the cell and then slowly removing fluid from the cell and measuring the density and pressure as a function of time. Susceptibility data were obtained from the slope of P versus ρ curves in the reduced temperature range of $6 \times 10^{-5} < |t| < 10^{-1}$. The density of the susceptibility maximum approaches the critical density, ρ_c, as $T \rightarrow T_c$. After completing the susceptibility measurements, the low temperature valve was closed at the critical density. Heat-capacity measurements were then performed using a pulse technique in the single and two-phase regions over the range $5{\times}10^{-4} < |t| < 10^{-1}$. Drift heat-capacity measurements were also performed close to the transition. These new C_V and χ_T data agreed with earlier measurements from Horst Meyer's group[3–6] over the same temperature range of overlap.

3. Determination of the critical temperature

In order to successfully analyze experimental measurements near a critical point, it is important to determine the critical temperature as precisely

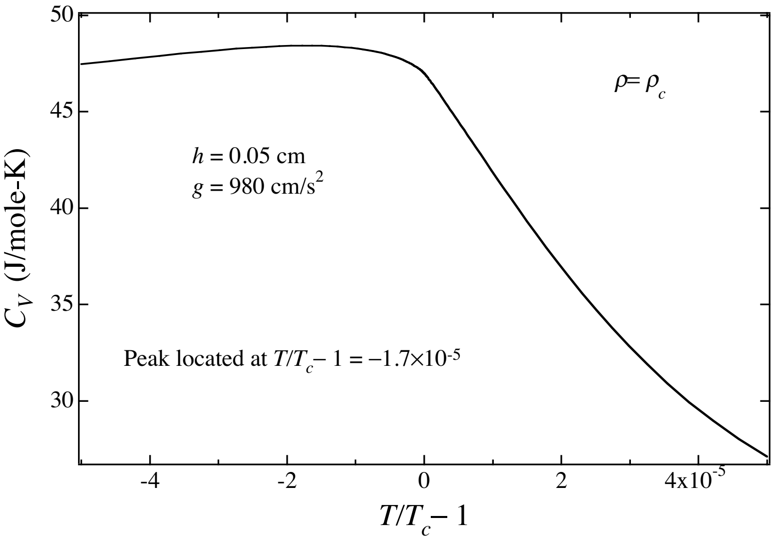

Fig. 2. Restricted cubic model prediction for the ^{3}He heat capacity in a 0.05 cm high cell along the critical isochore in 1g. A change in slope is predicted at the transition temperature.

as possible. There are several methods for finding T_c. One approach is to have T_c be a fitting parameter when analyzing data. However, the accuracy of the resultant T_c will depend on the model chosen and closeness of the data to the transition. We have used this approach with susceptibility measurements above the transition[7] to obtain $T_c = 3.315533\,\mathrm{K}$. This T_c will be used in analyzing the susceptibility measurements presented later in this paper. One can also attempt to use some characteristic signature of the transition. For example, it is known that the time constant for equilibrium in performing heat-capacity measurements is much greater in the two-phase region. Unfortunately, in ground-based measurements, the gravity induced density gradient smears out this sudden change near the transition.

We have recently been investigating a new slow-drift heat-capacity approach for determining the transition temperature. For experimental cells of small vertical height in a gravitational field, theory predicts an experimentally measurable change in the temperature derivative of C_V at T_c with a heat capacity maximum occurring in the two-phase region. Figure 2 shows the restricted cubic model[8] prediction for the ^{3}He heat capacity in our 0.05 cm high cell along the critical isochore in 1g. We see a change in slope occurring at the transition and a peak value located at a reduced temperature of $t \approx -1.7 \times 10^{-5}$ below T_c. Figure 3 shows an example of our experimental

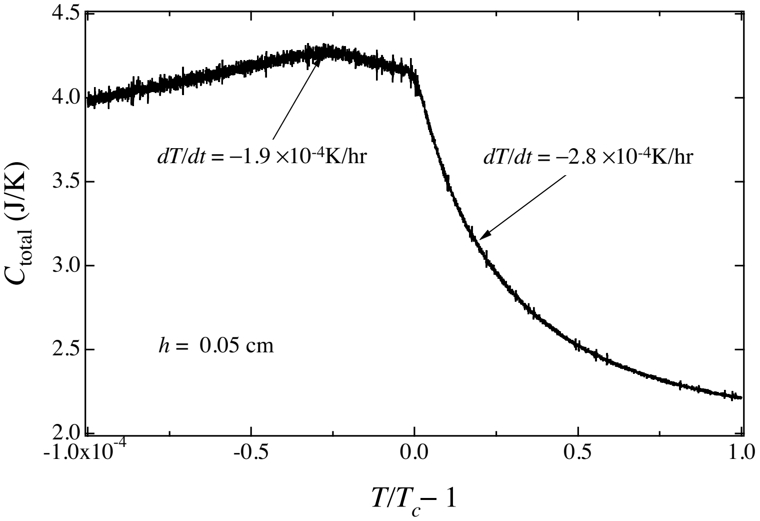

Fig. 3. Experimental determination of the transition temperature using the ^{3}He heat capacity anomaly along the critical isochore in 1g.

measurements performed during a slow drift down through the transition. There is a kink in the data that we associate with the transition temperature T_c. The transition temperature can be determined to better than $\pm 15\mu$K. The peak in these data is at $t \approx -2.3 \times 10^{-5}$, which is close to the theoretically predicted value. Additional measurements are planned at even slower drift rates to make sure we have this level of reproducibility in determining T_c.

4. Chemical potential

An electrostriction technique was previously developed[9] to perform susceptibility measurements within $t < 10^{-4}$. This technique is based on the fact that an electric field gradient can produce a pressure gradient within a dielectric fluid ($\delta P \propto E^2$) that in turn induces a density change. Our approach is to apply a dc voltage across a parallel plate capacitor to produce a uniform electric field within the density sensor capacitor gap. The density change $\delta\rho$ is obtained at several voltages and $\delta\rho/\delta P$ is determined in the limit of zero voltage. We have been evaluating drift electrostriction measurements using a fixed dc voltage across the gap. Figure 4 shows measurements of the density change between the applied dc voltage and zero dc voltage. The drift rates were $\approx -4 \times 10^{-4}$ K/hr. The susceptibility at any

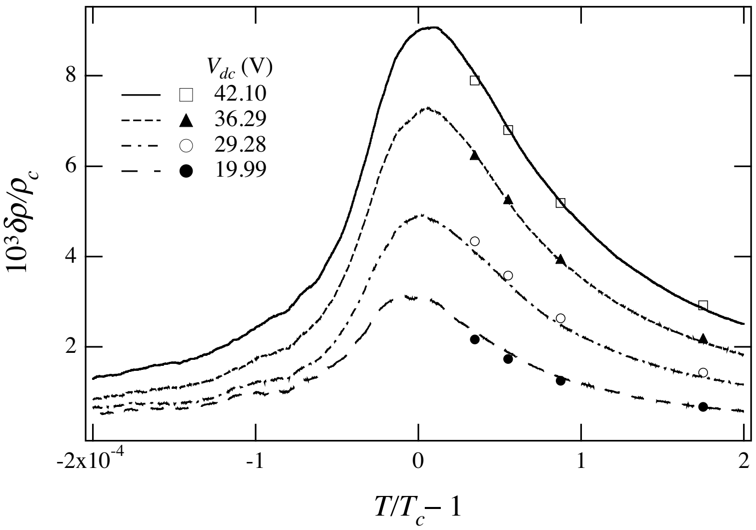

Fig. 4. Density change versus temperature for electrostriction drift (lines) and equilibrium (symbols) measurements at various constant applied dc bias voltages.

given temperature can be determined by extrapolating the density values obtained from these curves to zero dc voltage. We also performed equilibrium measurements, shown by symbols, at a few reduced temperatures to see if this drift rate was slow enough. Good agreement was obtained between the drift and equilibrium measurements down to about a reduced temperature of $t = 5 \times 10^{-5}$. The MISTE flight experiment plans to reach a reduced temperature of 10^{-6} that will require even slower drift rates.

We have realized that this electrostriction technique can be used to conveniently determine the chemical potential difference that can be written as $d\mu = -sdT + dP/\rho$. Under isothermal conditions the integration of this expression reduces to

$$\mu(\rho_2, T) - \mu(\rho_1, T) = \int_{P(\rho_1,T)}^{P(\rho_2,T)} dP/\rho\,, \tag{3}$$

where ρ_1 is the ambient density outside the capacitor gap and ρ_2 is the density inside the gap. Since the pressure gradient induced by an electric field gradient is given by

$$\nabla P = (\epsilon_0\rho/2)\nabla(E^2(\partial\epsilon/\partial\rho)), \tag{4}$$

we can write the chemical potential difference between two densities, Eq. (3),

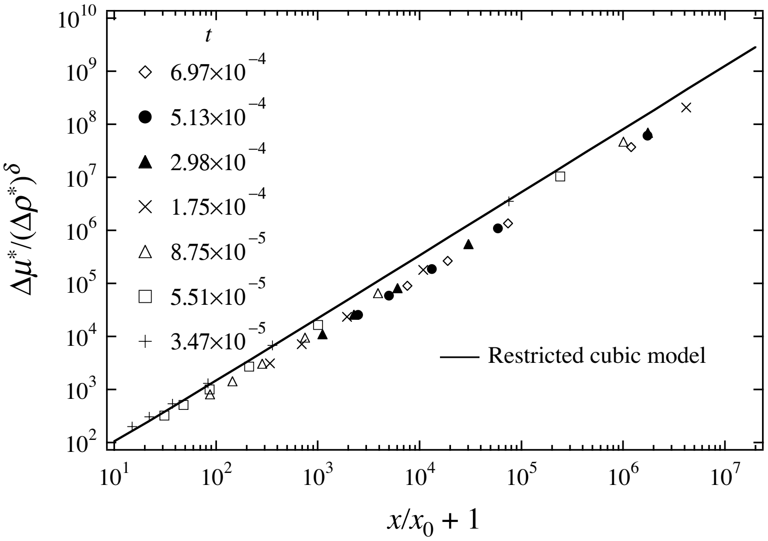

Fig. 5. Comparison of electrostriction measurements to theoretically predicted universal curve for the chemical potential.

as

$$\mu(\rho_2, T) - \mu(\rho_1, T) = (3\epsilon_0\zeta_c\rho_c/2(\rho_c - \zeta_c\rho_2)^2)E^2, \tag{5}$$

where $\zeta_c = 4\pi\alpha'/3$ with α' being the polarizability of the fluid.

In the asymptotic region, scaling theory predicts the chemical potential difference from its critical value can be scaled by a universal function h

$$(\mu^*(\rho, T) - \mu^*(\rho_c, T))/(\Delta\rho|\Delta\rho|^{\delta-1}) = Dh(x/x_0)\,, \tag{6}$$

where $\mu^* = (\rho_c/P_c)\mu$, $x = t/(|\Delta\rho|)^{1/\beta}$, and $x_0 = 1/B_0^{1/\beta}$. The reduced density $\Delta\rho \equiv \rho/\rho_c - 1$, and $\beta \simeq 0.326$ is the critical exponent and B_0 the critical amplitude that define the shape of the coexistence curve. D is the critical amplitude associated with the divergence of the pressure with density along the critical isotherm. By setting the ambient density ρ_1 equal to the critical density in Eq. (5), we obtain the following expression for the universal function h

$$Dh(x/x_0) = (3\epsilon_0\zeta_c\rho_c/2(\rho_c - \zeta_c\rho_2)^2)(E^2/(\Delta\rho)^\delta). \tag{7}$$

The right side of this equation can be determined experimentally since we measure the density ρ_2 and calculate $\Delta\rho$ and the electric field. Figure 5 is a plot of the universal curve. The solid line is the prediction from the restricted

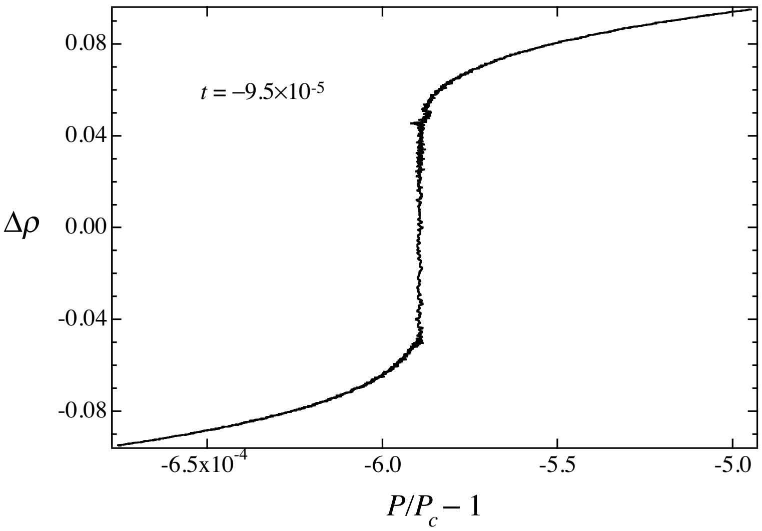

Fig. 6. Pressure versus density along an isotherm below T_c.

cubic model[8] and the data points come from equilibrium electrostriction measurements at various temperatures. We do not expect to have a good fit between theory and experiment since most of the data points are not in the asymptotic region. However, we anticipate a much more stringent test of this scaling theory prediction coming from the MISTE flight experiment where measurements will be performed much closer to the transition.

5. Susceptibility measurements

The isothermal susceptibility along the coexistence curve can also be obtained from pressure versus density measurements as stated above. Figure 6 shows an example of P versus ρ measurements at a reduced temperature of $t = -9.5 \times 10^{-5}$. The break in $(\partial\rho/\partial P)_T$ at a reduced density $\Delta\rho \approx 5\%$ indicates the onset of the two-phase region in which the pressure remains constant until the gas side of the coexistence curve is reached at $\Delta\rho \approx -5\%$. The susceptibility at the coexistence curve is obtained from the slope of this curve as it enters and exits the two-phase region. The coexistence curve densities at this temperature can also be determined to within ± 0.1% from such breaks in the slope. This method for determining the susceptibility and coexistence curve will become less precise as the transition is approached since the change in slope will be less pronounced.

The experimentally determined susceptibility along the critical isochore

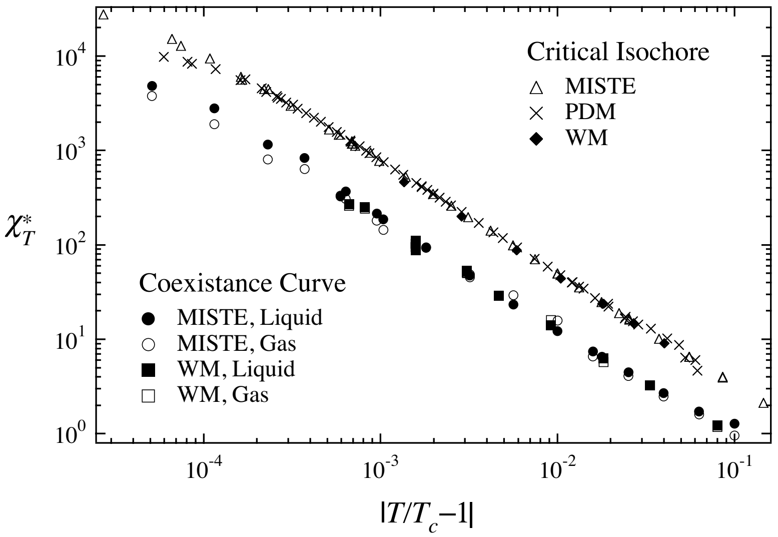

Fig. 7. Susceptibility measurements along the critical isochore above T_c and along the coexistence curve below T_c. Also included are the data from Wallace and Meyer (WM), and Pittman, Doiron and Meyer (PDM).

and coexistence curve are shown in Fig. 7. Earlier measurements from Wallace and Meyer[3], and Pittman, Doiron, and Meyer[4] have also been included. The MISTE measurements along the coexistence curve extend over a decade closer to the transition than the earlier data. We see good agreement between the various measurements in the regions of overlap. The susceptibility along the coexistence curve and critical isochore seem to have the same slope in this log-log plot, with the coexistence curve susceptibility having a smaller magnitude. To estimate the difference in magnitude between the susceptibility data above and below the transition, the critical isochore data were divided by 3.7 to approximately overlap the coexistence curve data. This is the same value used by Wallace and Meyer in their earlier work.[3] These normalized data are shown in Fig. 8. It is surprising to see that all the data sets are consistent with each other over three decades in reduced temperature. This factor of 3.7 can be considered as an effective ratio of the critical amplitudes $(\Gamma_0^+/\Gamma_0^-)_{\text{eff}}$ in the crossover region. Critical phenomena theories[10] predict a ratio $\Gamma_0^+/\Gamma_0^- = 4.95$ in the asymptotic region. Since most of these ground-based susceptibility data are outside the asymptotic region, additional measurements from the MISTE flight experiment are needed closer to the transition to test this theoretical asymptotic prediction and to obtain a better understanding of the observed crossover behavior.

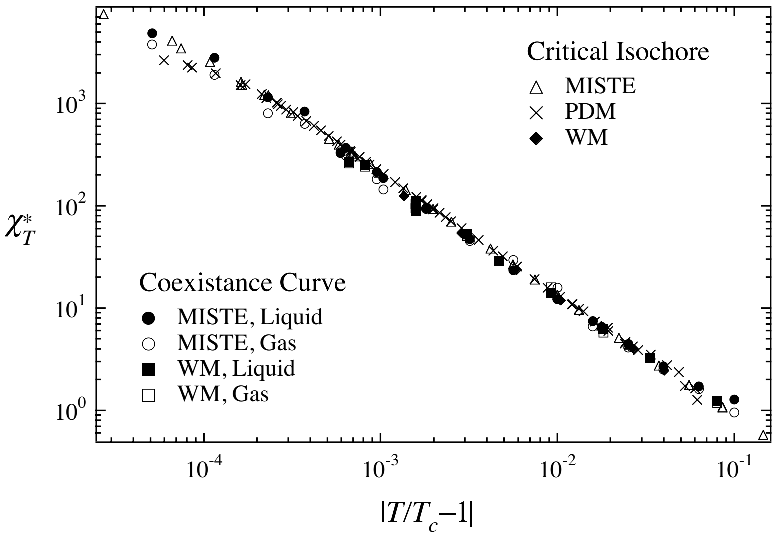

Fig. 8. Normalized susceptibility measurements. Critical isochore data above T_c in Fig. 7 were divided by 3.7 to overlay on coexistence data below T_c.

6. FUTURE STUDIES

The recent heat capacity and susceptibility measurements need to be analyzed using accurate theoretical crossover models in order to obtain a better understanding of thermodynamic behavior farther away from the transition. We began this process by analyzing our susceptibility data along the critical isochore above the transition using a field-theoretical Renormalization-Group ϕ^4 approach[11] recently adapted to the $O(1)$ universality class.[12] The results of this initial study[7] suggested that the ϕ^4 model would be a useful tool to investigate thermodynamic quantities measured along the critical isochore and coexistence curve. More recently, we have used this model to successfully analyze our heat-capacity data along the critical isochore.[13] The MISTE susceptibility and heat-capacity data have also been analyzed successfully using a new crossover parametric equation-of-state.[13] Further analyses of thermodynamic measurements throughout the critical region are planned using both the crossover parametric equation-of-state and ϕ^4 models.

ACKNOWLEDGMENTS

The research described in this article was carried out at the Jet Propulsion Laboratory, California Institute of Technology, under contract with the National Aeronautics and Space Administration. The authors are indebted to Dr. M. Weilert for supporting the experimental measurements and data analysis.

REFERENCES

1. R. Guida and J. Zinn-Justin, J. Phys. A: Math. Gen. **31**, 8103 (1998).
2. M. Barmatz, *MISTE Science Requirements Document*, Tech. Rep. JPL D-17083, JPL (1999).
3. B. Wallace and H. Meyer, Phys. Rev. A **5**, 953 (1972).
4. C. Pittman, T. Doiron, and H. Meyer, Phys. Rev. B **20**, 3678 (1979).
5. C. C. Agosta, S. Wang, L. H. Cohen, and H. Meyer, J. Low Temp. Phys. **67**, 237 (1987).
6. R. G. Brown and H. Meyer, Phys. Rev. A **6**, 364 (1972).
7. I. Hahn, F. Zhong, M. Barmatz, R. Haussmann, and J. Rudnick (to be published).
8. F. Zhong and H. Meyer, Phys. Rev. E **51**, 3223 (1995).
9. M. Barmatz, F. Zhong, and I. Hahn, Physica **B 284-288**, 206 (2000).
10. M. E. Fisher and S.-Y. Zinn, J. Phys. A: Math. Gen. **31**, L629 (1998).
11. R. Schloms and V. Dohm, Nuclear Physics **B328**, 639 (1989).
12. R. Haussmann (private communication).
13. M. Barmatz, I. Hahn, F. Zhong, M. A. Anisimov, and V. A. Vaktang (to be published).

New Science and Measurement Technology from Critical Dynamics in Microgravity (DYNAMX)

Rob Duncan, A. V. Babkin, S.T.P. Boyd, T. D. McCarson, D. A. Sergatskov (UNM)
P. K. Day, D. Elliott (JPL),
B. J. Klemme (NIST)

DYNAMX is in preparation for the Low-Temperature Microgravity Physics Facility (LTMPF) M1 Mission on the International Space Station (ISS), scheduled for launch in 2005. While the microgravity laboratory will be required to make the first detailed test of the renormalized, field theoretic predictions (by Haussmann and Dohm (HD)) for nonlinear effects near the superfluid transition in ^{4}He, many substantial results have been obtained during our ground definition of this experiment. We have clearly resolved the nonlinear region on Earth, and we have obtained experimental evidence of the gravitational limit to the otherwise divergent correlation length. The microgravity laboratory will be required to make a quantitative comparison of the HD theory to our thermal conductivity data, and to test for the HD quasi-scaling relationship, which would explicitly display the effects of the heat flux on the correlation length. New technology has been developed for DYNAMX, including a new type of paramagnetic susceptibility thermometer, an ultra-miniature cryovalve, and a new cell construction technique. These new technologies will permit next-generation experiments to be conducted on Earth orbit in the future. This work has been supported by NASA through the Microgravity Projects Office. The US Department of Energy funded the development of the PdMn thermometry alloys through Sandia National Labs.

Boundary Effects on the Superfluid Transition of He-4 (BEST)

Guenter Ahlers, University of California, Santa Barbara

This talk will review the opportunities for microgravity and Earth-based measurements of the thermal conductivity $\lambda(t,L)$ of ^{4}He confined in cylindrical geometries of radius *L* with axial heat flow at temperatures near the bulk superfluid-transition line $T_l(P)$(t is the reduced temperature $t = T/T_l - 1$). It provides an evaluation of existing data for L = 1 mm near T_l at saturated vapor pressure (SVP), and uses these to derive a scaling function for the resistivity $R(t,L) = 1/\lambda(t,L)$. The purpose of future measurements over a wide range of L and of the pressure P will be to test the applicability of this function. Here the scaling function is used to assess quantitatively the effect of gravity on potential Earth-based measurements. For typical three-mm-high samples at SVP, values of L significantly larger than 8 mm can only be investigated fully in microgravity. At higher pressures the gravity effect is even larger. The analysis suggests a flight experiment for a cylinder diameter of 50 mm.

Ultra-High-Energy Gamma Ray Bursts from Crossed Cosmic Strings: Simulation by Crossed Vortices in Superfluid Helium

Richard Ferrell
University of Maryland

Probably the greatest puzzle in modern astrophysics is posed by the extremely high-energy cosmic ray bursts. What kind of event could generate such a release of energy? A possible source of sufficiently high energy might be cosmic strings. These topological singularities are conjectured to have been generated in the course of the phase transition that must have taken place at an early stage of the evolution of the universe. Theory dictates that a cosmic string would contain an enormous energy per unit length in its core and that a long cosmic string would remain stable until it encountered and "intercommuted" with another cosmic string. Such a crossing and the shortening of the ensuing kinks is expected to release energy in the very high range that is observed for the cosmic ray bursts. In the spirit of exploiting the analogy between condensed matter phenomena and those observed in the cosmos, we discuss the possibility of simulating, by means of vortices in helium-4, the hypothesized behavior of cosmic strings. We propose to detect the sonic pulse that should result from the crossing of two vortices.

Sound Propagation and Magnetic Resonance in Porous Impurity-Helium Solids

S.I. Kiselev, V.V. Khmelenko, C.Y. Lee, D.M Lee
Laboratory of Atomic and Solid State Physics,
Cornell University, Ithaca, NY 14853-2501, USA

The observed features of attenuation of ultrasound in Im-He samples created after introduction of impurity particles (D_2, N_2, Ne, Kr) in a volume of helium II show that a porous substance consisting of a loosely interconnected continuous network is formed. It is formed by impurity particles encapsulated in solidified helium. The propagation of ordinary sound in these porous samples is similar to the fast sound mode in light aerogels. The temperature dependence of attenuation for different Im-He samples is investigated. It is established that the character of attenuation in D_2-He samples is considerably different from that in heavier Im-He solids (Im = N_2, Ne, Kr). Analysis of attenuation lets us conclude that Im-He samples have a wide distribution of pores from 8 nm to 800 nm. The study of ultrasound in helium in Im-He samples near the λ-point shows the presence of broadening in the attenuation peak as compared with bulk liquid helium. The suppression of T_c is very small, $\leq$0.2 mK. Recent attempts to study hyperfine resonance in D-He solids are discussed.

I. INTRODUCTION

The investigation of neutral atoms and clusters in liquid and solid helium is a rapidly developing research field [1–4]. Much progress has been achieved in studies of the spectral characteristics of single atoms or molecules trapped in matrices of solid helium or dissolved in liquid helium, from which information about the structure of the helium surrounding these impurities was found.

The impurities can be divided into two classes according to the sign of chemical potential inside the helium matrix. Particles with a positive potential tend to form bubbles, while atoms with a negative potential create snowballs. In the latter case, after introducing the impurity particles into liquid helium, we can produce stable impurity-helium (Im-He) clusters, which make it possible to create macroscopic Im-He samples consisting of impurity atoms isolated in liquid or solid helium. At first these systems were obtained by injecting atoms and molecules such as nitrogen, deuterium, neon and krypton [5–7] into superfluid helium. These metastable systems are of fundamental interest. For example, there is the possibility of observing collective effects caused by the interaction of stabilized impurity particles in helium and also the opportunity to create new materials with high energy density stored in them [8]. A very high relative concentration of nitrogen atoms in the solidified helium (N:He = 4%) has already been achieved by injecting the products of a nitrogen-helium discharge into a volume of superfluid helium [6,9]. For this case, the density of the chemical energy stored in these samples ($\sim 5\cdot 10^3$ J/gm) is close to that of the best chemical explosive materials. Another interesting aspect of Im-He systems is the possibility of chemical reactions in a solid matrix when the state of the low-temperature matrix is mostly determined by zero-point motion [10–12]. Investigations of atoms and molecules of hydrogen isotopes stabilized in superfluid helium have revealed tunneling reactions resulting in the exchange of hydrogen and deuterium atoms between the atomic state and the bound molecular state [5].

Investigations of macroscopic solid samples formed by injecting impurities into superfluid helium have opened the possibility for the creation of metastable solid phases built from coalescing clusters of solid helium surrounding the impurity particles. Later it was shown that the centers of the these clusters might consist of either single impurity particles or small clusters of impurities [13,14]. At the same time the structure of these Im-He solids is not fully determined. Recently X-ray spectroscopy showed that the impurities (surrounded by a few layers of solid helium) formed porous structures in superfluid helium [15]. The characteristic size of the constituent building blocks of this porous material is 6 nm. The density of impurity particles can be as high as 10^{20} atoms/cm^3 (with a volume fraction $\sim$0.5%).

We briefly summarize the present state of knowledge regarding the Im-He solids. The preponderance of evidence suggests that macroscopic samples of the Im-He solid phase are built from aggregations of small Im-He clusters. Furthermore, we believe that these aggregates form extremely porous solids into which liquid helium can easily penetrate. They consist of a loosely connected continuous network of impurities or clusters of impurities each of which is surrounded by one or two layers of solidified helium. Therefore we have a unique opportunity to investigate the properties of superfluid helium in porous structures formed by particles with a well known potential of interaction with helium.

A great deal of effort has recently been dedicated to the investigation of superfluid helium in porous materials. We cite here a recent review article describing the specific features of helium in various porous structures [16]. The importance of these studies is now discussed. Superfluidity of helium in restricted geometries has been the object of much theoretical and experimental interest in recent years. Helium has long provided a testing ground for theories of phase transitions. Bulk helium exhibits three-dimensional (3D) critical behavior near lambda transitions, while helium films on flat substrates are 2D with a vortex-inhibiting transition of the Kosterlitz-Thouless type [17]. When helium is adsorbed in a porous medium either as a film or completely filling the pores, its behavior may be changed in a number of ways. Finite size effects might shift or even smear out the phase transition, the multiply-connected substrate geometry may change the effective dimensionality, or disorder induced by the porous material may change the nature of the transition. The superfluid density, ρ_s vanishes near the lambda-point according to the power law:

$$\rho_s(t) = \rho_{s0} \mid t \mid^{\zeta}, \tag{1}$$

where t is a reduced temperature ($t = (T - T_c)/T_c$) with transition temperature T_c. The superfluid density exponent ζ is found to be 0.6705 for bulk helium [18], for helium in Vycor glass [19] and for helium in porous gold [20]. For a particular aerogel it is significantly larger - 0.81 [19]. For different porosity aerogels it changes from 0.71 to 0.81 [21]. At the same time the superfluid transition temperature is suppressed down to 1.955 K in Vycor. For porous gold (which contains larger pores) $T_c = 2.1691 \pm 5 \cdot 10^{-5}$ K, and for different porosity aerogels the suppression is very small: $T_c = 2.16985 \pm 3 \cdot 10^{-5}$ (in 95% aerogel), $T_c = 2.1717 \pm 1 \cdot 10^{-5}$ (in 99.5% aerogel) [21]. In the light of these previous studies, the problem of investigating the critical behavior of helium near the lambda point in the new class of porous material discussed here arises quite naturally. There are experimental difficulties in combining the method of preparing impurity-helium solids with precise heat capacity or torsional oscillator techniques. On the other hand, ultrasonic velocity and attenuation measurements [22,23] can be easily applied to investigate superfluid helium in Im-He solids. The sound velocity in porous media can provide information about the superfluid density as well as the density and elastic properties of the solid matrix. The sound attenuation reflects the dissipation in the system, and its frequency dependence is related to the characteristic pore size [24]. Also, if the sound speed in a "dry" sample (a sample with liquid helium removed) could be measured, we could then determine the effective density of the Im-He solid. This turns to be extremely difficult and has not as yet been accomplished.

The motion of a fluid in a porous medium during acoustic measurements depends on the pore size and the fluid's properties. In liquid ^{4}He the viscous penetration depth is

$$\delta_{visc} = (2\eta/\omega\rho_n)^{1/2}, \tag{2}$$

where η is the viscosity of ^{4}He, ρ_n is the density of the normal component and ω is the frequency of ultrasound. At low sound frequencies, δ_{visc} is bigger than the pore size so the entire normal component is viscously locked to the solid matrix. Therefore the main effect of the fluid is to change the effective density of the porous medium. At high frequencies, only a thin surface layer is dragged along with the solid. The effective density of the porous material then is much smaller and the sound is strongly attenuated by the viscous losses in the surface layer. To use sound for probing the structure of porous material, one should vary δ_{visc} over as large a range as possible. Superfluid helium gives us this unique opportunity. Between 1.0 to 2.17 K the normal fluid density fraction varies from zero to one, causing δ_{visc} to change by an order of magnitude from 1500 nm to 100 nm for 5 MHz sound. Biot created a basic theoretical framework for sound propagation in porous materials [25,26]. He considered the flow of the viscous fluid under an oscillatory pressure gradient in elastic porous solids. In the low frequency regime his theory predicted that attenuation changes as [24]

$$\alpha \propto \rho_n^2\omega^2/\eta, \tag{3}$$

For high frequency sound, the corresponding attenuation is

$$\alpha \propto \sqrt{\eta\rho_n\omega}. \tag{4}$$

In this paper we report results of ultrasound measurements of velocity and attenuation of longitudinal waves in helium filled porous Im-He solids. Some of the results have been published in our previous paper [27]. It was found that the speed of sound in this material is close to and decreases more rapidly with temperature than first sound in bulk liquid helium, similar to behavior observed in aerogel [28]. There was no clear explanation, however, to the way the attenuation of ultrasound changes with temperature in helium filled Im-He solids. Here we present the results of more detailed investigations of the speed and attenuation of sound, particularly near the lambda-point. One goal of this work was to check a possible T_c suppression. We also performed the measurements at different frequencies (1,3,5 MHz) to help us to understand the mechanism of attenuation. Moreover we investigated the stability of different Im-He samples between 1 and 4.2 K.

The final section of our paper will discuss the hyperfine resonance experiment.

II. EXPERIMENTAL METHOD

A. Preparation of porous impurity-helium solids

The technique for creating impurity-helium solids in a volume of He II was similar to that developed by the Chernogolovka group [6,29]. A gas jet of helium containing a small fraction (0.5-1%) of impurity atoms or

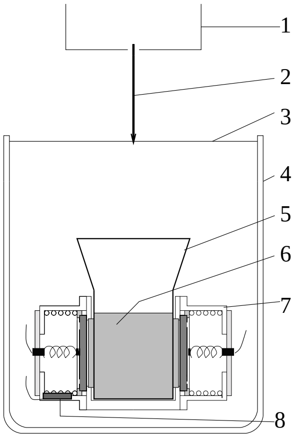

FIG. 1. Experimental cell: 1 - Atomic and molecular source, 2 - Impurity-Helium jet, 3 - surface of liquid helium, 4 - quartz dewar, 5 - quartz funnel, 6 - Impurity-Helium solid, 7 - ultrasound cell, 8 - germanium thermometer.

molecules impinged onto superfluid helium contained in a small dewar beaker sitting in the main helium glass dewar (Fig.1). The helium vapor pressure in the dewar was maintained at 1-5 Torr by a high speed rotary pump. The gas entered through a quartz capillary of diameter about 0.7 mm, near the end of which was a region containing a high power RF (60 MHz) discharge for dissociation of molecules. In this series of experiments most of the Im-He samples were created by introducing into He II a gas jet not subjected to the action of the RF discharge. When there was no need to dissociate molecules we used a stainless steel capillary with inner diameter of 1.6 mm surrounded by a vacuum jacket with a heater at the bottom end. As in all of our previous setups, the diameter of the hole at the end of the capillary was 0.7 mm. The nozzle of the capillary was located 2 cm above the surface of the superfluid helium in the small quartz dewar mentioned above, which acted as the collection beaker. To prevent the freezing of impurities in the nozzle we heated the end of the capillary by an annular heater ($R \sim 10\Omega$). In order to keep the level of helium in the beaker constant, a continuously operating fountain pump was used. When the gas mixture jet impinged on the surface, a macroscopic snowflake-like semitransparent material was created. This fell down through the liquid and then congealed, forming a porous impurity-helium solid between the transducers of the ultrasound cell. The centers of transducers were ~5cm below the level of helium in the beaker. For more effective collection of the sample in the cell we used a quartz funnel with two side plates which were placed between the endplates of the cell. On some occasions, in order to compress the sample at low temperatures we used a small teflon cylinder which could be moved up and down. We can monitor the presence of the sample in the cell and its homogeneity visually through slits on the sides of the glass dewars. In these experiments the impurities used were Kr, Ne and molecular D_2 and/or N_2. Gas mixtures of Im:He = 1:100 were used to dilute the impurity particles and therefore prevent them from congealing as they passed from the source to the surface of the liquid helium. The total flux of the gas mixtures was $(4\text{-}6)\cdot 10^{19}$ particles/s. Samples with a visible volume between 1.2 and 1.7 cm^3 were usually used.

B. Ultrasound cell

In our experiments we used two different ultrasound cells. In the first cell two x-cut gold plated quartz transducers (5 MHz fundamental) were used [27]. The crystals were 1 cm in diameter. Each of these was pushed against the parallel walls of the cell by two springs, one of which served as a central electrode. The ground was provided by the brass body of the cell. The path length was determined at room temperature with a micrometer with a correction being made for the contraction upon cooling. The value for the path length used in the experiments was 1.572±0.005 cm. In our second cell we used two $LiNbO_3$ transducers with fundamental frequency ~1 MHz (Fig. 1). The odd harmonics were also used (3 and 5 MHz). The transducers were 1.3 cm in diameter. Otherwise the design of the second cell was similar to the first one except that the distance between transducers was 1.470±0.005 cm.

C. Spectrometer

The ultrasonic measurements were made using a homodyne phase-sensitive spectrometer (Fig. 2). A continuously operating oscillator was gated to provide a transmitter pulse of 4-12 μsec.

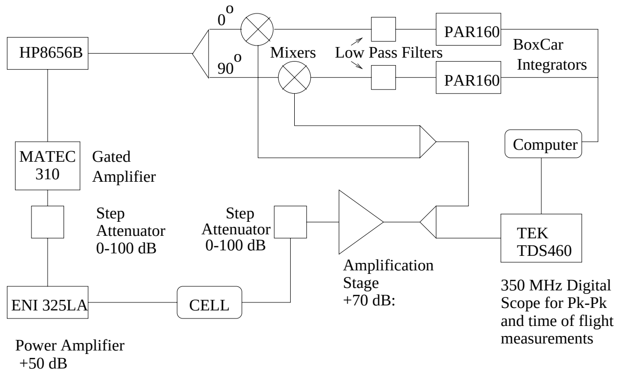

FIG. 2. Ultrasound spectrometer: 1 - HP8656B signal generator; 2 - MATEC310 gated amplifier; 3, 6 - step attenuators (0-100 dB); 4 - ENI325LA power amplifier (+50 dB); 5 - ultrasound cell; 7 - amplification stage (+70 dB); 8, 9 - power splitters; 10 - hybrid power splitter; 11, 12 - mixers; 13, 14 - low pass filters; 15, 16 - PAR160 box car integrators; 17, 18 - multimeters; 19 - computer ; 20 - TEK TDS460 oscilloscope for peak-peak and time of flight measurement.

The amplitude of the input signal could be varied from 1 to 100 V at the resonant frequency or at the odd harmonics of the transmitting crystal. The ultrasonic pulse was received by the second crystal, amplified and split in two parts, one of which was used to directly measure the attenuation by recording the amplitude of the signal on a TEK460 digital oscilloscope. The second part was split again in two parts to obtain the 0° and 90° components, A_{0° and A_{90°. They where used to determine the phase of the signal ϕ:

$$tan(\phi) = A_{0^\circ}/A_{90^\circ}. \tag{5}$$

Once the initial speed of sound was measured at the temperature T_0 from the pulse transit time τ_0, changes in velocity were calculated from the phase of the received signal.

$$\Delta v = l \; / \; \left(\tau_0 + \frac{\phi(T) - \phi(T_0)}{\omega}\right), \tag{6}$$

where l is the length of the cell. With typical samples the changes in velocity of a few parts per million could be resolved. A second oscilloscope was used to display the signal on a longer time scale. It registered up to 12 echoes of the signal in the first cell but only 3 echoes in the second one.

D. Thermometry

For temperature measurements, a calibrated Lake Shore germanium resistor was used. The thermometer was located inside the base of the cell just outside the path of the ultrasonic pulses so that the effect of the temperature difference between the thermometer site and the sound path is minimized. After the lowest temperature (1.0-1.1K) was achieved through pumping by both the rotary pump and a roots blower, the initial speed of sound was measured. In the next stage, by closing the pumping line down the temperature was allowed to increase by ~10^{-4} K/s. Near the lambda-point the rate was decreased to about 10^{-6} K/s. During the warm up, the fountain pump was constantly supplying helium into dewar beaker up to the lambda-point. After the superfluid transition, the warmup rate increased to 10^{-4} K/s but boiling in the inner dewar did not occur.

III. EXPERIMENTAL RESULTS

Fig.3 shows the results of 5 MHz ultrasound measurements (in the first cell) at T=1.1-2.2K in different Im-He solids (Im = D_2, Ne, Kr) just after preparation. Here and in later figures we show for comparison the velocity and attenuation of sound in bulk helium which were measured in each experiment before accumulating the sample. The attenuation of sound in the presence of Im-He samples (for such heavy impurities as Ne, Kr) is larger than in bulk helium at low temperatures and increases rapidly with temperature, after which it reaches a plateau and at the λ-point it goes through a maximum. Whereas heavy Im-He samples all have similar characteristic features, the D_2-He solid behaves quite differently. In the latter case, we do not observe any measurable effect on the speed of sound, and attenuation has a behavior similar to that of bulk liquid helium, although slightly (~1dB/cm) higher. The samples produced with heavy impurities are much denser than the ones with the D_2 impurity. In the case of the heavy impurities, investigations become impossible above temperature in the neighborhood of 1.4 K because of an extremely high attenuation. We could have increased the signal by decreasing the distance between the transducers but the method of collecting the sample does not allow us to do that. Therefore, in a series of experiments we introduced pulses with very large (up to 100 V) values of the input amplitude. From the analysis of attenuation in different Im-He samples it became clear that D_2-(heavy Im)-He samples are, in fact, the most suitable ones for investigations of mechanisms of attenuation, because they have a relatively small attenuation. In this work we compare three samples: N_2-He, D_2-He, and mixed D_2-N_2-He. We investigated the stability of these samples and also the frequency dependence of ultrasound attenuation. Measurements were performed between 1.0 K and 4.2 K, with special attention to the region near the λ-point. Fig. 4 shows the characteristic temperature

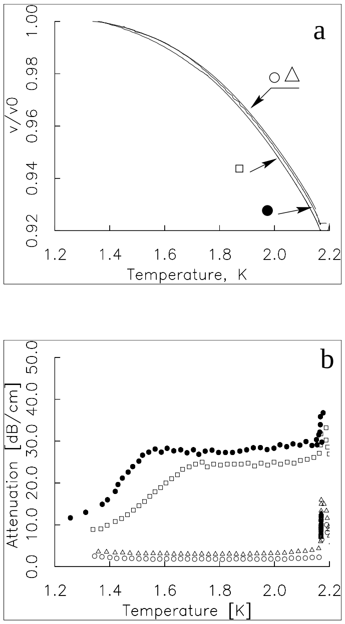

FIG. 3. The velocity (a) and attenuation (b) of 4.96 MHz sound in liquid helium : in bulk (○), in D_2-He solid (△), in Ne-He solid (□), in Kr-He solid (●). V_0 is the ultrasound velocity at initial temperature for these measurements, T=1.362 K.

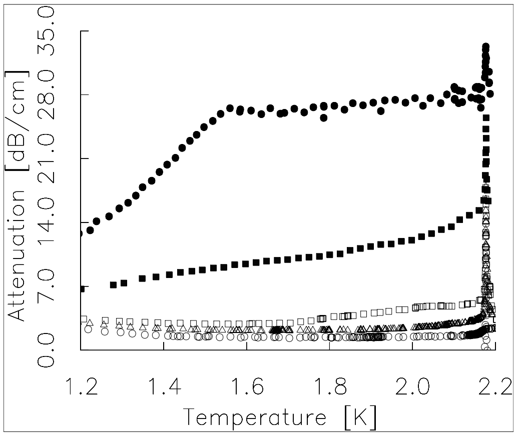

FIG. 4. The attenuation of 5 MHz ultrasound in liquid helium: in bulk (∘), in D_2-He solid (△), in D_2-N_2-He solid (prepared without discharge (□), with discharge (solid □)), in N_2-He solid (•).

dependence of attenuation for these three samples. The behavior of the attenuation in the D_2-N_2-He solid repeats that of the D_2-He solid and bulk helium up to T∼1.75 K. Warming up further, it becomes closer to the behavior of the N_2-He solid, *i.e.* the attenuation increases and then reaches a plateau.

A. Stability of the structure of Im-He solids.

In this section we discuss the factors affecting the structural stability of Im-He samples. Changes in the structure should lead to changes in the attenuation of ultrasound. Earlier it was discovered that the compression of samples results in an increase of attenuation [27]. In this series of experiments we show the impact of warmup from 1.0 K to 2.2-4.2K on the structure of our samples.

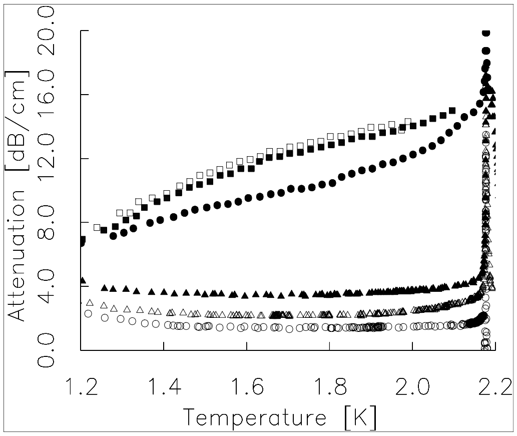

FIG. 5. The attenuation of ultrasound in liquid helium: in bulk (∘), in D_2-He solid (after preparation of solid (△), after crossing λ-point and cooling down (solid △)), D_2-N_2-He solid prepared with discharge (after preparation (•), after crossing λ-point and cooling down (solid □), after warming up to 2.1 K and cooling down (□))

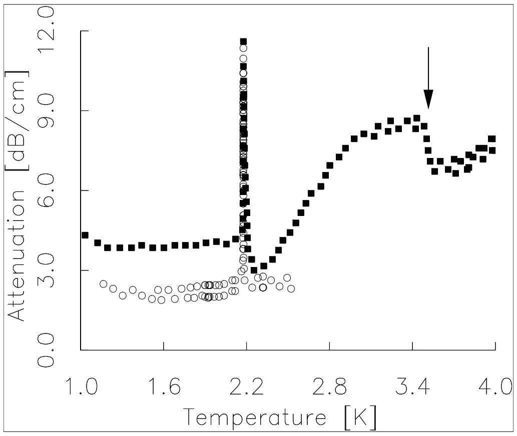

FIG. 6. The attenuation of 3.16 MHz ultrasound in liquid helium: in bulk (∘), D_2-N_2-He solid (solid □).

Fig. 5 presents the results of ultrasound measurements for the three samples mentioned above as they were warmed up in the temperature ranges below or above T_λ. We can see that as the sample was heated up to $T_{max} < T_\lambda$ and then cooled again, there was no change in attenuation and therefore the structure did not change. Crossing T_λ always led to the small transformations in the structure registered by a slight increase of sound attenuation. The attenuation preserved its characteristic features, nevertheless.

Fig. 6 shows the attenuation of ultrasound in liquid helium filled D_2-N_2-He solid during warmup from 1 K to 4.2 K. It was found that a sudden drop in attenuation takes place at 3.4-3.5 K, which is attributed to the change of structure of this solid. Below this temperature, the sample occupied the whole cell, but at T∼3.5 K a significant compression of the solid by a factor of 12 was observed. This is the first observation of a spontaneous macroscopic change of structure of an Im-He sample in liquid helium. For N_2-He without D_2, these changes were not observed.

B. Frequency dependence of the sound attenuation.

Fig. 7 presents the frequency dependence of the attenuation of ultrasound in a N_2-He sample. Decreasing the frequency leads to a lower attenuation and also shifts the point where the attenuation levels off to a plateau to higher temperatures. Fig. 8 shows the frequency dependence of attenuation in D_2-N_2-He sample measured at 3 and 5 MHz. It significantly differs from the one observed in heavy Im-He samples (like N_2-He). For the first time, for the D_2-N_2-He solid, we detected a steady and steep monotonic increase in the attenuation up to the λ-point without occurrence of a plateau for 5 MHz sound. This might be explained by the purely high frequency behavior of the attenuation in this sample. For 3 MHz attenuation we observed only a slow linear increase in the same

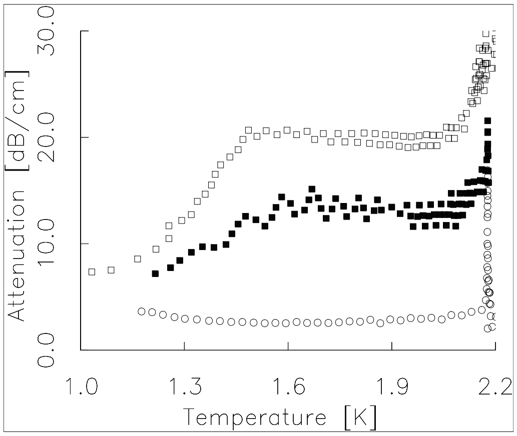

FIG. 7. The attenuation of ultrasound in liquid helium: in bulk (○), in N_2-He solid at 3.16 MHz (solid □), at 5.33 MHz (□).

temperature range.

C. The behavior of the sound attenuation and the speed of sound near T_c.

The results of measurements near the λ-point for N_2 are shown in Fig. 9. Different symbols represent different samples. The maxima of attenuation near the λ-point for N_2-He samples are much broader than for liquid helium, making the precise determination of the position of the maxima impossible. We can conclude from this data that there is no significant shift of the λ-point for helium-filled porous N_2-He solids.

Fig. 10 shows the attenuation of ultrasound (only 5 MHz data is presented) in the mixed D_2-N_2-He solids. The width of attenuation peak near the λ-point is only slightly broader than that for pure helium. That makes it possible to determine the more precise position of the center of the peak. It appears that the shift of peak with respect to bulk helium is $\sim$0.2 mK, but at the same time the reproducibility of the measurements of the sound attenuation maximum in liquid helium from run to run is about $\sim$0.1 mK. Therefore based on these experiments we can say that even if the shift exists, it is less than or on the order of 0.2 mK. Note that Fig. 10 reflects the fact that the attenuation peak in bulk helium is $\sim$0.8 mK below the λ-point [30].

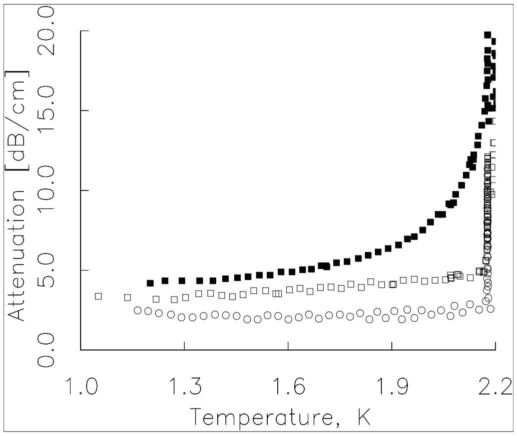

FIG. 8. The attenuation of ultrasound in liquid helium: in bulk (○), in D_2-N_2-He solid at 3.16 MHz (□), at 5.33 MHz (solid □).

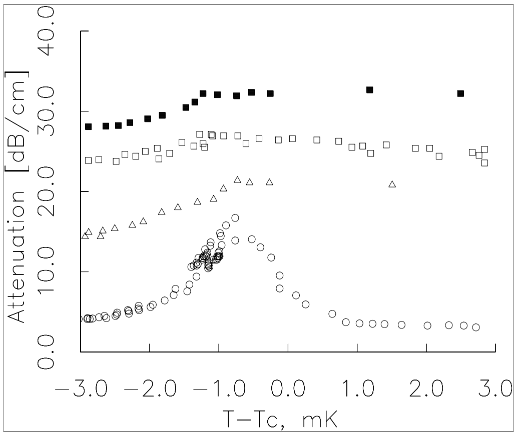

FIG. 9. The behavior of attenuation of 4.96 MHz sound in liquid helium near λ- point : in bulk (○), in different N_2-He solids (△,□,solid □). For N_2-He solids the attenuation is shifted by 0, 5 and 10 dBm/cm correspondingly.

IV. DISCUSSION.

A. Velocity of sound in Im-He solids.

Before performing this series of experiments, it was impossible to predict the characteristics of sound propagation in Im-He samples created by introducing impurities into superfluid helium. According to the existing model, these Im-He solids represent metastable phases formed

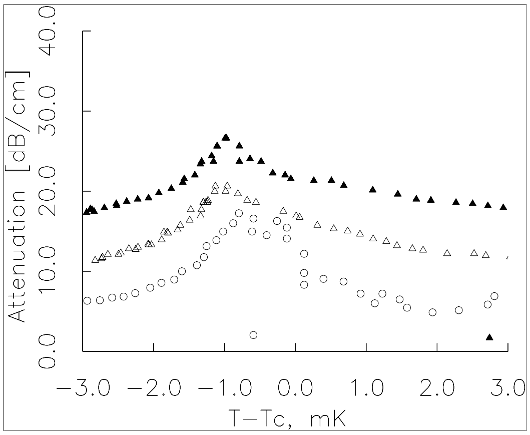

FIG. 10. The behavior of attenuation of ultrasound in liquid helium near λ- point : in bulk (○), in different D_2-N_2-He solids (△, solid △). For D_2-N_2-He solids the attenuation is shifted by 0, 5 and 10 dBm/cm correspondingly.

by coalescing Im-He clusters, in which helium is solidified as a result of large attractive van der Waals interactions between helium atoms and a central impurity particle. Therefore under the conditions of compact packing of these clusters one would expect an increase in elastic modulus for this material and also an increase of the speed of sound with respect to pure bulk liquid helium. A discovery of this effect was one of the first goals of this experiment. However we were not able to produce samples for which we could detect an increase in the speed of sound although we used our standard methods for creation of Im-He solids [6,7]. On the contrary, we observed a smaller speed of sound than in superfliud helium. The only exception were D_2-He samples for which the sound velocity was the same as in helium to great precision. The observed decrease in the speed of sound can be explained by the creation of the porous structure of solid helium around the impurity particles. This is also supported by the fact that the behavior of the speed of sound resembles the fast sound mode in porous aerogel [28]. This mode is intermediate between first and fourth sound. Here the normal component is locked in a very compliant solid matrix so that the liquid and the aerogel fibers move together under mechanical and thermal gradients. McKeena *et al.* [28] developed a theory explaining the behavior of sound modes in aerogel, taking into account coupling between the normal component and the aerogel and its elasticity. The same features are observed in Im-He samples.

B. Attenuation of sound in Im-He solids.

As we pointed out before, the behavior of the attenuation of sound in different heavy Im-He solids has the same characteristic features. We observe the transition from the plateau with a small attenuation to the plateau with a bigger one, which ends with a maximum at the λ-point. This can be explained by the structure of this porous material, which is characterized by a wide distribution of pore sizes. Among these pores there are large channels in which the behavior of the helium is close to bulk helium. The existence of these pores is realistic especially if we take into account the method of collecting Im-He solids. This is a highly nonequilibrium process in which the impurity particles cooled by the helium vapor enter the superfluid helium where they stick together after random collisions with each other. So in this process, as the model of aggregation of the small particles into clusters predicts [31], highly ramified fractal structures are created.

The accumulation of Im-He sample is characterized by the existence of a convective flow of helium which moves parts of the created condensate from a location where impurity particles first hit the surface of the helium to the bottom and to the walls of the cell. Later these small pieces of porous material stick together to form the Im-He solid. They do not coalesce homogeneously, however. Therefore macroscopic voids might be created between them, which can lead to the formation of large channels in the final condensate. We should notice that this Im-He solid preserves its form unless removed from the helium. Then it compresses by 60% [9].

Qualitatively the behavior of attenuation of sound in samples with this structure can be explained as follows: At the lowest temperatures the normal component of helium is locked to the solid matrix and the attenuation is small. Warming leads to a decrease of the viscous penetration depth δ_{visc} so that, when it is comparable to the pore size R of our solid, the decoupling of a portion of the normal fluid occurs. Therefore sound attenuation caused by the friction of the layers of normal fluid as they become unlocked from the solid matrix begins to increase rapidly. Let us call the temperature, where this occurs, T_1. Continuous warmup leads to decoupling of helium in a greater number of pores. We define T_2, as the temperature, where the sound propagates only in the large channels. There helium is almost like bulk helium and does not feel the effect of the walls. In addition sound can propagate through the smallest pores formed at the earliest stage of the creation of the sample. Helium in these pores is still locked to the solid matrix and attenuation is low and almost independent of temperature. This resembles the behavior of attenuation in bulk superfluid helium.

Calculating viscous penetration depths for T_1 and T_2 we can find the corresponding pore size (δ_{visc}=R). These results, inferred from Fig. 3b and 4, are shown in Tab. 1. Samples produced by injecting heavy impurities in superfluid helium are characterized by the presence of the pores of large size - from 150 nm to 820 nm. On the other hand, the D_2-N_2-He sample has smaller pores - 100nm to 140 nm. It should be pointed out that from the analysis of the lowest temperature part of attenuation, we can estimate only the pores of larger size where a large attenuation is observed. Information about the smallest pores is much harder to obtain because after T_2, sound propagates not only through them but also through the large size channels.

This model is supported by investigation of sound attenuation in the same sample but at different frequencies. Fig. 7 shows that a decrease in frequency leads to a decrease of attenuation. Also T_2 shifts to the higher temperature. For both frequencies δ_{visc}(T_2=1.48K at 5MHz) is equal to δ_{visc}(T_2=1.6K at 3MHz) which is in magnitude equal to 240 nm.

Im-He samples formed in our experiments have a variety of different volume ratios between the porous part and the large channels. Compressing these samples leads to a decrease in the volume of the large channels, which in turn increases the attenuation, as was detected in the

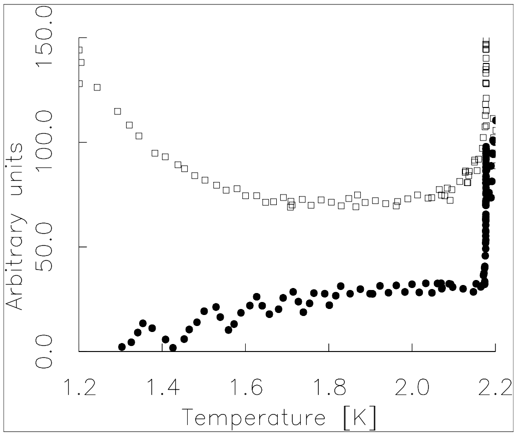

FIG. 11. Temperature dependence of ultrasound attenuation divided by $(\rho_n \omega \eta)^{1/2}$ for D_2-N_2-He sample at 5.43 MHz (□) and 3.16 MHz (•)

.

previous experiments [27]. The comparison of attenuation in freshly prepared samples and in those recycled above T_λ showed that crossing the λ transition always gives a somewhat larger attenuation caused by the compactification of Im-He solids. A much larger effect was observed in the D_2-N_2-He sample during warmup to 3.4-3.5 K where a sudden drop in attenuation was observed. In addition it was seen visually that the sample volume changed from 1.7 cm^3 to 0.14 cm^3. We did not observe a similar effect in N_2-He samples. Hence this change of attenuation is ascribed to the collapse of the porous structure formed by deuterium molecules. It seems as if a similar effect was detected in the work of Gordon *et al.* [32], where a significant decrease of concentration of deuterium atoms contained in a D_2-Ne-He sample was registered during the warmup from 1.8 K to 4.2 K.

Analysis of sound propagation in Im-He solids shows that a distribution of the channels in superfluid helium is present, including very large channels, in which the helium behavior is close to that of bulk helium. Although the speed and attenuation of sound did not reveal any substantial suppression of T_c in N_2-He samples, we discovered a very small shift in D_2-N_2-He samples, on the order of 0.2 mK which is similar to that in a very light aerogel. In addition, a small broadening of the attenuation peak was detected for N_2-He solid near the λ-point. The width of these peaks gives us information about the smallest pores in the samples. Using Josephson's relation [33] for helium in the channels of Im-He solids, namely

$$\xi(t) = \xi_0 \mid t \mid^{-\zeta} = \frac{k_B T_c m^2}{\hbar^2 \rho_s(t)} \tag{7}$$

we can find the correlation length at the temperature where the broadening of the attenuation peak starts. At this temperature T, the superfluidity in the pores (where the pore radius $R=\xi(T)$) starts breaking up. In equation (7) m, k_B and $\hbar$ are the mass of a helium atom, Boltzmann's constant and Planck's constant respectively. From Fig. 7 we can say that the onset of broadening of the attenuation peak is at T∼2.1 K, which gives the characteristic size of the pores from the argument above as R∼8nm. This is reasonably close to 6±2nm, the size of the clusters from which our Im-He solids are built [15].

Under certain favorable circumstances we were able to produce samples without any of the large channels and in this case we did not observe the plateau in the temperature dependence of the attenuation (see Fig. 8). This idea was checked by plotting attenuation divided by $(\rho_n \omega \eta)^{1/2}$ as shown in Fig. 11. The constant straight line above T∼ 1.6 K describes the high frequency behavior of helium in this particular porous sample, which implies that the energy loss is occurring on the entire surface in a thin layer of thickness δ_{visc}. At a lower frequency this behavior starts at a higher temperature because the viscous penetration length is larger. If we compare the temperatures at which the graph in Fig. 11 levels off to a straight line, we get the same value of δ_{visc}∼180 nm for 3 and 5 MHz ultrasound.

V. SUMMARY OF ULTRASOUND STUDIES.

Im-He solids have opened up a variety of intriguing possibilities for experimental investigations of the quantum properties of helium, as well as for studying atoms, molecules and small clusters stabilized in solidified helium. These studies provide a new perspective for matrix isolation in solidified helium. The big advantage of the Im-He solids is that a large variety of atoms or molecules can be used to build the "backbone" of the Im-He samples. It also appears that, depending on the preparation conditions, samples with different nanostructures can be prepared. To understand the properties of the Im-He samples it is necessary to determine their microscopic structure.

In this work investigations of the velocity and attenuation of ultrasound was used to study the characteristics of Im-He samples formed by introducing different impurities in the volume of superfluid helium. For helium in Im-He samples the speed of sound is a little smaller than in bulk helium, and its temperature dependence is close to the fast sound mode in light aerogel [28]. The character of attenuation of ultrasound in helium in Im-He samples is different from that in other porous materials like Vycor, porous gold, aerogel. The temperature dependence of ultrasound attenuation in D_2-He samples is close to that in bulk helium whereas it is considerably different from the attenuation in heavy Im-He samples. This allows us to grow mixed solids, such as D_2-N_2-He, in which the attenuation can be regulated by the content of the gasous mixture. For these mixed samples we produced and investigated the most 'perfect' porous solids, which do not contain large channels of bulk helium.

From the analysis of attenuation of ultrasound in Im-He samples, we conclude that they have a wide distribution of pore sizes between 8 nm and 800 nm, as well as large channels in which the behavior of helium is close to that of bulk liquid helium.

We investigated the behavior of the velocity and attenuation of ultrasound in Im-He samples near the λ-point where a broadening of the λ-peak is observed. The broadening increases with increasing sample density. A small shift of the transition temperature ($\sim$0.2mK) was observed for D_2-N_2-He samples.

For a better understanding of the microscopic structure of Im-He samples, a study of low angle x-ray scattering might be very helpful. The similarity between the behavior of ultrasound in Im-He samples and in aerogel suggests the possibility of a fractal structure for Im-He solids. For studies of the critical behavior of helium in Im-He samples, investigations of second sound (low frequency sound) are the most appealing. We believe that this will allow the observation of the slow sound mode similar to the one observed in aerogel [28] and also the determination of the critical exponent for different Im-He solids.

VI. MAGNETIC RESONANCE STUDIES OF D-HE SOLIDS.

A. Background.

In this section we discuss the possibility of performing hyperfine resonance experiments on helium-impurity solids containing atomic deuterium (D) as the primary impurity. The D-He solid is of particular interest because of the low mass of the deuterium atom, leading to the expectation that the properties of these solids would be dominated by zero point motion. Thus we may consider the D-He solid to be an extreme quantum solid. It would also be desirable to form H-He solids, but unfortunately it is difficult to introduce and maintain a population of hydrogen atoms in these solids.

Magnetic resonance experiments, in general, are powerful probes of the nature of impurity-helium solids for the case of magnetic impurities. They provide a means to determine the impurity atom concentration via a study of the signal strength. Line width and T_2 studies can be interpreted in terms of the separation between the impurities, since in homogeneous magnetic fields the linwidth is associated mainly with dipole-dipole interactions. Pulsed magnetic resonance methods can be used to determine spin diffusion in dilute samples which are not dominated by T_2 effects. The Chernogolovka group [32] has performed an extensive series of electron paramagnetic resonance experiments on D-He solids using CW methods at 10 GHz (X-band). They indeed were able to measure D atom concentration up to 10^{18} atoms per cm^3. They also studied the line widths for various deuterium atom concentrations, and showed that the line widths were broadened appreciably for high D atom concentrations.

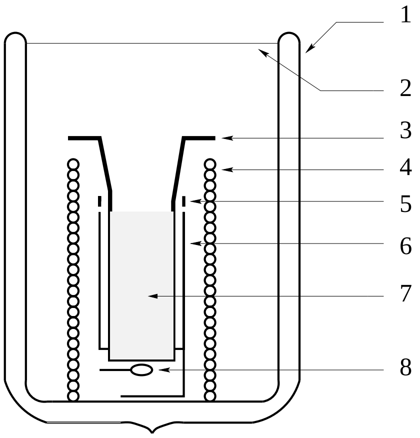

FIG. 12. The low temperature part of the apparatus: 1- quartz dewar beaker, 2- superfluid helium, 3- quartz cell, 4- superconducting solenoid, 5- tuning ring, 6- split-ring resonator, 7- Im-He sample, 8- coupling loop

In the present work we describe the application of the hyperfine resonance method to study the recombination of these atoms and their relaxation times in solid D-D_2-He systems. Determination of T_1, T_2 and spin diffusion will probe the local environment and transport of the deuterium atoms.

The D atom densities in experiments on gaseous atomic deuterium were severely limited by surface recombination. In the solid samples we are studying, the atomic densities are much larger, but the resonance lines are broadened by magnetic dipolar interactions between neighboring deuterium atoms.

B. Experimental Setup

To produce deuterium atoms, a mixture of D_2-He was passed through a high frequency discharge. The resulting D-D_2-He mixture struck the surface of superfluid helium and small solidified clusters then formed a porous network of D-D_2-He solid [27].

Fig. 12 shows the low temperature part of apparatus. The sample is accumulated in the cylindrical part of an open quartz cell fully occupying the central bore of a split-ring resonator. The resonator design, previously described by Nunes [34], is a copper cylinder (2 cm long and 1 cm in diameter) with a single longitudinal slot containing a rectangular piece of copper laminated capton (about 0.1 mm thick). To have a resonance close to the hyperfine frequency ($\sim$309 MHz) we trimmed the laminate with a pair of scissors. For fine tuning *in situ*, a movable metallic ring, which varied the resonant frequency by changing the effective inductance of the resonator, was used. The adjustable range of the resonator

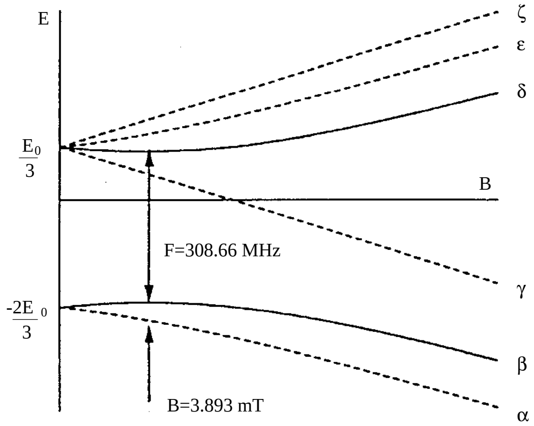

FIG. 13. Energy level diagram of atomic deuterium in a magnetic field.

was about 3 MHz. The Q increased from about 30 at room temperature to $3{\cdot}10^3$ at 4.2K and did not change noticeably below that temperature. The resonator was coupled to the external circuit through a small coupling loop in the bottom part of the resonator. To achieve a better coupling an external tuning trombone was used. When the temperature was stabilized near 1.6 K final adjustments of the coupling and the frequency were made. A superconducting solenoid producing a bias field for hyperfine resonance was placed around the resonator. The whole assembly described above was immersed in superfluid helium in a small dewar beaker, contained in a larger dewar partially filled with superfluid He.

C. Hyperfine resonance and search for FID.

We are investigating the pulsed magnetic resonance transition between the $\beta(F = 1/2, m_F = -1/2)$ and $\delta(F = 3/2, m_F = -1/2)$ hyperfine levels to observe D atoms (see Fig. 13). This is a longitudinal transition, which means that the bias field and the oscillating magnetic field are parallel. The resonance frequency of the $\beta \rightarrow \delta$ transition depends on the applied static field near B_0 according to the equation :

$$f = f_0 + c(B - B_0)^2 \tag{8}$$

where f_0=308.66092 MHz and c=1272.859 kHz/mT^2. We use this transition near the minimum of the energy splitting (at B_0=3.893 mT as seen in Fig. 2) to minimize the effect of the magnetic field inhomogeneity.

In the present experiments we used two different gas mixtures to produce stabilized deuterium atoms: D_2:He=1:100 and D_2:Ne:He=1:4:500. After a collection of the sample was finished, we lowered the cell inside the resonator and performed a final tuning of the resonator to the resonant frequency f_r. In searching for the free induction decay (FID) from the $\beta \rightarrow \delta$ hyperfine transition we applied $\pi/2$ pulses to maximize the signal. The power necessary for a $\pi/2$ pulse is calculated from :

$$P_{\pi/2} = V_c \frac{\pi\omega}{2Q}\left(\frac{1}{2\gamma t}\right)^2, \tag{9}$$

where V_c is the volume of the cavity and γ is the electron gyromagnetic ratio. For a $t = 10\mu$sec pulse duration the $\pi/2$ tipping pulse is at a power level of 7.5 μW.

A heterodyne spectrometer was used in our experiment [34]. In our search for a FID we slowly scanned the bias magnetic field from 40 to 60 G (at the rate ∼0.1G/s) at fixed frequency f_r. Then we changed f_r and repeated this procedure again. We varied f_r from 307.5 MHz to 310.5 MHz because the behavior of the hyperfine resonance of deuterium in the solid matrix differs from the one for free deuterium atoms in a gaseous phase. Knight *et. al.* [35], for example, showed that the hyperfine line of D atoms in solid Ne, Ar and Xe can shift by as much as 1%. Unfortunately our search did not yield a positive result. Below we discuss why we failed to find a FID signal and what we have to do next to reach our goal.

D. Discussion

Earlier investigations of deuterium atoms stabilized in helium [32] showed that it is possible to reach very stable high relative concentrations of D atoms with a characteristic decay time more than 3600 sec. This result differs significantly from experiments with gaseous deuterium , where it was impossible to reach concentrations higher than about 10^{14} cm^{-3} because of the high recombination rate of deuterium . On the other hand, the D-D_2-He solid formed in our experiment is a quantum solid. The large zero point oscillations of D atoms suggests a high speed of quantum diffusion of deuterium in solidified He. ESR experiments showed that a relative concentration of deuterium atoms in molecular deuterium can reach [D]/[D_2]=0.5% [32]. D atoms were most likely stabilized in the small clusters of molecular deuterium surrounded by solidified helium. The local concentration of deuterium atoms is expected to be considerably larger than the average concentration characteristic for this extremely porous structure. If the density of molecular deuterium in helium (as in the case of heavier impurities [15], like Ne and N_2) is 10^{20} cm^{-3}, then the average concentration of deuterium atoms is about $5{\cdot}10^{17}$ cm^{-3}. Therefore the expected width the of magnetic resonance line due to dipole-dipole interactions is

$$\Delta H = \frac{2\pi^2}{3\sqrt{3}}\beta \cdot n \sim 0.04G, \tag{10}$$

β - Bohr magneton, n - concentration of deuterium atoms. Experimentally a much larger ESR linewidth of 5.6 G was observed [32]. This corresponds to local concentrations of $\sim 8{\cdot}10^{19}$cm^{-3}.

We used a similar sample for hyperfine resonance studies. With ΔH=5.6 G (near the minimum of hyperfine level splitting at B=B$_0$), equation (8) gives $\Delta f = f - f_0$=400kHz. The large local concentration of D atoms corresponds to a value of T_2 in our sample of $T_2 = 1/2\pi\Delta f = 0.5\mu$s, which is shorter than our resonator ring down time $\tau = Q/\omega = 1.5\mu$s ($Q = 3 \cdot 10^3$). Therefore our search for the FID in our deuterium-helium sample did not give a signal. This supports the argument about the uneven distribution of deuterium atoms in D-D$_2$-He samples and the presence of regions with high local concentrations of deuterium atoms. The creation of samples with much smaller local concentrations of D will allow us to increase T_2 in this system and hopefully observe a FID signal. We are planning to investigate samples obtained by condensation of a diluted gas mixture (D$_2$:Ne:He=1:10^3:10^5). In these solids atoms of deuterium will be diluted by Ne atoms. The local concentration of D atoms will be $\leq 10^{19}$ cm^{-3} giving a characteristic T_2 of order 10 μs, which we should be able to observe.

In addition we are in the final stage of preparing a new series of experiments using a pulsed NMR method (5 MHz) for investigation of molecular deuterium in D$_2$-He samples and also CW ESR (X-band) for exploration of deuterium atoms stabilized in helium.

VII. ACKNOWLEDGEMENTS

We would like to thank NASA for its support through grant NAG 8-1445. We also wish to thank Drew Geller, John Beamish, Jeevak Parpia and John Reppy for very useful suggestions and discussions.

---

[1] B. Tabbert, H. Gunter, and G. zu Putlits, *J. Low Temp. Phys.* **109**, 653 (1997)
[2] J.P. Toennies, and A.F. Vilesov, *Annu. Rev. Phys. Chem.* **49**, 1 (1998)
[3] S.I. Kanorsky and A. Weis, *Adv. At. Mol. Opt. Phys.* **38**, 87 (1998)
[4] E.B. Gordon, A.F. Shestakov, *Low Temp. Phys.* **26**, 1 (2000)
[5] E.B. Gordon, A.A. Pelmenev, O.F. Pugachev, and V.V. Khmelenko, *JETP Lett.* **37**, 282 (1983)
[6] E.B. Gordon, V.V. Khmelenko, E.A. Popov, A.A. Pelmenev, O.F. Pugachev, *Chem. Phys. Lett.* **155**, 301 (1989)
[7] E.B. Gordon, V.V. Khmelenko, A.A. Pelmenev, E.A. Popov, O.F. Pugachev, A.F.Shestakov, *Chem. Phys.* **170**,411(1993)
[8] B. Palaszewski, L.S. Ianovski, and Patrick Carrik, *J. Propulsion and Power* **14**, 641 (1998)
[9] R.E.Boltnev, E.B. Gordon, I.N. Krushinskaya *et al. Fiz. Nizk. Temp.* **18**, 819 (1992) [*Sov. J. Low Temp. Phys.* **18**, 576 (1992)]
[10] R.E.Boltnev, E.B. Gordon, V.V. Khmelenko, I.N. Krushinskaya, M.V. Martynenko, A.A. Pelmenev, E.A. Popov, A.F. Shestakov, *Chem. Phys.* **189**, 367 (1994)
[11] R.E.Boltnev, E.B. Gordon, I.N. Krushinskaya, *et al. Low Temp. Phys.* **23**, 567 (1997)
[12] R.E.Boltnev, I.N. Krushinskaya, A.A. Pelmenev, D.Yu. Stolyarov, V.V. Khmelenko, *Chem. Phys. Lett.* **305**, 217 (1999)
[13] R.E. Boltnev, E.B. Gordon, V.V. Khmelenko, M.V. Martynenko, A.A. Pelmenev, E.A. Popov, A.F. Shestakov, *J.de Chimie Physique* **92**, 362 (1995)
[14] L.P. Mezhov-Deglin and A.M. Kokotin, *JETP Letters* **70**, 11 (1999)
[15] V. Kiryukhin, B Keimer, R.E. Boltnev, V.V.Khmelenko, E.B. Gordon, *Phys. Rev. Lett.* **79**, 1774 (1997)
[16] J.D. Reppy, *J. Low Temp. Phys.* **87**, 205 (1992)
[17] J.M. Kosterlitz and D.J.Thouless, *J. Phys.* **C6**, 1131 (1973)
[18] L.S. Goldner, N. Mulders, and G. Ahlers, *J. Low Temp. Phys.* **93**, 131 (1993)
[19] M.H.W. Chan, K.I. Blum, S.Q. Murphy, G.K.S. Wong and J.D. Reppy, *Phys. Rev. Lett.* **61**, 1950 (1988)
[20] J. Yoon and M.H.W. Chan, *Phys. Rev. Lett.* **78**, 4801 (1997)
[21] J. Yoon, D. Sergatskov, J. Ma, N. Mulders, M.H.W. Chan, *Phys. Rev. Lett.* **80**, 1461 (1998)
[22] K.L.Warner, J.R. Beamish, *Phys. Rev. B* **36** , 5698 (1987)
[23] N. Mulders, J.R Beamish, *Phys. Rev. Lett.* **62**, 438 (1989)
[24] K.Warner, J.R.Beamish, *Phys. Rev. B* **50**, 15 896 (1994)
[25] M.A. Biot, *J. Acoust. Soc. Am.* **28**, 168 (1956)
[26] M.A. Biot, *J. Acoust. Soc. Am.* **28**, 179 (1956)
[27] S.I.Kiselev, V.V. Khmelenko, D.A. Geller *et al. J. Low Temp. Phys.* **119**, 357 (2000)
[28] M.J. McKenna, T. Slawecki, J.D.Maynard, *Phys. Rev. Lett.* **66**, 1878 (1991)
[29] E.B. Gordon, L.P. Mezhov-Deglin, O.F. Pugachev, V.V. Khmelenko, *Cryogenics* **9**, 555 (1976)
[30] C.E. Chase, *Physics of Fluids* **1**, 3 (1958)
[31] P. Meakin, *Ann. Rev. Phys. Chem.* **39**, 237 (1988)
[32] E.B. Gordon, A.A. Pelmenev, O.F. Pugachev, and V.V. Khmelenko, *Sov. J. Low Temp. Phys.* **11**, 307 (1985)
[33] B.D. Josephson, *Phys. Lett.* **21**, 608 (1966)
[34] G. Nunes, Jr. *Rev. Sci. Instr.* **61**, 1154 (1990); Ph.D. Thesis, Cornell University
[35] L.B. Knight, Jr., W.E. Rice, *et. al.*, *J. Chem. Phys.* **109**, 1409 (1998)

Transient processes in normal to superfluid transition in the presence and absence of gravity

Akira Onuki
Kyoto University

I would like to discuss how a normal fluid state is changed into a superfluid state. For example, if a bottom boundary is cooled through the lambda transition, a superfluid region expands from the bottom in the upward direction. There, a strong thermal counterflow is transiently induced to subtract entropy stored in the upper normal fluid region. In gravity the resultant vortex line density can attain the theoretical maximum if measured in units of the correlation length. We discuss how gravity affects such vortices and controls the speed of the normal fluid expansion.

Experimental Evidence For The Josephson Effect In Superfluid ^{4}He

Dave Pearson, JPL

We present here preliminary data that we believe to be the first experimental observation of the Josephson effect in ^{4}He. The flow of superfluid ^{4}He through a weak link was studied in a double-holed Helmholtz oscillator. The weak link consisted of an array of apertures, each of which was in the shape of a slit with a width of ~0.17 micron. The oscillator was driven at resonance and the amplitude and frequency of the oscillations were measured. The dependence of the resonance frequency on the amplitude of oscillations is analyzed to give the current-phase relationship through the weak link. At temperatures close to the lambda transition, an almost sinusoidal I(phi) is observed.

Susceptibility Crossover Behavior in ^{3}He and Xe Near Their Liquid-Vapor Critical Point - A Progress Report

Horst Meyer

Department of Physics, Duke University, Durham, NC 27708-0305

A discussion is presented on the crossover of the susceptibility from mean-field to Ising critical behavior upon approaching the critical point from below and from above T_c, both for ^{3}He and Xe. Fits of the experimental susceptibility data are made to curves from Monte Carlo simulations, and the corresponding Ginzburg numbers G_i for each measured property are deduced. Also the first correction amplitudes for the confluent singularities are obtained from the fit of the data. The respective ratios of these numbers and those obtained for the coexistence curves for ^{3}He and Xe, presented elsewhere, are discussed in terms of predictions.

I. INTRODUCTION

The interest in crossover phenomena from the asymptotic to mean-field critical behavior in fluids has been described in detail in a recent review article by Anisimov and Sengers [1], which lists many references and where different theoretical approaches and also a comparison with some experiments are presented. The subject of a recent paper [2] was a comparison between predictions for the crossover from Monte Carlo calculations [3] and experimental data of simple fluids. The susceptibility χ^+ above T_c (or compressibility) and the liquid and vapor densities along the coexistence curve (CXC) for Xe and ^{3}He were studied. From a fit of the data to the predicted curves, the corresponding Ginzburg numbers G could be estimated. For the CXC, the exit of the fluid from the critical regime into a background behavior could be clearly seen by a systematic departure from the predicted curve, well before the regime of mean-field critical behavior could be reached. For χ^+, the behavior of

Xe, a "classical fluid", agreed well with predictions, but there were systematic differences for ^{3}He, and a qualitative discussion was made in terms of the interplay between quantum and critical fluctuations for this fluid.

The purpose of this progress report is to extend the same analysis to the susceptibility χ^- data below T_c for Xe and ^{3}He, and also to give a status report on this program. After a background review, the susceptibility data of several experimental groups, namely along the critical isochore ($T > T_c$) and along the liquid and the vapor side of the CXC ($T < T_c$), are discussed. Comparison is made with curves from Monte Carlo calculations [3], and the corresponding Ginzburg numbers G(χ^-) are estimated. The internal consistency for the Ginzburg numbers so obtained is checked by determining G from the fit of data to a 2-term series expansion representing part of the curve obtained from the MC calculations. From the collection of Ginzburg numbers obtained so far [$G(\chi^+)$,$G(\chi^-)$ and $G(CXC)$], their ratios are discussed in the light of predictions. In spite of the uncertainties in the G(χ^-) below T_c due sparsity of data and experimental scatter, and also in the G(χ^+) for ^{3}He, some preliminary conclusions can be made. This progress report is to draw attention to the interest of such results, to their present incomplete understanding and to the great need of better data.

II. A SHORT REVIEW

A. Properties considered

We now list the properties discussed in this paper, and introduce the definitions of reduced temperature and density, $t \equiv (T - T_c)/T_c$ and $\Delta\rho \equiv (\rho - \rho_c)/\rho_c$. The coexistence curve is expressed by

$$\Delta\rho_{LV} = (\rho_{\text{liq}} - \rho_{\text{vap}})/\rho_c = B_0(-t)^\beta[1 + B_1(-t)^{\Delta_1} + B_2(-t)^{\Delta_2}...] \qquad (1)$$

where ρ_{liq}, ρ_{vap} and ρ_c are the densities in the coexisting liquid and vapor phases, and at the critical point. Furthermore $\beta = 0.326$ is the critical exponent and the bracket includes the correction-to-scaling confluent singularity terms. Here the B_i's are amplitudes characteristic of the fluid, and $\Delta_1 = 0.52$, $\Delta_2 = 1.04$ are the exponents obtained by Wegner [4] and by Newman and Riedel [5].

The susceptibility χ of the fluid, namely the analog of the susceptibility of a magnet, is given by $\chi \equiv (\partial\rho/\partial\mu)_T = \rho^2\beta_T$, where β_T is the isothermal compressibility and μ is the chemical potential. As discussed by Sengers and Levelt Sengers [6], the 3-D lattice-gas model (which corresponds to the 3-D Ising model in magnets) has properties that adequately describe real fluids. One particular aspect is that of symmetry in the $\mu - \Delta\rho$ plane. (In this respect, ^{3}He is the fluid that best conforms to this model. See Appendix) As a consequence, the derivative χ is a symmetric function of $\Delta\rho$ along an isotherm. Hence below T_c, one obtains $\chi_{Liq} = \chi_{Vap}$, where the susceptibilities are measured on both sides of the coexistence curve, and therefore we expect consistency between the data on both liquid and the vapor sides. Here we introduce the reduced quantity $\chi^* \equiv \chi(P_c/\rho_c^2)$, where the critical parameters have been listed in ref. [2]. Above T_c and along the critical isochore, $\chi^* = \beta_T P_c$.

Similarly to Eq.1, the expansion for the susceptibility $\chi^{*(+,-)}$ from the asymptotic critical regime is given by

$$\chi^{*(+,-)} = \Gamma_0^{(+,-)}|t|^{-\gamma}[1 + \Gamma_1^{(+,-)}|t|^{\Delta_1} + \Gamma_2^{(+,-)}|t|^{\Delta_2} + ...] \tag{2}$$

where the indices + and - indicate the region $t > 0$ along the critical isochore and $t < 0$ along the coexistence curve, respectively. Here again the Γ_i's are amplitudes characteristic of the fluid and $\gamma = 1.24$ is the critical exponent. The ratio Γ_0^+/Γ_0^- for a given fluid has been calculated from series expansion by Liu and Fisher to be [7]

$$\Gamma_0^+/\Gamma_0^- = 4.95 \pm 0.15 \tag{3}$$

This compares with the value of 4.82 obtained from the ratio $(\gamma/\beta)[(1-2\beta)\gamma/2\beta(\gamma-1)]^{\gamma-1}$ predicted from the parametric representation of the equation of state [8], where $\gamma = 1.24$ and $\beta = 0.327$ were used. The most recent values of this ratio (see [9]) are very close to 4.77. Predictions for the ratio of the amplitudes B_1, Γ_1^+ and Γ_1^- will be presented below.

B. Ginzburg numbers and amplitude ratios

The Ginzburg criterion and Ginzburg number have been discussed in detail in the article by Anisimov, Kiselev, Sengers and Tang [10] on the crossover approach to global critical phenomena in fluids. The Ginzburg number G is seen as a dimensionless temperature, obtained from the criterion $t \gg G$ which gives an estimate for the range of t, where the classical critical theory is valid, this is where the fluctuation contribution is small. For fluids, an order of magnitude estimate [10] of G leads to $\approx 10^{-2}$, and furthermore for a 3-D fluid, one finds $G \propto R^{-6}$, where R is the normalized molecular interaction range [10]. Hence the asymptotic critical behavior takes place for $t \ll G$ while the classical critical behavior is expected for $1 \gg t \gg G$. However as pointed out in ref. [1], in ordinary fluids the crossover is never completed in the critical domain ($t \ll 1$) since R is of the same order as the distance between molecules. The Monte Carlo algorithm developed by Luijten and Bloete [11] allows the full crossover region in 3-D Ising models to be covered. The calculation then gives a curve of a given singular property $f_i = f_i(|t|/G_i)$ covering ≈ 8 or more decades in $|t|/G_i$, and is clearly more complete than the expansion series expressed in correction-to scaling terms of series. A simple check for the internal consistency in determining G can be made by the expected expansion in terms of the corrections-to-scaling confluent singularities as

$$f_i = A_{0,i}|t|^{-\lambda_i}[1 + A_{1,i}(|t|/G_i)^{\Delta_1} + ...] \tag{4}$$

where the amplitude $A_{0,i}$ is non-universal but where the numerical coefficients $A_{1,i}$, and the exponent λ_i are universal for all fluids and characteristic of the property (susceptibility, CXC etc...). A fit of the curves $f_i = f_i(|t|/G_i)$, calculated by the Monte Carlo approach [3], to Eq. 4 (restricted to the region of $|t|/G_i$ where higher terms are negligible) gives $A_1(\chi^+) = 0.10$, $A_1(\chi^-) = 0.65$, and $A_1(CXC) = 0.23$.

Of particular interest here is the calculation of the susceptibility χ, both below and above T_c, represented in a very sensitive way by the plot [3] of the effective exponent γ_{eff}, which is given by the derivative

$$\gamma_{\text{eff}} \equiv -\frac{d\ln\chi_T^*}{d\ln|t|}. \tag{5}$$

In Fig.1, the plots of $\gamma_{eff}^{(+,-)}$ versus $|t|/G^{(+,-)}(\chi)$ for $t > 0$ and $t < 0$, as obtained from Monte Carlo calculations, are presented side-by-side for comparison. The various symbols denote the successively larger values of the interaction range R that were used to generate the master curve as the distance from T_c is increased. The lines labeled "BK, BB and SF" for $t > 0$ and "App" for $t < 0$ are theoretical curves described in ref. [3]. The slope of the exponent,$-\partial\gamma_{\text{eff}}/\partial\ln|t|$, gives information on the crossover width between the asymptotic Ising value of $\gamma = 1.24$ and the mean-field one $\gamma = 1$. This width is shown to be much narrower for the region $t < 0$ than for $t > 0$, as was pointed out in ref. [3]. We shall see that this difference in crossover width is reflected in the data for ^{3}He.

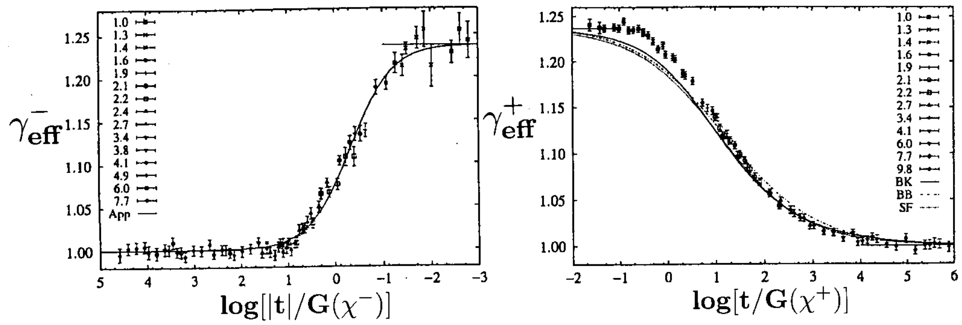

Figure 1: The effective exponents γ_{eff}^- for $t < 0$ (left side) and γ_{eff}^+ for $t > 0$ (right side) as a function of $|t|/G^{(+,-)}(\chi)$. This figure has been reproduced from the paper by Luijten and Binder where the symbols (Monte Carlo calculations) and the curves (predictions "BB","BK" and approximation "App") are described.

The relations between the G's and the first Wegner terms in the correction to scaling follow from Eqs, 1, 2 and 4. For instance in the case of the susceptibility above T_c, one has

$$\Gamma_1^+ = A_1(\chi^+)[G(\chi^+)]^{-\Delta_1} \tag{6}$$

with $\Delta_1 = 0.5$, which will be used in the discussion of the data analysis.

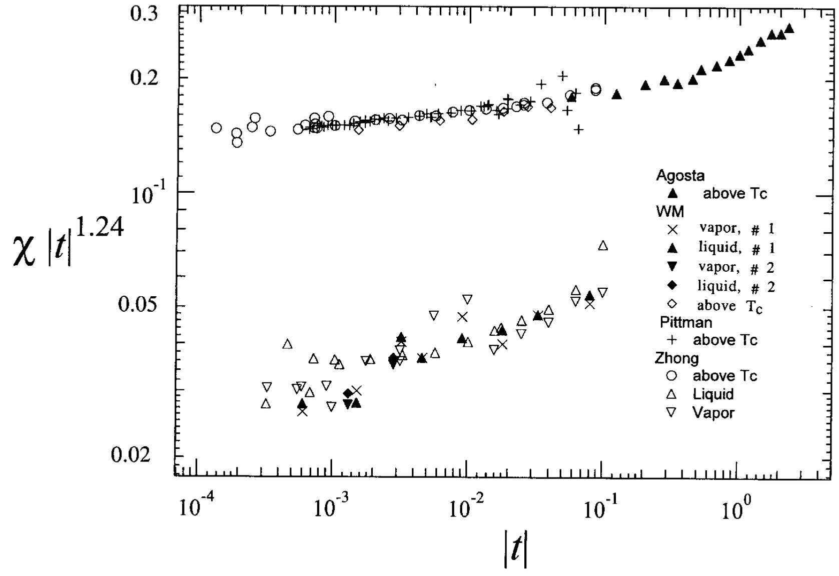

Figure 2: Experimental reduced susceptibility (χ^*) data from for ^{3}He above and below T_c (upper and lower figures) versus $|t|$ The references are respectively Agosta:[18];WM:[17]; Pittman:[20]; Zhong:[19] taken at the JPL laboratory

Aharony and Ahlers [12] have discussed the ratios of the amplitudes of the "correction-to-scaling confluent singularity" terms in expressions such as Eqs. 1 and 2 for different properties, and in particular for the order parameter (here CXC) and the susceptibility above T_c versus $|t|$. They expressed thermodynamic quantities with singularities at the critical point as

$$f_i = A_{0,i}|t|^{-\lambda_i}[1 + a_i|t|^{\Delta_1} + O|t|^{2\Delta_1}] \tag{7}$$

where λ_i is the (asymptotic) critical exponent of the property i, such as susceptibility, specific heat, order parameter etc.. and the a_i's are the amplitudes of the first correction-to-scaling term of the confluent singularity (already introduced here as Γ_1 and B_1). Among the relations they derived, one which considers the ratio of the correction term amplitudes for two properties i and j of a fluid is of particular interest to us, namely

$$(\lambda_{i,eff} - \lambda_i)/(\lambda_{j,eff} - \lambda_j) = a_i/a_j \tag{8}$$

Here $\lambda_{i,\text{eff}}$ is the effective exponent and $\lambda_{i\,\text{or}\,j}$ is the asymptotic exponent with $\lambda_i = \gamma = 1.24$ and $-\lambda_j = \beta = 0.326$. The numerical values for $\lambda_{i,\text{eff}}$ are obtained by fitting experimental data to a simple power law over the same range of $|t|$ where the fit to Eq. 7 has been made. A prediction of the ratio of Ginzburg numbers via Eqs.4 and 7 can therefore be made and compared with that from experiments. One has

$$(G_j/G_i) = [a_i A_1(j)/a_j A_1(i)]^{1/\Delta_1}. \tag{9}$$

Here $A_1(j)/A_1(i)$ is the ratio of the numerical coefficients in Eq.4 for the properties j and i, listed after Eq.4.

Bagnuls, Bervillier, Meiron and Nickel [13] have calculated the ratios a_i/a_j using "massive field theory" for the Φ^4 model in 3-D for the n=1 class. These ratios are universal and are found to be $a(\chi^+)/a(\chi^-) = \Gamma_1^+/\Gamma_1^- = 0.315 \pm 0.013$ and $a(\chi^+)/a(CXC) = \Gamma^+/B_1 = 0.9 \pm 0.2$. (See Tables VIII and IX of ref [13]). This implies that the ratio of the Ginzburg numbers is universal too. From Eq.9 one then obtains $\text{G}(\chi^+)/\text{G}(\chi^-) = 0.23 \pm 0.01$ and $\text{G}(\chi^+)/\text{G(CXC)} = 0.15 \pm 0.07$.

III. EXPERIMENTAL DATA AND DETERMINATION OF T_C

In the experiments, χ has been determined either from the intensity of light scattering (Xe) [14,15] or from the measurements of the density versus pressure along isotherms in Xe [16], and in ^{3}He [17,21,18,19] and from the vertical density gradient in the gravity field for ^{3}He [20] above T_c. Here we briefly comment on the various measurements and their respective scatter.

As will be seen below, the χ data for $t > 0$ have an appreciably higher accuracy than those below T_c. In the light scattering measurements, this might possibly be due to the added difficulty of sending the laser beam alternatively into the superposed liquid and vapor phases of a cell with a small height, and where the meniscus will become concave as T_c is approached, because of the decreasing surface tension. This contrasts with measurements above T_c where the beam is positioned near mid-height of the cell, and where the maximum light scattering intensity is observed by slowly scanning the vertical position. In the present analysis, the data by Smith et al [15] above T_c have not been used, because their scatter is larger than that of the more recent data by Güttinger and Cannell [14]. However we note that in ref [15] the amplitude ratio is $\Gamma_0^+/\Gamma_0^- = 4.1$, which is not far from the predictions. If the data of ref [14] above T_c are combined with those below T_c [15], a ratio of $5.8\pm$ 0.4 is obtained by fitting both sets of data to Eq. 2. The amplitudes are listed in Table I.

The maximum value of χ^+ at ρ_c from isotherm data above T_c is obtained with a higher precision than is the extrapolation of χ^- to the coexistence curve below T_c. As mentioned above, it is expected from the Ising model that $\chi_{vap} = \chi_{liq}$. Yet there can be appreciable scatter in both determinations which reflects the uncertainties both in the differentiations of the $\rho(P)$ data sets and also in the factor ρ^2_{Vap}, or ρ^2_{Liq}. The results are presented as reduced quantities $\chi* \equiv \chi P_c/\rho_c^2$, where the critical parameters have been listed in ref. [2]

In the experiments with Xe where optical methods were used, the determination of the critical temperature has been achieved for the χ measurements by observing the disappearance of the meniscus, and by a fit to Eq.2 [14]. The coexistence curve data were fitted to Eq.1 [22]. On the average these determinations were made with an uncertainty of $\delta t \approx \pm 5 \times 10^{-6}$.

By contrast in the experiments with ^{3}He without optical access, the uncertainty in T_c is more important. It is probably smallest in the experiments by Pittman et al. [20] where T_c was determined principally from measurements below T_c (coexistence curve), and where T_c was obtained from a fit of Eq.1, as described in that paper. Here the claimed uncertainty is $\delta T_c/T_c \approx \pm 9 \times 10^{-6}$. In the older measurements of χ from isotherms by Wallace and Meyer [17], the choice of T_c was obtained by extrapolation of both coexistence curve data and compressibility data, and based on a simple power law with effective exponents. The uncertainty was claimed to be $\delta T_c/T_c \approx \pm 6 \times 10^{-5}$. The use of this power law led to a systematic error in T_c which was evidenced by deviations from the compressibility data of ref. [20], as shown in Fig.1 of [20]. In the χ measurements by Chase and Zimmerman [21], also from isotherms, the determination of T_c was done in a similar way as in ref [17]. In the most recent measurements of χ from isotherms by the MISTE team at JPL [19], the value of T_c was determined from a fit of the χ data above T_c to Eq. 6 with a systematic uncertainty of $\delta T_c/T_c \approx \pm 1.5 \times 10^{-5}$ in T_c (F. Zhong, private communication).

IV. DATA PRESENTATION AND MONTE CARLO CALCULATIONS

In Fig.2 the susceptibility data for ^{3}He from refs [17,20,19,18] are presented, both above and below T_c, scaled by the leading singularity $|t|^{-\gamma}$. The data of ref [21] lie systematically up to 20% below the other data sets and have not been included in the plot to avoid overcrowding the figure. The data of ref [20] can be made to agree well with those of ref. [19], if their respective values of T_c are slightly shifted well within the stated uncertainty mentioned above. The shifts are as follows: $\delta T_c/T_c = +6 \times 10^{-6}$ for data of ref. [19] and $\delta T_c/T_c = -6 \times 10^{-6}$ for data of ref. [20]. By combining the two sets of data with the mutually shifted T_c, a fit to Eq. 2 gives $\Gamma_0^+ = 0.145$. For a given set of experiments,where data above and below T_c were obtained, the same choice of T_c was implemented. The error in T_c in the experiments of ref [17] was corrected by an appropriate shift δT_c withing the stated uncertainty, which resulted in the data above T_c to lie uniformly $\approx$ 5% below those of refs. [20] and [19].

Table I lists the amplitudes of the leading terms Γ_0^+, Γ_0^- and B_0, and of the first correction terms Γ_1^+, Γ_1^- and B_1 obtained by a fit of the data to Eq.1 resp. Eq. 2. The errors listed are all systematic, not statistical. The corresponding sources of data are listed in the last column. The data fits for Γ_1^+ and Γ_1^- in ^{3}He and for Γ_1^- in Xe (with very scant data and appreciable scatter close to T_c) were made by setting the higher terms in Eq. 1 to zero. To this purpose, the fitting was restricted to the range $|t| < 2 \times 10^{-2}$, where presumably the higher terms in Eqs. 1, 2 (and therefore also in Eq. 4) can be neglected. Because of the strong correlation between the amplitudes in the data fitting procedure to Eqs 1 and 2, an uncertainty of only say O(±5%) in Γ_0 can produce a much larger one of O(±50%) in Γ_1. For the CXC of ^{3}He and Xe, and for Γ_1^+ of Xe, the amplitudes listed in refs [14,20,22] were used.

The ^{3}He data by Pittman et al., which result from measuring the density difference between two superposed sensors, show a smaller scatter close to T_c than those ref. [19], but they are restricted to the range $t > 5\times10^{-4}$, below which the vertical density profile becomes sharply non-linear as stratification from gravity increases. Above $t > 5 \times 10^{-2}$, where χ has become small, this method is no longer sensitive, as shown by the rapidly increasing scatter. One notes that for the ^{3}He χ^- data, the leading amplitude Γ_0^- is consistent well within the large scatter with the expected $\Gamma_0^- = \Gamma_0^+/4.95 = 0.029$ where the factor 4.95 was given in Eq. 3. Here we have taken $\Gamma_0^+ = 0.145$, the value from the combined set of data from refs. [20] and [19]. In spite of the data scatter below T_c, the difference in the change of $\chi\,|t|^{1.24}$ with $|t|$ in the regime above and below T_c is quite striking : $\mathcal{R}(\text{t=0.1})/\mathcal{R}(\text{t}\rightarrow 0) = 1.25$ compared to $\mathcal{R}(\text{-t=0.1})/\mathcal{R}(\text{t}\rightarrow 0) = 1.93$, where $\mathcal{R}(\text{t}) \equiv \chi|t|^{1.24}$. This is consistent with the finding that $\gamma_{eff}(t < 0)$ is smaller than $\gamma_{eff}(t > 0)$ over the common experimental range $10^{-3} < |t| < 10^{-1}$. As was mentioned before, MC calculations predict that the crossover width is narrower for $t < 0$ than for $t > 0$.

In Figs. 3 and 4, plots of the scaled reduced and normalized susceptibility $\bar{\chi}\,|t|^{1.24}$ versus $|t|/G(\chi^{(+,-)})$ are shown. Here $\bar{\chi} = \chi^*/\Gamma_0^{(+,-)}$, as in ref. [2]. In each figure the subscripts indicate the phase (vapor or liquid) along the coexistence curve. In the limit $|t| \rightarrow 0$ the ratio $\bar{\chi}\,|t|^\gamma$ becomes unity. However the MC calculations for $t < 0$ have more scatter than for $t > 0$ as seen from Fig.1. In spite of this, their trajectory for $[(-t/G] < 1 \times 10^{-2}$ can be estimated quite well, since with decreasing $|t|$ the curves will follow Eq.4, and tend to unity. The values of the Γ's and $G(\chi^+)$ obtained via Eq. 6 and similarly of $G(\chi^-)$ and $G(CXC)$ for both fluids are shown in Table 1.

In Fig.3 both the susceptibilities [14,16,15] above and below T_c for Xe are presented, - the first one already shown in ref [2]. Below T_c, there are few data points, and the scatter prevents a precise determination of Γ_0^- and therefore the resulting value of $\mathrm{G}(\chi^-)$ is much more uncertain than that of $\mathrm{G}(\chi^+)$. It should be mentioned, as was done in ref. [2], that the fit for $t > 0$ was made taking $\Gamma_0 = 0.0594$ instead of 0.0577 obtained in ref. [14]. This choice of Γ_0, determined by the adopted value of $\gamma = 1.240$, is no doubt responsible for the different values of $\mathrm{G}(\chi^+)$ obtained from the data fit to Eq.2 and to the MC curve, respectively 0.006 amd 0.018, as reported in ref [2].

Fig.4 shows the plots for ^{3}He of refs [20,19,17,18] of Fig.2, with $\Gamma_0^+ = 0.145$. For χ^-, the value $\Gamma_0^- = 0.029$ mentioned above was used, which "anchors" the data presentation $\bar{\chi}\, t^{1.24}$ in the asymptotic regime. The fit according to Eq.2 is restricted to $|t| < 3 \times 10^{-2}$. The top plot is different from that of ref [2] as it combines the data of refs [19] and [20] as has been described above. The new value of $\Gamma_0^+ = 0.145$ (instead of 0.139) then leads to a larger value of $\mathrm{G}(\chi^+)$, listed in Table 2. [By accident, in the bottom plot for $t < 0$, the symbols WM(vapor) and JPL (liquid) on one hand, and WM(liquid) and JPL(vapor) on the other, are undistinguishable]. It is clear that the restricted data range in $|t|/\mathrm{G}(\chi^-)$ for ^{3}He below T_c does not enable confirming the variation of the quantum fluctuations in the crossover region, proposed for $t > 0$ [2], where the data extend beyond $t = 10^{-1}$.

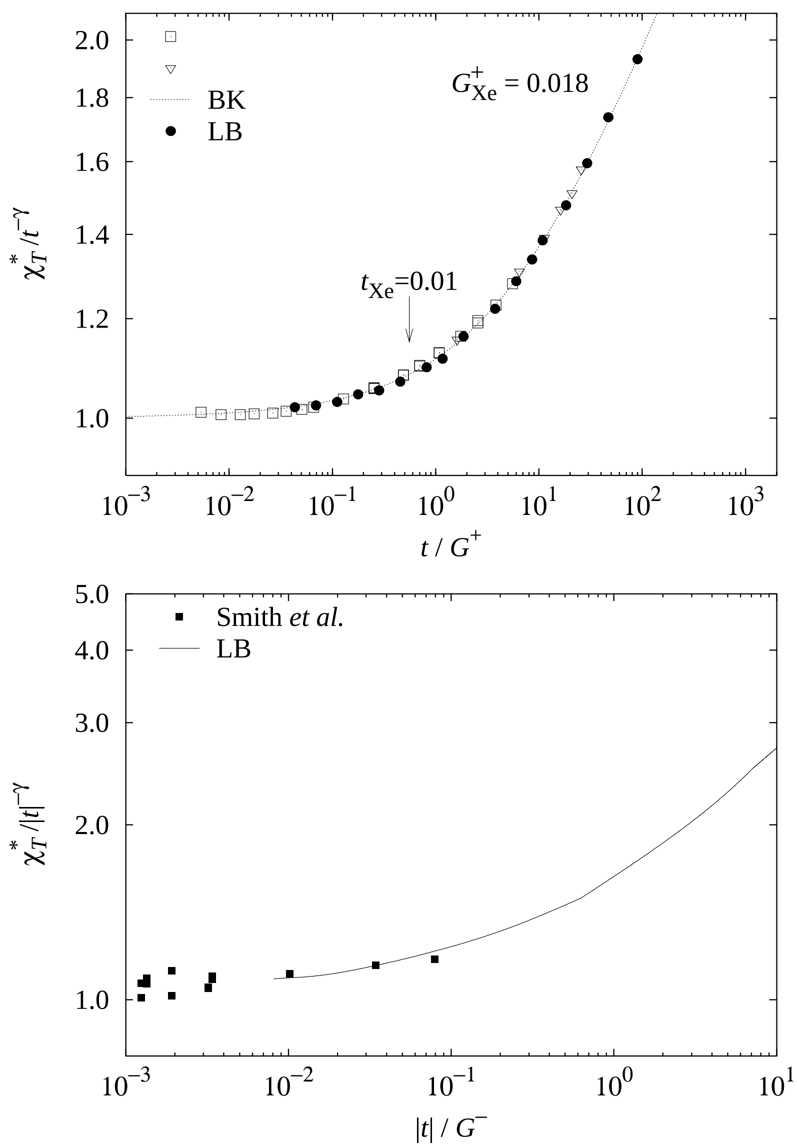

Figure 3: Experimental susceptibility data for Xe above and below T_c (upper and lower figures) versus $|t|/G(\chi^{(+,-)})$, fitted to the Monte Carlo calculations (solid circles LB and lines LB). Dotted line: Renormalization Group (BK) for Belyakov and Kiselev, referred to in [3]. Experimental data: open squares: [14], open inverted triangles:[16], solid squares:[15]. Here the χ^*'s have been divided respectively by Γ_0^+ and Γ_0^-

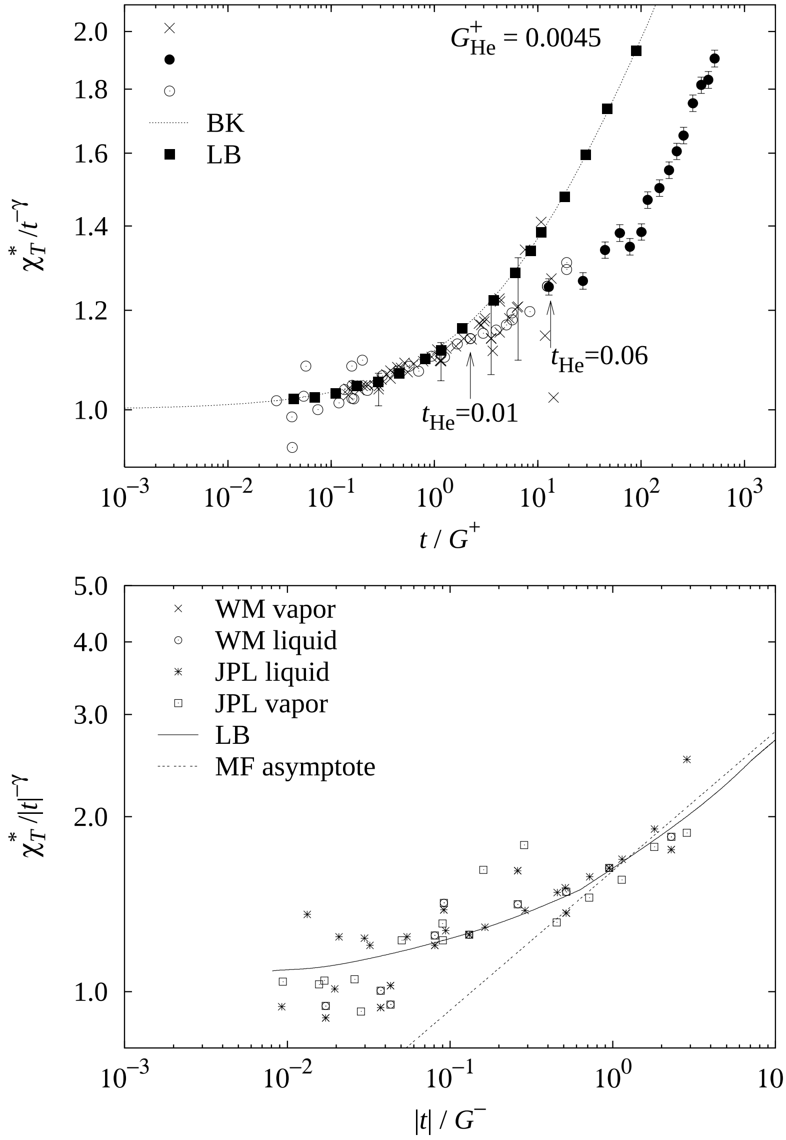

Figure 4: Experimental susceptibility data for ^{3}He above and below T_c from fig.2, (upper and lower figures) versus $|t|/G(\chi^{(+,-)})$, fitted to the Monte Carlo calculations (solid squares (LB) ($t > 0$) and solid line ($t < 0$). Dotted line: Renormalization Group (BK), as described in [3]. Dotted line labeled MF: Mean Field asymptote. Experimental data for $t > 0$: X:[20]; solid circles:[18]; open circles [19]. For $t < 0$: WM :[17]; JPL: [19]. Here the χ^*'s have been divided respectively by Γ_0^+ and Γ_0^-

V. DISCUSSION

In Table 1, the values of the first correction term amplitudes, obtained from a fit of the experimental data to Eqs.1 and 2 are obtained and their ratios are compared with predictions [13]. The large (systematic) error bars reflect the data scatter and fit quality. A fair consistency within the large uncertainties is obtained, indicating that the result from the data analysis appears consistent with the universality prediction based on the Φ^4 model.

In Tables 1 and 2, the Ginzburg numbers and relevant ratios are listed, and the results are now briefly discussed. Here again the error bars are guesses based on the fitting uncertainties, since a satisfactory error calculation could not be done. In Table 2, the G's are those obtained by a fit of the data to the curve obtained from Monte Carlo calculations. Obviously one of the great merits of MC calculations is to give a much wider range of $|t|/G$ where the data can be fit to predictions than can a 2-term expansion such as Eqs 1 and 2. At the same time, it is instructive to compare the resulting G's obtained from both methods.

Fluid	Γ_0	Γ_1	B_0	B_1	G() from $\Gamma_1^{(+-)}$, B_1	Refs.
Xe	[+] 0.0577	[+] 1.29±0.2	-	-	(χ^+) 0.006	Guettinger&Cannell
	[-] 0.013	[-] 1.4±0.5			(χ^-) 0.2	Smith et al.*
-			1.47	1.17	(CXC) 0.035	Naerger&Balzarini
^{3}He	[+] 0.141	[+] 1.5±0.2			(χ^+) 0.0044	Pittman et al.*
	[+] 0.150	[+] 0.98	-	-	(χ^+) 0.010	JPL,(Barmatz et al.*)
	[+] 0.145	[+] 1.3±0.2	-	-	(χ^+) 0.006	JPL/Pittman*
	[-] 0.029	[-] 3.6±0.3			(χ^-) 0.034	JPL/Wallace *
			1.02±0.02	0.90±0.1	(CXC) 0.06±0.02	Pittman et al.
	Γ_1^+/Γ_1^-	Γ_1^+/B_1				
Xe	0.9±0.4	1.1±0.3				Same refs. as above
^{3}He	0.36±0.07	1.4±0.3				JPL/Wallace/Pittman
Theory	0.315±0.013	1.1±0.2				Bagnuls et al.

Table 1: Amplitudes for the expansions in Eqs 1 and 2 for χ^+, χ^- and CXC, as obtained from fits in various experiments, and the corresponding Ginzburg numbers deduced from the amplitudes a_i in Eq.6 and similar. The symbol " * " indicates that the expansion was limited to the first correction term and to $|t| < 10^{-2}$. The bottom three rows show the comparison between the experimental and the predicted (universal) ratios of the first correction amplitudes. For^{3}He, $\Gamma_1^+ = 1.3$ was used.

Fluid	$G(\chi^+)$ $\times 10^2$	$G(\chi^-)$ $\times 10^2$	$G(CXC)$ $\times 10^2$	$G(\chi^+)/G(\chi^-)$	$G(\chi^+)/G(CXC)$
Xe	1.8±0.3	10±5	7±2	0.18±0.08	0.26 ±0.06
^{3}He	0.25±0.15 * 0.45±0.2 **	3.5±2	7±2	0.07±0.04 0.13±0.05	0.036±0.02 0.064±0.03
Eqs.8 and 9				$0.02 \rightarrow 0.2$	0.10±0.02
Bagnuls et al. with Eq. 9				0.23±0.01	0.15±0.07

Table 2: The Ginzburg numbers, as obtained from fits of the data to Monte Carlo calculations, and their ratios, with estimated uncertainties, and comparison with predictions via Eq. 8 of ref[12] and Eq. 9. Notation indices: “ * ” obtained with Pittman data and $\Gamma_0^+ = 0.140$. “ ** ” obtained with combined Pittman/JPL data and $\Gamma_0^+ = 0.145$. The numerical values in the bottom row are those predicted in Ref.[13] with use of Eq.9.

This is done by comparing the numbers in the last column of Table 1 with those on the first three columns in Table 2. On the whole, there is acceptable consistency between the determination from both methods, with the exception for Xe. This might be caused by the different choices of Γ_0 for the the χ^+ data, as mentioned before.

We note that the Ginzburg numbers have uncertainties that reflect the degree of difficulty in fitting the data to the curve obtained from Monte Carlo calculations. Yet, even with this caveat, certain tentative conclusions can be reached. First, the order of magnitude of the G_i is as expected [1], namely $O(10^{-2})$. Second, the ratios $G(\chi^+)/G(\chi^-)$ are roughly the same for Xe and ^{3}He, within the stated uncertainty. From [12] it is not clear whether there should be universality for this ratio or for $G(\chi^+)/G(CXC)$, where the experimental values for both fluids are different. But as noted before, universality for the ratios of the first correction term amplitudes is predicted from the Φ^4 model [13], and therefore the ratios of the corresponding Ginzburg numbers, obtained via Eq.9, are universal too.

We now compare the ratios with those expected, based on ref [12]. For ^{3}He, the measured effective exponents for χ were $\gamma^+_{eff} = 1.19$ [17,21,20] and $\gamma^-_{eff} = 1.08$ [17,21] over the range $5 \times 10^{-4} < |t| < 5 \times 10^{-2}$. When these χ data were published, this result was very surprising, because it was expected that the exponents should be the same both above and below T_c. However in the light of the Monte Carlo calculations that show the crossover to be quite different on both sides of T_c (See Fig.1), this discrepancy in the values of γ_{eff} can be understood. Interestingly the susceptibility data for Xe [15] do not show this difference, and both effective exponents are listed [15] as $\gamma_{eff}^{(+,-)} = 1.21$ over the range $2 \times 10^{-4} < |t| < 8 \times 10^{-3}$. For the coexistence curve, the effective exponent has been reported to be $\beta_{eff} = 0.360$ for ^{3}He [17,21,20] and 0.355 for Xe [23].

The predicted ratios $G(\chi^+)/G(CXC)$ and $G(\chi^+)/G(\chi^-)$ from Eqs.8 and 9, and from Bagnuls et al. [13] via Eq.9 are listed in Table II. Starting with the results from ref. [12], $G(\chi^+)/G(CXC) \approx 0.10$ is determined from the effective exponents and lies in between the values listed for Xe and ^{3}He. This prediction, which is consistent with the value obtained by Bagnuls et al., is then good to within say ± 20%. There is agreement within the combined uncertainties for ^{3}He , but not so for Xe. The prediction of the ratio $G(\chi^+)/G(\chi^-)$ from ref. [12] with Eq.8, is uncertain : if $\gamma_{eff}^+ = \gamma_{eff}^-$ is taken, as appears to be the case for the Xe data, the ratio is 0.2. However when the values for γ_{eff}^+ and γ_{eff}^- for ^{3}He are used, as listed above, the ratio becomes 0.02 ! The first value is consistent with the predictions by Bagnuls et al.. Overall the experimental data analysis in terms of the correction term amplitudes a_i and the G_i's is still in a preliminary state and further progress is needed.

VI. CONCLUSION

A status report has been presented of the program describing the crossover from asymptotic to mean-field behavior in different properties for two simple fluids. So far, our understanding is incomplete, since the accuracy of several sets of experimental data needs substantial improvement. By contrast, MC calculations [3] are making precise predictions of the crossover for the susceptibility χ^+ and χ^- as well as the coexistence curve in terms of Ginzburg numbers. Also there are quantitative predictions of the ratios of the correction term amplitudes [13].

In spite of the uncertainty in experimental data, some conclusions can be reached. The Ginzburg numbers for χ and CXC in ^{3}He and Xe and their ratios have been obtained from a data analysis. The latter were compared with predictions and discussed. Also from the ratios of the first correction term amplitudes B_1, $\Gamma_1(\chi^+)$ and $\Gamma_1(\chi^-)$, there appears confirming evidence of their predicted universality within the large uncertainties. Further progress can be expected when better experimental data of the susceptibility of Xe and ^{3}He below T_c, and over a larger temperature range have been obtained.

VII. ACKNOWLEDGMENTS

This research was supported by NASA grant NAG 3-1838. The greatest debt of gratitude goes to E. Luijten for the very stimulating and informative interactions with him and for his generous effort in preparing several plots. Furthermore he made a detailed criticism of this paper. I am also indebted to A. B. Kogan for his help with the plots in Fig.2, with data fitting and for his technical help with the formatting, to G.O Zimmerman for supplying an original figure of the Chase and Zimmerman χ data, to M. Barmatz and F. Zhong for permission to use the unpublished χ data (labeled Zhong and JPL in the figures) obtained in the JPL MISTE project, and to M. Giglio for supplying tabulations of χ^- in Xe. I am very grateful to J.M.H. Levelt Sengers for correspondence on the V.d.W. model and to F. Zhong for comments on this report and for very useful suggestions. Finally I am indebted to C. Bervillier for correcting some references, and to him and to E. Vicari and A. Pelissetto for bringing those in [9] to my attention.

VIII. APPENDIX

A. Extension of the rectilinear diameter above T_c ?

In the course of the data analysis for obtaining the χ^+ of Xe from ref. [16], the location of the maximum for χ^+ with respect to the critical isochore was determined. This line of points might be thought to extend the trajectory of the rectilinear diameter as T increases and passes the critical point. Over the whole range of the data ($t < 0.47$) it was found to have a slope $\Delta\rho/t$ = - 0.049, to be compared with the slope of - 0.725 for the rectilinear diameter [23]. In the Ising model, the slope is zero for both lines. Similarly the Van der Waals model predicts the rectilinear diameter slope as -2/5 [6], and from an expansion above T_c the slope for the maximum of χ^+ to be zero [24]. Hence there is a slope discontinuity in the same direction as observed in Xe. For ^{3}He, experiments give a rectilinear diameter slope of +0.022 [20]. Above T_c from an inspection of the the maximum location in χ^+ in the data analysis of various experiments [25], the slope is found to be zero within experimental error over the range $t < 2 \times 10^{-1}$. Beyond this range, the χ^+ versus ρ curve along an isotherm is no longer symmetric with respect to ρ_c and as t increases, the maximum of χ^+ shifts to larger densities.

---

[1] M.A. Anisimov and J.V. Sengers " Critical and Crossover Phenomena in Fluids and Fluid Mixtures" To appear in "Supercritical Fluids-Fundamentals and Applications" E. Kiran, P.G. Debenedetti and C.J. Peters, Eds, (Kluwer, Dordrecht).

[2] E. Luijten and H. Meyer, Phys. Rev. E **62** 3257 (2000).

[3] E. Luijten and K. Binder, Phys. Rev. E **58** 4060(R) (1998).**59** 7254(E) (1999).

[4] F. Wegner, Phys. Rev. B **5** 4529 (1972).

[5] K.E. Newman and E.K. Riedel, Phys. Rev. B **30** 6615 (1984).

[6] J.V. Sengers and J.M.H. Levelt Sengers, "Critical Phenomena in Classical Fluids", in Progress in Liquid Physics, C.A. Croxton, ed. (Wiley, Chichester, UK, 1978) p. 103.

[7] A. Liu and M.E. Fisher, Physica **A 156** (35) 1989.

[8] P. Schofield, J.D. Litster and J.T. Ho, Phys. Rev. Lett. **23**, 1098 (1969).

[9] Further values for the ratio Γ_0^+/Γ_0^- are 4.77±0.3 by C. Bagnuls et al. (ref.13); 4.75±0.03 by M. Caselle and M. Hasenbusch, J. Phys. **A 30**, 4963 (1997); 4.73±0.16 and 4.79±0.1 by R. Guida and J. Zinn-Justin, J. Phys. **A31**, 8103 (1998), 4.77±0.02 by M. Campostrini, A. Pelissetto, P. Rossi and E. Vicari, Phys. Rev. **E 60** 3526 (1999) and 4.762±0.008 by P. Butera and M. Comi, Phys. Rev. **B 62** 14837 (2000).

[10] M.A. Anisimov, S.B. Kiselev, J.V. Sengers and S. Tang, Physica A, 188, 487 (1992).

[11] E. Luijten and H.W.J. Bloete, Int. J. Mod. Phys. C**6** 359 (1995).

[12] A. Aharony and G. Ahlers, Phys. Rev. Lett. **44**, 782 (1980).

[13] C. Bagnuls, C. Bervillier, D.I. Meiron and B.G. Nickel, Phys. Rev. B **35** 3585 (1987).

[14] H. Güttinger and D.S. Cannell, Phys. Rev. B **24** 3188 (1981).

[15] I.W. Smith, M. Giglio and G.B. Benedek, Phys. Rev. Lett. **27**, 1556 (1971).

[16] A. Michels, T. Wassenaar and P. Louwerse, Physics **20** 99 (1954).

[17] B.A. Wallace and H. Meyer, Phys. Rev. A **2** 1536 (1970). A tabulation of the susceptibility data is given in a technical report, Duke University (1972), unpublished.

[18] C.C. Agosta, S. Wang, L.H. Cohen and H. Meyer, J. Low Temp. Phys. **67**, 237 (1987).

[19] M. Barmatz, I. Hahn and F. Zhong, Proceedings of the 2000 NASA/JPL Investigators Workshop on Fundamental Physics in Microgravity, edited by D. Strayer, Solvang,CA, June 2000.

[20] C. Pittman, T. Doiron and H. Meyer, Phys. Rev. B **20** 3678 (1979) The fit of the χ^+ data was done to a series with two correction terms in Eq.2, namely leading to $\Gamma_0^+ = 0.139$, $\Gamma_1^+ = 3.2\pm1$ and $\Gamma_2^+ = -12\pm$ 14 (Their Table III). However in this fit the second term is very important, and through the strong correlation in the least squares fit, this term impacts on the value of Γ_0^+. Above the fit range of $t = 2\times10^{-2}$, the agreement with the data deteriorates very sharply. A fit with only the first term, more reasonable, gives $\Gamma_0^+ = 0.141$ and $\Gamma_1^+ = 1.5\pm0.2$ over the same range of t.

[21] C.E.Chase and G.O. Zimmerman, J. Low Temp. Phys. **24**,315 (1976)

[22] U. Naerger and D. Balzarini Phys. Rev. B **42** 6651 (1990)

[23] A.B. Cornfeld and H.Y Carr, Phys. Rev. Lett. **29**, 28 (1972).

[24] J.M.H. Levelt Sengers, Industrial and Engineering Fundamentals **9**, 470 (1970)

[25] From an unpublished analysis of ρ versus P data along isotherms from Agosta et al.(ref. 16)

Coalescence of Levitated He II Drops

George Seidel, C.L. Vicente, C. Kim, and H.J. Maris,
Brown University

We have initiated a study of the coalescence of superfluid helium drops levitated in a magnetic trap. Drops of up to 2 cm diameter, at temperatures down to 0.7 K, can be brought into contact with an impact velocity of a few cm/s. The evolution of the shape of the fluid upon coalescence is recorded with a high speed CCD camera. Movies of the fluid reveal interesting features of the motion of the surface. We a particularly interested in observing the growth of the neck joining the two drops immediately after contact. Different theoretical calculations predict that the growth of the radius of the neck should obey a scaling law and that toroidal voids should be entrapped during the growth process. In order to study these phenomena in detail, experiments may have to be performed on larger drops. Such experiments can only be done in space.

EXperiments Along Coexistence near Tricriticality (EXACT)

Melora Larson(a), Ashutosh Tiwari(b) , Masoud Mohazzab (b), Vladimir Dotsenko (b),
John Panek (a), Al Nash (a),and Norbert Mulders (b)

(a) Jet Propulsion Laboratory, California Institute of Technology
(b) Department of Physics and Astronomy, University of Delaware

Tricritical points are among the few physical systems for which Renormalization Group theory produces exact predictions. In fact, since D=3 is the marginal spatial dimension for tricriticality, the associated critical exponents are (exact) integer fractions with logarithmic corrections to this critical behavior. Therefore, the tricritical point in the helium-3/helium-4 phase diagram offers many unique opportunities to test the understanding of critical phenomena. To fully test these predictions, the inhomogeneities introduced by the diverging concentration susceptibility in the presence of gravity must be removed by performing the experiment in a micro-gravity environment. We present the results of our ground-based measurements of the superfluid density and the phase separation boundary. We have used a pulsed second sound technique to determine the superfluid density near the tricritical point. To minimize concentration gradients induced by the earth's gravitational field, the experiments were done in a 160mm thin layer of helium, bounded by two sapphire disks. We analyzed our second sound data within the framework of a model that explicitly takes into account the boundary conditions as well as the non-linear nature of the sound propagation in the mixture. To detect the phase separation boundary in the helium mixtures, we have developed two different capacitative sensors, a parallel plate geometry to make bulk concentration measurements, and an inter-digital capacitor to make local concentration measurements. The resolution and advantages of these two types of sensors will be presented along with our preliminary measurements of the phase separation boundary.

This work is supported by NASA.

Out of Equilibrium Nucleation in First Order Phase Transitions

Charles Elbaum
Brown University

We are studying the transition from superfluid helium-four to the bcc and hcp solid phases. In this process we are frequently observing nucleation of a non-equilibrium (metastable) solid phase. After times varying from a fraction of a second to tens of minutes, the stable phase nucleates (independently) from the liquid, and the non-equilibrium solid melts. We examined the possibility of accounting for these events in the context of traditional nucleation theory by using the known differences between the superfluid and the two solid phases (stable and metastable). The experimental results, however, are not consistent with this explanation nor, more generally, with predictions of traditional nucleation theory. We propose a new model in which the critical nuclei are initially the same for both solid phases, and in the following stage, before reaching macroscopic size, these nuclei transform into either the bcc or hcp phase.

Heat Capacity Enhancement and a New Surface Instability in Superfluid ^{4}He Under a Heat Current Near the Lambda Transition

Talso Chui, A. W. Harter, R. A. M. Lee, A. Chatto, Xinkai Wu, and D. L. Goodstein
JPL & Caltech

We report on results recently published in Physical Review Letters [1] on the enhancement of the heat capacity of superfluid ^{4}He under a heat current near the lambda transition. The observed enhancement is much larger than predicted by theory. We also propose a new way to interpret the data of a previous experiment on the depressed breakdown temperature of superfluid helium under a heat current. In our interpretation these observations may be accounted for by an instability in the singular Kapitza resistance at the hot endplate of the thermal conductivity cell, which is different from the breakdown of bulk superfluidity.

[1] Phys. Rev. Lett., 84, 2195 (2000).

Surface Physics with Helium Crystals in Microgravity

A. V. Babkin, R.V. Duncan, and A.Ya. Parshin, UNM
Y.-M. Liu, JPL

The equilibrium shape of any crystal is controlled by the thermodynamics of its surface. The microscopic structure of the interfacial boundary is strongly influenced by its crystallographic orientation, giving rise to a variety of surface phases. Each of these phases is mirrored in the particular details of the equilibrium crystal shape. From a practical point of view, a detailed knowledge of possible surface formations and their thermodynamic properties is of a great importance - these characteristics are mainly responsible for the growth properties of a crystal. However, in conventional solids the intrinsic properties of the interfaces are always obscured by the transport processes in the bulk phases.

An exceptional situation is found in the case of helium. The highly mobile superfluid liquid phase transports heat away quickly and the latent heat of solid formation is almost zero. As a result, the interface can relax very quickly making it possible to study directly its equilibrium properties. Helium is also an exceptionally pure material since all foreign substances are frozen out. An isotopic purity of one part in 10^{15} has been achieved in ^{4}He. The short shape relaxation time of ^{4}He crystals has enabled systematic experimental and theoretical studies of both their equilibrium and kinetic properties. However, since the equilibrium shape of a crystal is strongly affected by gravity, the interpretation of experimental results remains an extremely complicated task. This difficulty has led to a significant controversy between existing experimental observations obtained by various research groups. This controversy may only be resolved by making new measurements in the microgravity laboratory.

The proposed flight experiment represents a comprehensive microgravity investigation of the equilibrium and kinetic properties of the liquid/solid interface in helium. All experimental and theoretical activities proposed here are primarily focused on the development of a fundamental understanding of the interfacial phenomena on the liquid/solid interfaces. Some experiments will take advantage of microgravity environment to extend the scope and accuracy of ground-based measurements of the equilibrium and dynamic properties of crystal surfaces. Other experiments will attempt to test, for the first time, the universality of the roughening transition temperature as predicted by Kosterlitz-Thouless theory. Such measurements may only be reliably accomplished in microgravity.

The important thermodynamic parameters of an interface can be deduced directly from the equilibrium crystal profile, but only if the crystal is grown in microgravity. We will show that the scope of measurements can be significantly extended and their accuracy greatly improved, as compared to Earth-bound measurements. The results will provide new detailed knowledge about surface physics and crystallography.

We propose to measure the equilibrium shape of a helium crystal in the gravity-free environment over a wide temperature interval. In these measurements, a hierarchy of faceting (roughening) transitions on the crystal interface will be established and the angular plot of the surface free energy for each temperature will be determined. The results will be used to verify fundamental assumptions of modern theory. In microgravity, the critical behavior near the roughening transition temperatures could be examined with significantly improved accuracy by broadening the scope of our measurements toward previously inaccessible crystallographic orientations.

The proposed experiment will also measure fine details of the equilibrium crystal shape close to a facet edge. These measurements will yield new information about the microscopic surface organization. Current interfacial theoretical models will be tested directly on the basis of this information.

We will explore a wide spectrum of crystal growth phenomena. We are convinced that a faceted helium crystal in microgravity provides an ideal model to study basic growth mechanisms, such as spiral growth governed by screw dislocations and the two-dimensional nucleation of terraces.

A high-resolution, non-invasive optical method will be employed to visualize and quantify the crystal shapes and their morphology. This innovative imaging scheme will employ an optical interferometer with a cooled CCD camera. We will take full advantage of our previous experience with this powerful new measuring technique.

This proposed effort has inspired interest and scientific excitement throughout the world. Many leading international physicists including Prof. A.F. Andreev, Dr. O.A. Andreeva, Prof. A.Ya. Parshin, Prof. K.O. Keshishev (all from the Kapitza Institute for Physical Problems, Russia), Prof. M. Paalanen (Low Temperature Laboratory, Helsinki University of Technology, Finland), Prof. T. Mizusaki (Kyoto University, Japan), and Prof. Y. Okuda (Tokyo Institute of Technology, Japan) plan to propose to their respective agencies to obtain funds to conduct synergistic research. This will promote strong international collaboration in this area of science.

Phase Separation of ^{3}He-^{4}He mixtures in aerogel and progress toward a gravity-free demagnetization refrigerator

Jeevak Parpia, Wendy J. McRae, Gavin J. Lawes, Eric N. Smith, John Beamish*, and Norbert Mulders+
Department of Physics, Clark Hall, Cornell University, Ithaca NY
+Department of Physics, University of Delaware, Newark DE
*Department of Physics, University of Alberta, Edmonton, AL, Canada

We report on phase separation phenomena at temperatures below 100 mK in ^{3}He-^{4}He mixtures in 98% open aerogel. We describe the temperature dependence of the ^{4}He fraction (x_4) starting from a variety of ^{4}He concentrations. The measurements were carried out using a torsion pendulum that contained a capacitor into which the aerogel was grown that provides an in-situ measurement of the ^{4}He content in the aerogel. The cell was cooled by a high surface area sintered silver heat exchanger. Below x_4 of 10% (at 21.8 bar) we observe that the ^{4}He is expelled from the aerogel as the temperature is lowered. For these concentrations the limiting low temperature value of x_4 is 4%, corresponding to the so-called inert layer. If we start with x_4 greater than 12%, the ^{4}He is drawn into the aerogel as the temperature is reduced. These previously unobserved phenomena are likely due to the competition between surface tension and the different pore geometries of the aerogel and silver sinter. It is clear that the ^{4}He is stable against the gravitational potential for x_4 <40%, and above these concentrations there is a catastrophic invasion of the ^{4}He-rich phase into the aerogel. We will also report on progress toward a demagnetization refrigerator for micro-gravity environments.

Statics and dynamics of phase segregation in multicomponent fermion gas

K. Esfarjani, S.T. Chui[1], V. Kumar[2], and Y. Kawazoe

Institute for Materials Research, Tohoku University, Sendai 980-8577, Japan

Abstract

We investigate the statics and dynamics of spatial phase segregation process of a mixture of fermion atoms in a harmonic trap using the density functional theory. The kinetic energy of the fermion gas is written in terms of the density and its gradients. Several cases have been studied by neglecting the gradient terms (the Thomas-Fermi limit) which are then compared with the Monte-Carlo results using the full gradient corrected kinetic energy. A linear instability analysis has been performed using the random-phase approximation. Near the onset of instability, the fastest unstable mode for spinodal decomposition is found to occur at a wavevector $q = 2k_F$. However, in the strong coupling limit, many more modes with $q > 2k_F$ decay with comparable time scales.

Typeset using REVTEX

I. INTRODUCTION

Recent realizations of two[3,4] and three[5] component alkali Bose-Einstein condensates (BEC's) in a trap provide us with new systems to explore the physics in otherwise unachievable parameter regimes.[6–8]. Dramatic results were recently observed in the phase segregation dynamics of mixtures of Rb[3,4] and Na[5] gases. Periodic spatial structures were found at intermediate times which then recombine at a later time.

Phase segregation phenomena have been much studied in materials science and these can be understood using *classical mechanics*. Spatial modulations have also been observed, for example, in AlNiCo alloys.[9] These were explained in terms of a concept called spinodal decomposition.[10] When a system is quenched from the homogeneous phase into a broken-symmetry phase, the ordered phase does not order instantaneously. Instead, different length scales set in as the domains form and grow with time. For the BEC's, however, *quantum mechanics* plays an important role. It has been shown[11] that it is possible to have an analogous spinodal decomposition, which manifests some of the phenomenology including a periodic spatial structure at an intermediate time that is now determined by quantum mechanics. The time scale provides for a self-consistent check of the theory and is consistent with the experimental results.[4] The growth of domains at later times is now determined by quantum tunneling and not by classical diffusion.

Recently, it became possible[12] to cool a single component system of about a million ^{40}K fermionic atoms in a magnetic trap below the Fermi temperature, T_F leading to the realization of a spin-polarized fermion gas of atoms. Similar to electrons in a solid, the dilute gas of atoms fills all the lowest energy states below the Fermi energy, E_F. The transition to this quantum degenerate state is gradual as compared to the abrupt phase transition into a Bose condensate. For single component fermionic systems, however, the equilibrium is difficult to achieve as the s-wave elastic collisions are prohibited due to Pauli exclusion principle. In the experiments of DeMarco and Jin[12], this was circumvented by using a mixture of two nuclear spin states of ^{40}K atoms for which s-wave collisions are allowed. One of the manifestations of quantum mechanics was the nature of momentum distribution which differed from the well known classical gaussian distribution. The other system which is being explored[13] is the gas of ^{6}Li atoms. From theoretical point of view, the thermodynamic properties and the density and momentum distributions of a spin-polarized Fermi gas in a harmonic trap have been studied[14–16]. Butts and Rokhsar[14] have obtained universal forms of the spatial and momentum distributions for a single component spin-polarized non-interacting fermion gas using the Thomas-Fermi (TF) approximation, whereas Schneider and Wallis[16] have studied the effects of shell closure for small number of atoms. Brunn and Burnett[15] have studied an interacting fermion gas of ^{6}Li atoms which have a large negative scattering length. Such an interaction could also lead to the possibility of superfluid state[17] in these systems. In the present paper, we consider mixtures of these new finite systems of ultracold fermionic atoms with a positive scattering length and explore the equilibrium and non-equilibrium quantum statistical physics using the TF approximation, Monte Carlo simulations, and the random phase approximation.

II. STATICS

We first start with the statics of a two component fermion gas of atoms with masses m_1 and m_2 and particle numbers N_1 and N_2. This is assumed to be confined in an azimuthally symmetric harmonic trap with radial and axial frequencies ω and $\lambda\omega$, respectively which are considered to be the same for both the components. Unlike the electron gas in matter, the fermion gas of atoms is neutral and dilute. The significant interactions between atoms are, therefore, only short-ranged and these would be responsible for any phase segregation in the system. In the long wavelength limit, the system can be well described by density functional theory and the total energy can be written as

$$E = \int [\sum_\sigma E_{0\sigma}(\rho_\sigma) + g\rho_1(\mathbf{r})\rho_2(\mathbf{r})]\mathrm{d}\mathbf{r}. \tag{1}$$

Here $E_{0\sigma} = \frac{\hbar^2}{2m_\sigma}\tau_\sigma(\mathbf{r}) + \frac{1}{2}m_\sigma\omega^2(x^2+y^2+\lambda^2z^2)\rho_\sigma(\mathbf{r})$ is the non-interacting part of the energy density and $\rho_\sigma(\mathbf{r})$ is the particle density of the component $\sigma = 1,2$ with $\int \rho_\sigma(\mathbf{r})d\mathbf{r} = N_\sigma$.

The interaction term has been approximated by contact potential $g\delta(\mathbf{r}-\mathbf{r}')$. g is related to the scattering length l by $g = 2\pi\hbar^2 l/\bar{m}$, with $\bar{m} = m_1 m_2/(m_1+m_2)$. We take l to be positive and consider here only the s-wave scattering. Therefore, the contribution to the interaction term is non-zero only when the species are different or are in different hyperfine state as in experiments. From the exclusion principle, there is no contact interaction between particles of the same species. In a more general treatment including p-wave scattering there would be additional terms involving interaction between identical species also. But these are small.

For the kinetic energy density τ_σ we use a local approximation including the first and second derivatives of the charge density,

$$\tau_\sigma(\mathbf{r}) = \frac{3}{5}(6\pi^2)^{2/3}\rho_\sigma(\mathbf{r})^{5/3} + \frac{1}{36}\frac{|\nabla\rho_\sigma(\mathbf{r})|^2}{\rho_\sigma(\mathbf{r})} + \frac{1}{3}\nabla^2\rho_\sigma(\mathbf{r}). \tag{2}$$

The first term represents the TF approximation to the kinetic energy. The second term is $\frac{1}{9}|\nabla\sqrt{\rho_\sigma}\,|^2$ and represents the gradient correction to the kinetic energy. The integral of the third term extended to infinity vanishes, and will be neglected.

Without the interaction term in (1), the system behaves in the same fashion as the one component system in which case Butts and Rokhsar[14] obtained E_F to be related to the total particle number N by $E_F = \hbar\omega(6\lambda N)^{1/3}$ and the density profile at T=0 is given by

$$\rho_{\mathrm{non-interacting}}(\mathbf{r}) = \rho_0\left[1-\bar{r}^2/R_F^2\right]^{3/2}, \tag{3}$$

with $\bar{r}^2 = x^2+y^2+\lambda^2 z^2$, $\rho_0 = 8N\lambda/\pi^2 R_F^3$, and $R_F = (2E_F/m\omega^2)^{1/2}$. The latter gives the characteristic size of the gas. In the TF approximation, the trapping potential can be treated to be locally constant and we can define a local Fermi wavevector, $k_F(\mathbf{r})$, and the density at $\mathrm{T} = 0$ can be written as $\rho_{non-interacting}(\mathbf{r}) = k_F^3(\mathbf{r})/6\pi^2$. Also we can define a characteristic Fermi wavevector $K_F = (2mE_F/\hbar^2)^{1/2}$ corresponding to a free particle with energy E_F. We now examine the properties of the mixed (two-component) system in the presence of interactions. The strength of the coupling, which controls the phase segregation, depends on the dimensionless parameter which is the ratio between the interaction and the kinetic energies, namely $g\rho_1\rho_2/[\frac{3\hbar^2}{10}(6\pi^2)^{2/3}(\rho_1^{5/3}/m_1+\rho_2^{5/3}/m_2)] \propto l k_{F1}^3 k_{F2}^3(m_1+m_2)/(m_2 k_{F1}^5 + m_1 k_{F2}^5)$. In the simple case of equal masses ($m_1 = m_2 = m$) and densities ($\rho_1 = \rho_2 = \rho$) of the two components, this simply becomes $\propto lk_F$. This means that the coupling would be stronger if l and the density are large. Also as E_F is proportional to the frequency of the trap (a higher frequency leads to larger separation between the levels), the coupling would be large for higher frequencies.

For a general two-component system with chemical potentials μ_1 and μ_2 the ground state is obtained by minimizing the new thermodynamic potential $\Omega = E \Leftrightarrow \int(\mu_1\rho_1 + \mu_2\rho_2)\mathrm{d}\mathbf{r}$. This leads to the following system of equations:

$$\frac{\partial\Omega}{\partial\rho_1(\mathbf{r})} = \frac{\hbar^2}{2m_1}\left[(6\pi^2\rho_1)^{\frac{2}{3}} \Leftrightarrow \frac{1}{36}\left(\left|\frac{\nabla\rho_1}{\rho_1}\right|^2 + 2\frac{\nabla^2\rho_1}{\rho_1}\right)\right] + \left(\frac{1}{2}m_1\omega^2\bar{r}^2 \Leftrightarrow \mu_1 + g\rho_2\right) = 0 \qquad (4)$$

$$\frac{\partial\Omega}{\partial\rho_2(\mathbf{r})} = \frac{\hbar^2}{2m_2}\left[(6\pi^2\rho_2)^{\frac{2}{3}} \Leftrightarrow \frac{1}{36}\left(\left|\frac{\nabla\rho_2}{\rho_2}\right|^2 + 2\frac{\nabla^2\rho_2}{\rho_2}\right)\right] + \left(\frac{1}{2}m_2\omega^2\bar{r}^2 \Leftrightarrow \mu_2 + g\rho_1\right) = 0. \qquad (5)$$

Similar to the one-component case, one can rewrite the above in a dimensionless form by introducing for each of the species σ, the following quantities: $R_\sigma = [2\mu_\sigma/m_\sigma\omega^2]^{\frac{1}{2}}$, $k_{F\sigma}(\mathbf{r}) = (6\pi^2\rho_{\sigma 0}(\mathbf{r}))^{\frac{1}{3}}$, $K_{F\sigma} = (2m_\sigma\mu_\sigma/\hbar^2)^{\frac{1}{2}}$, $\mathcal{G}_\sigma = g\rho_{\bar{\sigma}0}/\mu_\sigma$, $S_\sigma = k_{F\sigma}/K_{F\sigma}$ and $n_\sigma(\mathbf{r}) = \rho_\sigma(\mathbf{r})/\rho_{\sigma 0}$. Here $\rho_{\sigma 0}(\mathbf{r})$ is the density of the component σ in the absence of interaction and $\bar{\sigma} = 3$-σ. If one neglects the smaller terms containing derivatives of ρ (the TF limit), one obtains the following algebraic equations satisfied by the dimensionless densities n_1 and n_2 for any coupling strength $\mathcal{G}_\sigma$:

$$\begin{aligned} S_1^2 n_1^{2/3} &= 1 \Leftrightarrow \bar{r}^2/R_1^2 \Leftrightarrow \mathcal{G}_1 n_2 \\ S_2^2 n_2^{2/3} &= 1 \Leftrightarrow \bar{r}^2/R_2^2 \Leftrightarrow \mathcal{G}_2 n_1. \end{aligned} \qquad (6)$$

We see that the effect of the additional $\mathcal{G}_\sigma n_{\bar{\sigma}}$ term is to deplete the regions where $n_{\bar{\sigma}}$ is highest (without necessarily leading to a phase segregation).

When there is phase segregation, the interface energy is proportional to the square root of the coefficient of the gradient term[19] and it often serves to distinguish different configurations. In that case, their effect cannot be neglected and these are included in the Monte Carlo simulations. We next discuss some special cases for the TF limit.

A. TF limit: Similar densities: ($\mu_1 = \mu_2$) for any coupling

To simplify the notations, we will use: $\mu_1 = \mu_2 = \mu$; $R_1 = R_2 = R$; $\mathcal{G}_1 = \mathcal{G}_2 = \mathcal{G}$. In this case, three solutions to Eq. (6) will correspond to $n_1 = n_2$, of which only one is physical with $n_1 > 0$. If a solution $n_2 = f(n_1)$ exists, by symmetry, another one is necessarily $n_1 = f(n_2)$. These solutions with $n_1 \neq n_2$ can be obtained numerically. The real solutions are plotted in Fig. 1, where the physical $n_1 = n_2$ solution is referred to as "Sym", and the other conjugate (asymmetric) solutions are referred to as "A$_1$" and "A$_2$". Below we discuss these solutions in the weak and strong coupling limits.

1. Weak or intermediate coupling regime

In this case we look for symmetric solutions ($n_1 = n_2 = n$, $S_1 = S_2$). Equation (6) then reduces to (dropping the subscripts):

$$S^2 n(\mathbf{r})^{2/3} = 1 - \bar{r}^2/R^2 - \mathcal{G}\, n(\mathbf{r}), \tag{7}$$

which can be solved easily numerically to give the charge profile of the non-segregated phase. It is possible to show that after proper rescaling, the result for all coupling strengths and at any point can be summarized in a single curve displayed with solid line in Fig. 1. If $n_{\mathcal{G}}(\mathbf{r})$ is a solution for Eq. (7), then $\mathcal{N} = n\,\mathcal{G}^3$ versus $\mathcal{P} = [1 - \bar{r}^2/R^2]\,\mathcal{G}^2$ is the universal function of Fig. 1 satisfying $S^2\mathcal{N}^{2/3} + \mathcal{N} - \mathcal{P} = 0$. For small couplings and near the boundary ($\mathcal{P} \approx 0$; $\mathcal{N}^{2/3} \gg \mathcal{N} \; - \; \mathcal{N} = S^{-3}\mathcal{P}^{3/2}$), this curve is a power law and in fact tends to the non-interacting density $n(\mathbf{r}) \approx [1 - (x^2 + y^2 + \lambda^2 z^2)/R^2]^{3/2}$. For larger couplings, and near the center where $\mathcal{P}$ is the largest, $\mathcal{N}^{2/3} \ll \mathcal{N} \Rightarrow \mathcal{N} \approx \mathcal{P}$. The density can then be approximated with $n(\mathbf{r}) \approx [1 - \bar{r}^2/R^2]/\mathcal{G}$.

2. Strong coupling regime

The above situation, however, can not be always sustained. In the strong coupling limit, we can have phase segregation ($n_1 \neq n_2$), and one needs to go back to Eq. (6) which now admits lower energy solutions that are not "permutation symmetric":

$$S_1^2 n_1^{2/3} + \mathcal{G} n_2 = 1 \Leftrightarrow (x^2 + y^2 + \lambda^2 z^2)/R^2 \Leftrightarrow S_1^2 \mathcal{N}_1^{2/3} + \mathcal{N}_2 = \mathcal{P} \Leftrightarrow S_1^6 \mathcal{N}_1^2 = (\mathcal{P} \Leftrightarrow \mathcal{N}_2)^3$$
$$S_2^2 n_2^{2/3} + \mathcal{G} n_1 = 1 \Leftrightarrow (x^2 + y^2 + \lambda^2 z^2)/R^2 \Leftrightarrow S_2^2 \mathcal{N}_2^{2/3} + \mathcal{N}_1 = \mathcal{P} \Leftrightarrow S_2^6 \mathcal{N}_2^2 = (\mathcal{P} \Leftrightarrow \mathcal{N}_1)^3, \quad (8)$$

where we used the same simplifying notations as before. As previously mentioned, the symmetric solution $\mathcal{N}_1 = \mathcal{N}_2$ always exists. This can be exploited to reduce the above equations to a quadratic equation, which is analytically more transparant.

Subtracting the above equations from each other and dividing out by $\mathcal{N}_1 \Leftrightarrow \mathcal{N}_2$, we obtain at the point $S_1 = S_2$,

$$S_1^3 \mathcal{N}_1 + S_2^3 \mathcal{N}_2 = (\mathcal{P} \Leftrightarrow \mathcal{N}_2)^2 + (\mathcal{P} \Leftrightarrow \mathcal{N}_1)^2 + (\mathcal{P} \Leftrightarrow \mathcal{N}_2)(\mathcal{P} \Leftrightarrow \mathcal{N}_1). \quad (9)$$

This quadratic equation can be solved for $\mathcal{N}_1$ in terms of $\mathcal{N}_2$.

The solutions will all be axially symmetric in that they are functions of $\bar{r}^2$ only. In actuality, the axial symmetry can also be broken, but we do not find it here since we neglected the terms in gradient of the charge density in the kinetic energy. The broken symmetry solutions will be discussed in the results from the Monte Carlo simulations where these terms were kept. In Fig. 1, the solutions with $n_1 \neq n_2$ can be seen in the limit of small reduced distance and large $\mathcal{P}$. The bifurcation point where these solutions start to occur corresponds to $\mathcal{P}_c \approx 0.74$, and $\mathcal{N}_c \approx 0.3$. Since $\mathcal{G}^2 = \mathcal{P}/(1 \Leftrightarrow \bar{r}^2/R^2) \geq \mathcal{P}$, the critical coupling for the unequal solution to occur is $\mathcal{G}_c = \sqrt{\mathcal{P}_c}$. Since $\mathcal{G} = S^2(k_F l)4/3\pi$, we find a critical dimensionless coupling $(k_F l)_c \approx 2.03$. We shall come back and compare this value with that obtained with a different approach.

FIGURES

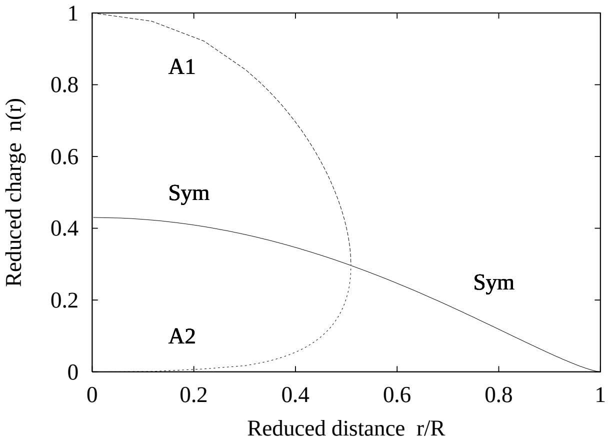
1
0.8
0.6
0.4
0.2
0
0
0.2
0.4
0.6
0.8
1
Reduced charge n(r)
Reduced distance r/R
A1
Sym
Sym
A2

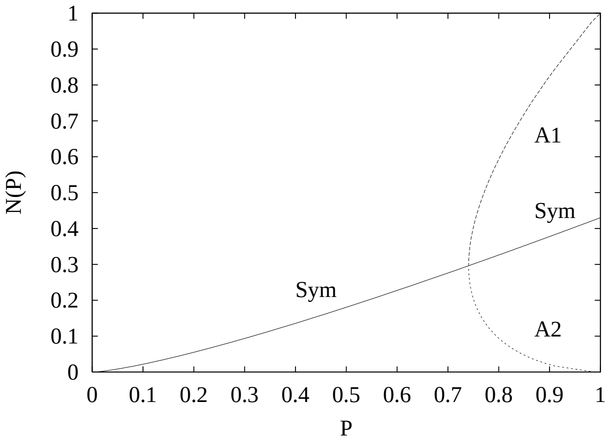
1
0.9
0.8
0.7
0.6
0.5
0.4
0.3
0.2
0.1
0
0
0.1
0.2
0.3
0.4
0.5
0.6
0.7
0.8
0.9
1
N(P)
P
A1
Sym
Sym
A2

FIG. 1. Top: Dimensionless charge versus dimensionless radius $\bar{r}/R$ for $\mathcal{G} = 1$ in the case of $S_1 = S_2 = 1$. For $\bar{r}/R$ larger than 0.51 both asymmetric solutions join the symmetric density profile. The sharp features around this point are due to the neglect of the gradient terms. Bottom: Universal curve of rescaled charge $\mathcal{N} = n\,\mathcal{G}^3$ versus $\mathcal{P} = (1-\bar{r}^2/R^2)\,\mathcal{G}^2$ which is valid for all coupling strengths. Note that $0 < \mathcal{P} < 1$, and $\mathcal{N}_{\max} = 0.43$. The strong coupling regime is separated from the weak coupling regime by the line $\mathcal{P} = 0.741$. In both figures, the symmetric solution is drawn with solid line, and the asymmetric one with dashed lines.

B. TF limit: Very different densities: ($\mu_1 \gg \mu_2$) for any coupling

One can also treat the case where one of the species is a minority ($\mu_1 \gg \mu_2$). If we assume $\mu_1 = \lambda^2\mu_2$, then $R_1 = \lambda R_2$; $K_{F1} = \lambda K_{F2}$;, and $n_\sigma \sim 1$. The charge distribution of the majority species will be weakly perturbed. Referring to Eqs. (6), one can see that the coupling $\mathcal{G}_1 = g\rho_{20}/\mu_1$ becomes very small and maybe neglected. Thus a good approximation is to assume $\rho_1 \approx \rho_{\mathrm{non-interacting}}$. The $\mathcal{G}_2$ term in the second equation, however, is a large quantity, and will strongly affect the charge density n_2. Therefore,

$$n_2(\mathbf{r}) = S_2^{-3}\left[1 \Leftrightarrow \bar{r}^2/R_2^2 \Leftrightarrow \mathcal{G}_2 S_1^{-3}[1 \Leftrightarrow \bar{r}^2/R_1^2]^{\frac{3}{2}}\right]^{\frac{3}{2}} . \tag{10}$$

In the presence of the majority species, the number of atoms of minority species will be much less than their non-interacting counterparts which would have the same chemical potential. As we can see from the above equation, their number, even at the origin is reduced by a factor of $(1 \Leftrightarrow \mathcal{G}_2 S_1^{-3})^{\frac{3}{2}}$. We find that for a large enough $\mathcal{G}_2$ the charge $\mathcal{N}_2$ is depleted from the center (see also Fig. 1b) More importantly, their general profile is not affected much, though the radius is also much smaller than R_1.

C. TF limit: linear instability analysis

We next study the fluctuations of the system about its equilibrium configuration in the TF limit by expanding the thermodynamic potential Ω upto second order in the charge density variation $\delta\rho$ about its minimum which was computed above. The sign of the second derivative of Ω will decide the stability of the symmetric phase. A phase segregation occurs when the second derivative ceases to be positive definite. If the transition is first order, it would have already occurred before reaching a negative second derivative. For simplicity, we consider the symmetric phase which was just solved. In this case, the second derivative from Eqs. (3-4) is just a 2×2 matrix:

$$\frac{\partial^2 \Omega}{\partial \rho_\sigma \partial \rho_{\sigma'}} = \frac{\hbar^2}{2m_\sigma}\frac{2}{3}(6\pi^2)^{\frac{2}{3}}\, \rho_\sigma^{-\frac{1}{3}}\, \delta_{\sigma\sigma'} + g\,(1 - \delta_{\sigma\sigma'}). \tag{11}$$

The phase instability criterion in the symmetric phase thus becomes

$$\omega_- = \frac{\hbar^2}{2\sqrt{m_1 m_2}}\frac{2}{3}(6\pi^2)^{\frac{2}{3}}\, \rho_\sigma^{-\frac{1}{3}} - g = 0 \tag{12}$$

Thus the instability will first occur locally at the point where the relation $\mathcal{N}^{1/3} = \mathcal{G}n^{\frac{1}{3}} = 2/3\, S_1 S_2$ is satisfied. At the origin where $S_1 = S_2 = 1$, this implies that $\mathcal{N} = 0.296$. This is within numerical accuracy to the critical $\mathcal{N}_c$ obtained earlier.

D. General case: Monte Carlo results

The density distribution that extremized the energy functional in Eq. (1) can be obtained by a Monte Carlo simulation with a weighting factor $exp(-E/T)$ for a parameter T that is sufficiently low. This is basically the simulated annealing method and has been exploited successfully in earlier treatment[8] of the corresponding Bose system described by a Gross-Pitaevski functional.

We approximate the volume integral of the energy functional by a discrete sum. Using the scaled radius $\bar{r}$, we sample a lattice inside a sphere of diameter $2R$ consisting of 40 sites along the diameter, making a total of 33398 sites. The derivative term is approximated by a finite difference. For simplicity, we show here results for the case when the two components have the same mass.

We first show in Fig. 2 the density profile of component 2 as a function of x and y for z=0 for the weak coupling case with no phase segregation. The values of different parameters were chosen to be $\omega = 600Hz$, $l = 52\,a_{\mathrm{Bohr}}$, $\lambda = \sqrt{8}$, and $N_1 = N_2 = 10^6$ ($\mu_1 = \mu_2 = 1.626 \times 10^{-29}$); roughly corresponding to the experimental parameters of the ^{40}K system.[12] The density profile for component 1 is the same and hence is not shown.

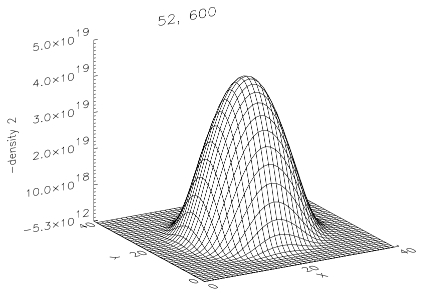

FIG. 2. Snap shot of the density profile at z=0 as a function of x and y in the weak coupling limit.

In the limit of strong interaction, phase segregation starts and as mentioned earlier, the system can now also break cylindrical symmetry. This happens when $k_F l$ is large enough, which in turn can be achieved with only large k_F, only large l, or both. To illustrate this, we show in Fig. 3 the density profiles for components 1 and 2 for the case of only large l with $l = 20800 a_B$, $\mu_1 = \mu_2 = 1.626 \times 10^{-29}$, and $\omega = 300Hz$.

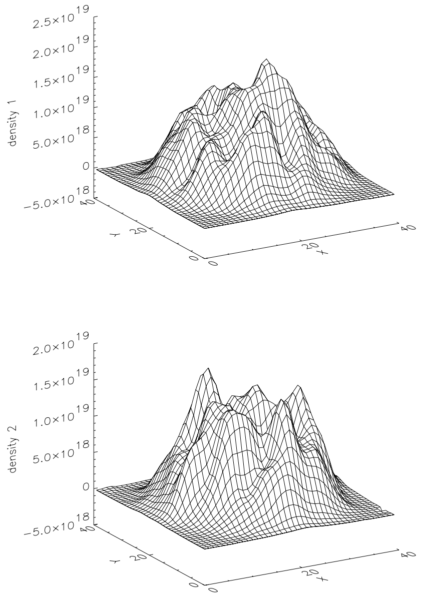

FIG. 3. Snap shot of the density profile of components 1 (top) and 2 (bottom) at z=0 as a function of x and y in the strong coupling limit.

For the case of both large k_F and l, we show in Fig. 4 the density profiles for $l = 2080a_B$, $\mu_1 = \mu_2 = 1.626 \times 10^{-29}$, and $\omega = 6000Hz$. The difference in the densities of the two components shows that the largest change occurs near the center where the density is the maximum.

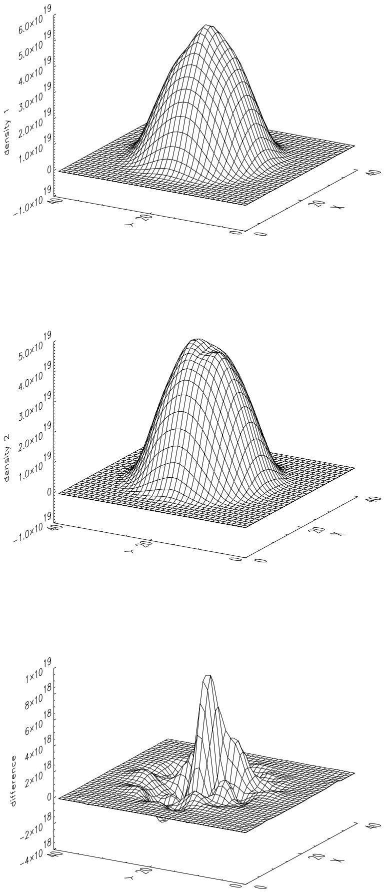

FIG. 4. Snap shot of the density profile of components 1 and 2 and their difference at z=0 as a function of x and y in the strong coupling limit.

It is to be further noted that for this case, the density distribution is still quite cylindrical but there is a slight asymmetry, as we can see from the graph of the difference. This asymmetry become more pronounced as the interaction is increased further. In Fig. 5 we have shown the results of simulations with larger l. The density profiles were calculated for $l = 4160a_B$, $\mu_1 = \mu_2 = 1.626 \times 10^{-29}$, $\omega = 6000Hz$.

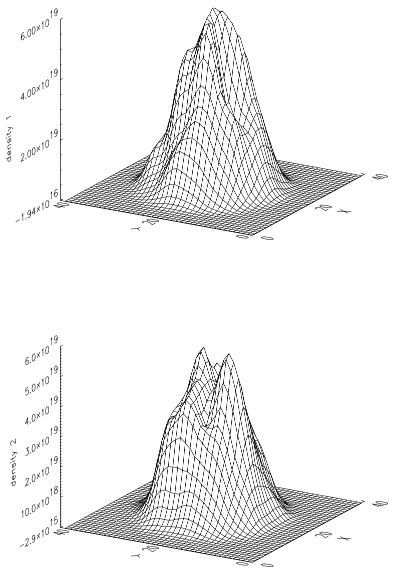

FIG. 5. Snap shot of the density profiles of components 1 and 2 at z=0 as a function of x and y in the strong coupling limit.

As discussed earlier, phase separation can also occur when $N_1 >> N_2$. As an illustration, we show in Fig. 6 the density profiles for components 1 and 2 for the case $l = 104a_B$, $\mu_1 = 2.6016 \times 10^{-26}$, $\mu_2 = 4.336 \times 10^{-26}$ and $\omega = 1600000$.

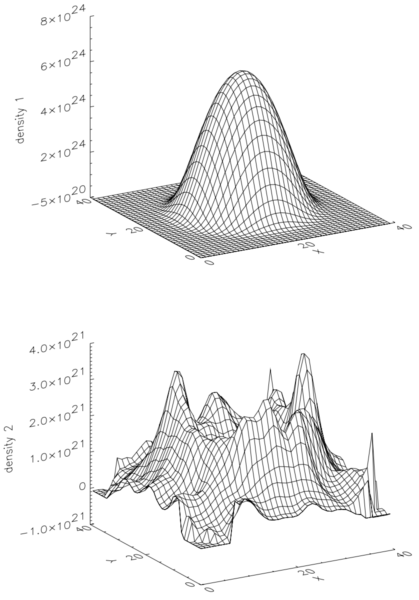

FIG. 6. Snap shots of the density profiles at z=0 as a function of x and y for $N_1 >> N_2$.

The density of component 2 is small, thus its noise is also substantially higher.

III. DYNAMICS

We next turn our attention to the issue of dynamics. For the classical and boson spinodal decomposition, the fastest unstable mode occurs at a finite wave vector. We ask if a similar situation occurs for the fermion case. We found that the fastest unstable mode occurs at wavevector $q = 2k_F$ at the onset of instability. For stronger coupling, many modes with $q > 2k_F$ decay with comparable time scales. We now describe the details of this linear stability analysis.

The energy functional (Eq. (1)) which was approximated with a *local kinetic energy* depending on the density and its derivatives is only good in the long wavelength limit. Due to this approximation, we found that the instability has a local character and occurs first in regions of high density. Here we will perform a linear instability analysis in the random phase approximation (RPA) to improve upon this local picture. The linear susceptibility χ is defined as the response of the charge density to an external potential V which could also be σ-dependent:

$$\delta\rho_\sigma(\mathbf{r}) = \sum_{\sigma'=1,2} \int d\mathbf{r}' \chi_{\sigma\sigma'}(\mathbf{r},\mathbf{r}') V^{tot}_{\sigma'}(\mathbf{r}'). \tag{13}$$

Here V^{tot} is the total self-consistent field and is the sum of the external field and that due to the interaction: $V^{\rm tot}_\sigma = V_\sigma + g\delta\rho_{\bar{\sigma}}$. The bare response $\chi_{\sigma\sigma}$ can be obtained from the usual Lindhard expression[20]. Since there is no term in the Hamiltonian that interchanges the species 1 and 2, off-diagonal terms of the susceptibility are zero ($\chi_{12} = \chi_{21} = 0$). Taking the above into consideration, Eq. (13) can be written in the following matrix form: $\delta\rho = \chi(V + G\delta\rho)$, leading to $\delta\rho = [1 \Leftrightarrow \chi G]^{-1}\chi V$, where the 2×2 matrix G has 0 as its diagonal elements and g as its off-diagonal elements, and χ is diagonal. Consequently, an instability will occur when the following determinant becomes zero:

$$\mathrm{Det}|1 \Leftrightarrow \chi G| = \mathrm{Det}|1 \Leftrightarrow g^2\chi_{11}\chi_{22}| = 0. \tag{14}$$

In the case where the densities are equal, $\chi_{11} = \chi_{22} \equiv \chi$, the two eigenmodes are calculated as:

$$\delta\rho_1 + \delta\rho_2 = (1 - \chi g)^{-1}\chi(V_1 + V_2) \tag{15}$$

$$\delta\rho_1 - \delta\rho_2 = (1 + \chi g)^{-1}\chi(V_1 - V_2). \tag{16}$$

The first mode corresponds to a density fluctuation, and the second mode $\delta\rho_1 - \delta\rho_2$ represents the phase separation instability in which we are interested. The response corresponding to this mode is given by $\epsilon(q,w) = [1 + g\chi(q,w]^{-1}$. The instability decay time ν^{-1} is determined from the formula $\epsilon^{-1}(q, i\nu) = 0$. There exists a $q = q_0$ such that $\nu(q_0)$ is largest. This determines the spinodal wavevector in the fermion system. To treat this problem, we use the semi-classical approximation and take k_F in an inhomogeneous system to be a local function of the position: $k_F(\mathbf{r}) = [6\pi^2\rho(\mathbf{r})]^{1/3}$. From the Lindhard expression[20] for χ for real frequencies, we obtain, after correcting for a spin degeneracy factor of 2, the corresponding dimensionless response $\bar{\chi} = 4\pi^2\hbar^2\chi(q,is)/mk_F$ for imaginary frequencies:

$$\bar{\chi}(q,is) = -1 + (1 + (s/q)^2 + q^2/4)\log[\frac{(1-q/2)^2 + s^2/q^2}{(1+q/2)^2 + s^2/q^2}]/2q \tag{17}$$

$$+s\left(\tan^{-1}[s/(q(1-q/2))] + \tan^{-1}[s/(q(1+q/2))]\right)/q.$$

Here q is in units of k_F and s, in units of $\hbar/2E_F$. The two dimensional plot of $\bar{\chi}$ as a function of q and s is shown in Fig. 7.

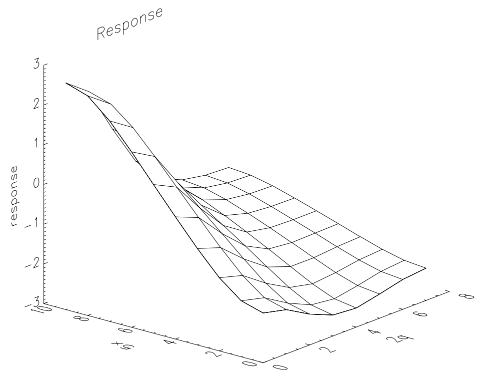

FIG. 7. Plot of the Lindhard susceptibility as a function of q for several values of the imaginary frequency.

Now $g\chi = k_F l \bar{\chi}/\pi$. The instability condition thus implies $c\bar{\chi} = 1$ where $c = k_F l/\pi$. From this plot, we arrive at the conclusion that for small g there is no solution to $\epsilon^{-1}(q, i\nu) = 0$ and no instability develops.

The algebraic equation $c\bar{\chi}(q, i\nu) = 1$ is solved with a bisection algorithm. The inverse decay time ν as a function of the wavevector in units of k_F is shown in Fig. 8. As can be seen, the fastest unstable mode occurs at wavevector $q = 2k_F$ at the onset of the instability ($c \approx 0.3$). For stronger coupling, many modes with $q > 2k_F$ decay with comparable time scales.

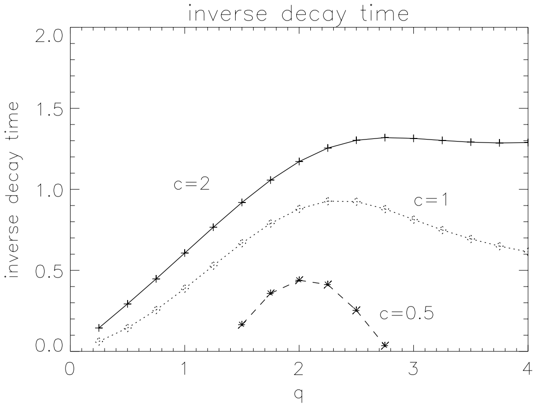

FIG. 8. The inverse decay time for phase segregation mode of wave vector q for three values of the dimensionless coupling $c = k_F l/\pi$.

The $2k_F$ instability occurs at a critical dimensionless coupling $(k_F l)_C \approx 0.3\pi$. This is about two times smaller than the instability derived in the previous section, which focused mostly on the long wavelength aspect of the problem. We think the difference is real, and suggests a physical picture where the $2k_F$ instability occurs first, with more phase segregation happening as the coupling is further increased.

Further phase separation creates a bigger increase in the kintic energy of the system, which cannot be compensated for by the interaction term. In the really strong interaction limit, further phase separation can take place either via tunnelling[21,22] or via quantum motion of the domain walls. We hope to investigate this further in the future.

IV. CONCLUSION

In conclusion we have investigated the statics and dynamics of the spatial phase segregation process of a mixture of fermion atoms in a harmonic trap using the density functional theory and the random phase approximation. As the coupling starts to increase, even with the same chemical potential, equilibrium distribution with unequal densities starts to appear, which quite often do not exhibit axially symmetric correleations.

Similar to the classical and Bose spinodal decomposition case, the fastest mode for the initial phase segregation occurs at a finite wave-vector. However, different from these other cases, near the onset of instability with intermediate coupling, the phase separation stops after the initial phase separation at the wavevector $2k_F$. Further phase separation creates a bigger increase in the kintic energy of the system, which cannot be compensated for by the interaction term.

The instability calculation for the phase segragation phenomena discussed here is related to the instability calculation for the antiferromagnetic transition of the electron gas. In the electron gas, this is enhanced when there is nesting of Fermi surface such as in Cr or in one dimensional materials. The transition always stops after the $2k_F$ instability and no further "segregation" takes place.

An interesting situation is the one dimensional trap as it would exhibit a much stronger instability. In mean field, the one dimensional density difference response function $\epsilon(2k_F) = 1/[1 + lk_F ln(T/E_F)]$ is logarithmically infinite at zero temperature. The transition temperature occurs at $T_c = E_F e^{-1/k_F l}$. One dimensional trap has been extensively studied[5] and we expect a higher tendency towards phase segragation in that case as well.

ACKNOWLEDGMENTS

S.T. Chui is partly supported by NASA under contract no. NAG8-1427 He and VK thank the Institute for Materials Research for the kind hospitality, where the main body of this

work was completed.

REFERENCES

[1] Permanent address: Bartol Research Institute, University of Delaware, Newark, DE 19716, USA.

[2] Permanent address: Dr. Vijay Kumar Foundation, 45 Bazaar Street, K.K. Nagar (West), Chennai - 600 078, India.

[3] C.J. Myatt, E.A. Burt, R.W. Ghrist, E.A. Cornell, and C.E. Wieman, Phys. Rev. Lett. **78**, 586 (1997).

[4] D.S. Hall, M.R. Matthews, J.R. Ensher, C.E. Wieman, and E.A. Cornell, Phys. Rev. Lett. **81**, 1539 (1998).

[5] J. Stenger, S. Inouye, D.M. Stamper-Kurn, H.-J. Miesner, A.P. Chikkatur, and W. Ketterle, Nature **396**, 345 (1998).

[6] C.K. Law, H. Pu, N.P. Bigelow, and J.H. Eberly, Phys. Rev. Lett. **79**, 3105 (1997); and references therein.

[7] T.L. Ho, Phys. Rev. Lett. **81**, 742 (1998).

[8] S.T. Chui and P. Ao, Phys. Rev. A**59**, 1473 (1999).

[9] Y. Iwama and M. Takeuchi, Trans. Jap. Inst. Met. **15**, 371 (1974); ibid. **17**, 481 (1976).

[10] J.W. Cahn, Tans. Met. Soc. AIME **242**, 166 (1968);

J.S. Langer, in *Solids Far From Equilibrium*, ed. C. Godrèche (Cambridge University Press, Cambridge, 1992).

[11] P. Ao and S. T. Chui, To appear in J. Phys. Conds. Matt. and Physica.

[12] B. DeMarco and D.S. Jin, Science **285**, 1703 (1999).

[13] K.M.O'Hara, S.R. Granade, M.E. Gehm, T.A. Savard, S. Bali, C. Freed, and J.E. Thomas,

Phys. Rev. Lett. **82**, 4204 (1999).

[14] D. A. Butts and D. S. Rokhsar, Phys. Rev. A**55**, 4346 (1997).

[15] G.M. Brunn and K. Bernett, Phys. Rev. A**58**, 2427 (1998).

[16] J. Schneider and H. Wallis, Phys. Rev. A**57**, 1253 (1998).

[17] M. Houbiers, R. Ferwerda, H.T.C. Stoof, W.I. McAlexander, C.A. Sackett, and R.G. Hulet, Phys. Rev. A**56**, 4864 (1997).

[18] O. Penrose, Phil. Mag. **42**, 1373 (1951);

E.P. Gross, Nuovo Cimento **20**, 454 (1961);

L.P. Pitaevskii, Sov. Phys. JETP **13**, 451 (1961);

E. Demircan, P. Ao, and Q. Niu, Phys. Rev. B**54**, 10027 (1996).

[19] P. Ao and S.T. Chui, Phys. Rev. A**58**, 4836 (1998).

[20] A. Fetter and D. Walecka, *Quantum Many-Body Systems*, Mc Graw Hill (1991).

[21] I. Zapata, F. Sols, and A.J. Leggett, Phys. Rev. A**57**, R28 (1998).

[22] A. Smerzi, S. Fantoni, S. Giovanazzi, and S.R. Shenoy, Phys. Rev. Lett. **79**, 4950 (1997).

Numerical Studies of Confined Helium and Helium Films

Efstratios Manousakis,
Florida State University

We have used state of the art simulation techniques to study the finite-size scaling behavior of thermal resistivity near the lambda point of helium confined in pore-like geometry similar to the experiment BEST. We also present our results for the phase diagram of helium deposited on the ideal graphite substrate and on graphite pre-plated with hydrogen. Our results for a few layers are in remarkable agreement with the experiment. In addition, to the phase diagram, our studies will give us insight on the role of the surface Van der Waals forces in scaling of confined helium.

Thermal Dissipation in ^{4}He Below but Near the Lambda Line

Kerry Kuehn and Guenter Ahlers

Department of Physics and iQUEST,

University of California, Santa Barbara, CA 93106, USA

(October 9, 2000)

Abstract

We present high-resolution experimental results for the thermal resistivity R due to mutual friction below but near the superfluid transition temperature $T_\lambda(P)$ of ^{4}He. The measurements were made along several isobars between saturated vapor pressure and the melting curve. They cover the heat-current-density range $0.1 < q < 70 \mu\mathrm{W/cm}^2$ and the reduced-temperature range $3 \times 10^{-7} < t \equiv 1 - T/T_\lambda(P) < 3 \times 10^{-5}$ ($T_\lambda(P)$ is the transition temperature at pressure P for $q = 0$). We find that R has an incipient divergence at $T_\lambda(P)$ which can be described by the powerlaw $R = (t/t_0)^{m\nu+\alpha}$ where $t_0 = (q/q_0)^x$; but this divergence is supplanted by a transition to a highly dissipative phase at a critical temperature $T_c(q,P) < T_\lambda(q,P)$ described by $t_c(q,P) \equiv 1 - T_c(q,P)/T_\lambda(P) = (q/\Delta_0)^y$.

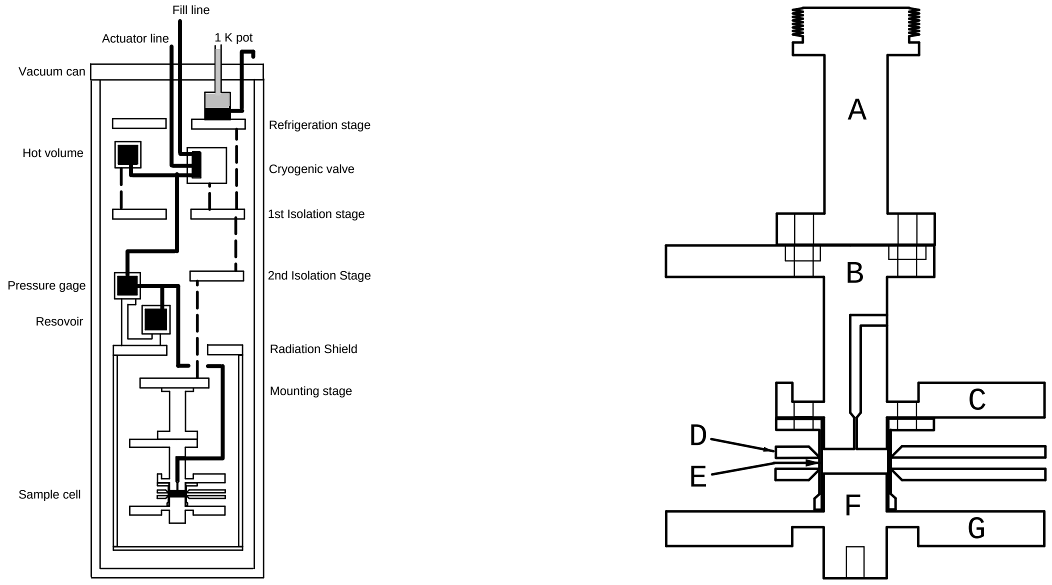
Fill line
Actuator line
1 K pot
Vacuum can
Refrigeration stage
Hot volume
Cryogenic valve
1st Isolation stage
Pressure gage
2nd Isolation Stage
Resovoir
Radiation Shield
Mounting stage
Sample cell
A
B
C
D
E
F
G

FIG. 1. Left: A schematic drawing of the cryostat. Right: the sample cell. Shown are the mounting post (A), cell top (B), wings (C) and (G) and sideplanes (D) for mounting thermometry, stainless steel sidewall (E) and cell bottom (F).

I. INTRODUCTION

At finite heat-current densities q superfluid ^{4}He has a thermal resistivity $R(t)$ due to the interaction between the normalfluid and the superfluid known as "mutual friction". [1] For bulk helium and at saturated vapor pressure (SVP) recent high-resolution measurements suggest a divergence of $R(t, P)$ at $t \equiv 1 - T/T_\lambda(P) = 0$, where $T_\lambda(P)$ is the superfluid transiton temperature at a pressure P in the limit as q vanishes. [2] However, upon approaching T_λ, there was a sudden dramatic increase of R at $T_c(q, P) < T_\lambda(P)$ where R was still finite.

In the present paper we present results which extend the previous measurements at SVP to several isobars, covering the pressure range $SVP \leq P \lesssim 29$bar. In addition to determining $R(t, P)$, our measurements also yielded $T_c(q, P)$.

Measurements of R were made before at various pressures by Brewer and Edwards. [3] These authors used much larger heat currents, and worked well below the superfluid transition. They observed that R increases with pressure. We also find that R increases with pressure. In our current and temperature range the dependence on P, t, and q

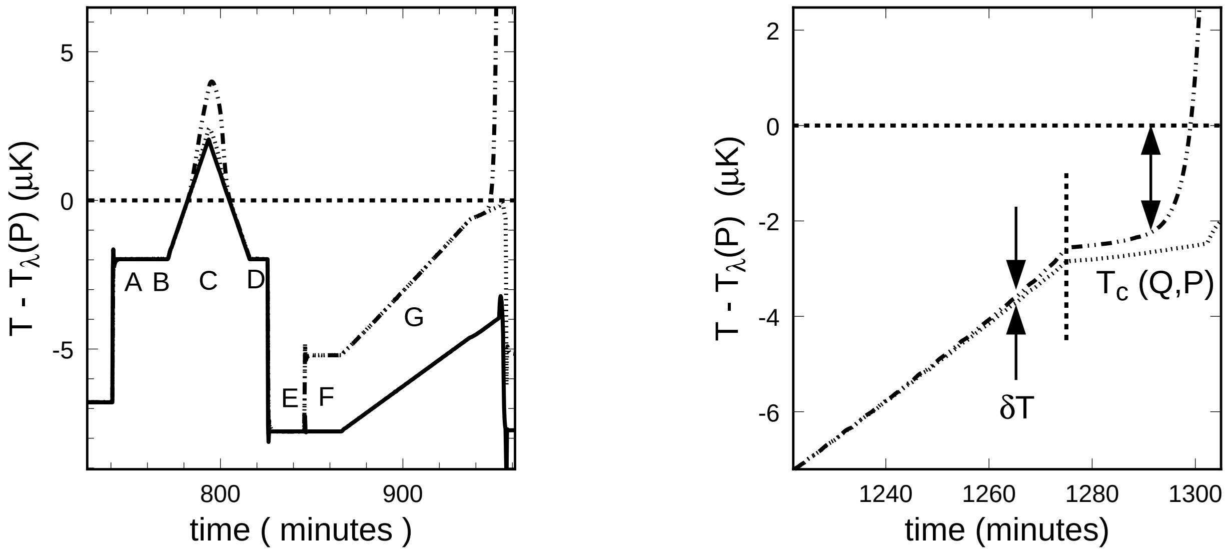

FIG. 2. Typical experimental runs. Horizontal dashed lines represent $T_\lambda(P)$. Solid, dotted, and dash-dotted lines represent the temperatures of the cell top, cell side top, and cell side bottom thermometers respectively. Left: A complete low-q run (see text). Right: Expanded view of a high-q run. δT is the small temperature difference between the sideplanes due to mutual friction. The vertical dashed line represents the time at which the cell bottom reached $T_c(q,P)$.

can be described by the power law $R = (t/t_0)^{-(m\nu+\alpha)}$ with $t_0 = (q/q_0)^x$. Here, ν is the correlation-length exponent, and m and α are exponents appearing in the Gorter-Mellink mutual friction model described below. For $T_c(q,P)$, we find that $t_c(q,P) = (q/\Delta_0)^y$ where $t_c(q,P) \equiv 1 - T_c(q,P)/T_\lambda(P)$.

II. EXPERIMENTAL PROCEDURE

An experimental run consisted of applying a constant heat current to the cell bottom while ramping the temperature upwards through the transition. An example of this procedure is shown in the left part of Fig. 2. At each q and P, the cell-top temperature was regulated a couple of micro Kelvin below the transition (A). Next, $q = 15$ nW/cm^2 was applied to the cell from the bottom (B). Several minutes were allowed for a steady-state temperature-profile to develop. The cell-top temperature was then ramped at a constant rate of 3 nK/second up and then down again through the transition (C). The heat current was then turned off (D). This yielded $T_\lambda(P)$, i.e. the transition temperature in the limit of very low q.

The cell-top temperature was then reduced to several μK below the transition (E). After equilibration, a larger q, in this case 2.37 μW/cm^2, was applied to the cell bottom.The fluid was again allowed to reach its steady-state temperature (F). The cell-top temperature was then ramped at a rate of 0.7 nK/second upwards through the transition (G).

III. RESULTS

The effect of the finite thermal resistivity, and of the shifted transition temperature at $T_c(q)$, are clearly visible in the right-hand side of Fig. 2, which depicts a run at $q = 21.31\mu$W/cm^2 and $P = 28.8$ bar. The horizontal dashed line represents $T_\lambda(P)$ determined from the low-current ramp. The upper and lower traces represent the temperatures at the lower and upper sideplanes respectively. The vertical dashed line represents the time at which the fluid at the cell bottom reached $T_c(q, P)$. The small difference δT between the sideplane temperatures to the left of this line is due to mutual friction. Slightly to the right of this line, $T_c(q, P)$ passes the bottom sideplane. This is used to determine the shifted onset. In the following subsections we describe the analysis of these two phenomena.

A. $R(t, q, P)$ analysis

The thermal resistivity can be determined from the sideplane spacing h, the heat-current density q and the temperature difference between the sideplanes δT via the formula

$$R \equiv \frac{\delta T}{hq} \ . \qquad (1)$$

This equation assumes a linear temperature profile in the fluid. For the small temperature differences we are considering this is a good approximation.

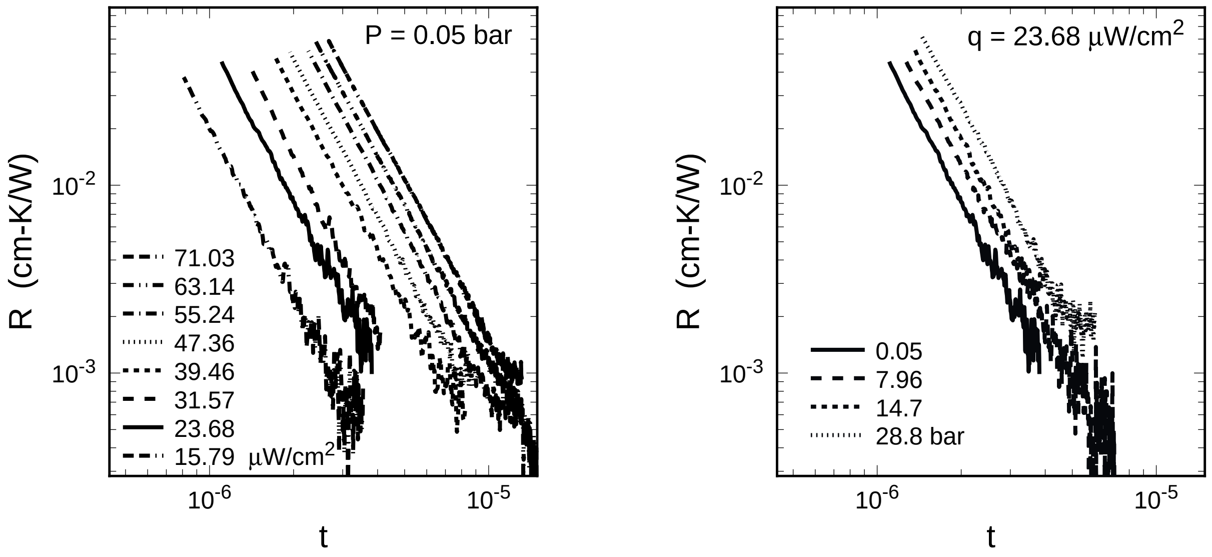

FIG. 3. The thermal resistivity R as a function of the reduced temperature t. Left: results at vapor pressure for several q. Right: results at constant q for several pressures.

The left-hand plot of Fig. 3 shows R at SVP for various q as a function of t, where now $t \equiv 1 - \langle T \rangle / \langle T_\lambda(P) \rangle$. Here $\langle\rangle$ indicates averaging the two sideplane values. These results agree with previous measurements [2] in that they exhibit both a powerlaw dependence on t and a strong dependence on q. The right-hand plot of Fig. 3 shows R at constant q for various pressures. It suggests that R is given by similar powerlaws for various pressures, but that its magnitude increases with pressure.

To interpret these results quantitatively, we used as a guide the formula

$$\nabla T = A w^m \frac{\rho_n}{s} = A_o t^{-\alpha} \left(\frac{Q}{\rho_s s T} \right)^m \frac{\rho_n}{s} \tag{2}$$

which was suggested by Gorter and Mellink to describe mutual friction [1]. Here we used on the right the equation $Q = \rho_s s T w$ [4] with $w = v_n - v_s$. Using the known critical behavior $\rho_s \propto t^\nu$ [5], we may immediately identify the t- and q-dependence of R:

$$R \equiv -\frac{\nabla T}{Q} \sim Q^{m-1} t^{-(m\nu+\alpha)} \ . \tag{3}$$

This may now be cast in another form to facilitate data analysis:

$$R = (t/t_o)^{-(m\nu+\alpha)} \ , \tag{4}$$

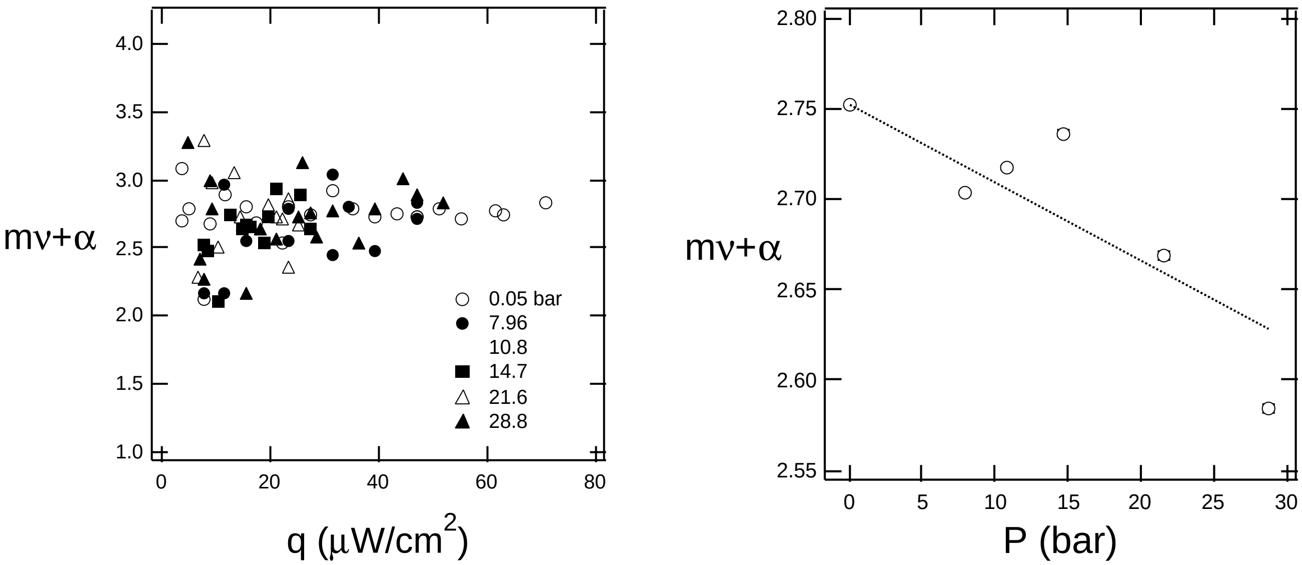

FIG. 4. The exponent $m\nu + \alpha$ of Eq. 4 and its pressure dependence.

$$t_o = (q/q_o)^x \ . \tag{5}$$

Eq. 4 and Eq. 5 are related to Eq. 3 via

$$m = 1 + x(m\nu + \alpha) \ . \tag{6}$$

Using data from, for instance, Fig. 3, we fit Eq. 4 to R to obtain $m\nu + \alpha$ and t_0. On the left side of Fig. 4 we show the results for $m\nu + \alpha$ as a function of q for several pressures. There is no systematic dependence on q. Thus an average value of $m\nu + \alpha$ was calculated for each pressure. The averages are shown on the right side of Fig. 4. The variation of $m\nu + \alpha$ with pressure can be described by the formula

$$m\nu + \alpha = (2.76 \pm 0.03) - \left(\frac{0.004 \pm 0.002}{bar}\right) \times P \tag{7}$$

In Fig. 5 we show t_0 as a function of q for each pressure. At SVP, $t_0(q)$ displays a clear power law behavior. At higher pressure t_0 shows a bit more scatter; but we assumed that it still can be described by a powerlaw. Thus, we fit Eq. 5 to the data. This yielded the values for x and q_0 shown in Fig. 6. The variation of x and q_0 with pressure can be described by

$$x = (0.929 \pm 0.001) - \left(\frac{0.0001 \pm 0.0006}{bar}\right) \times P \ , \tag{8}$$

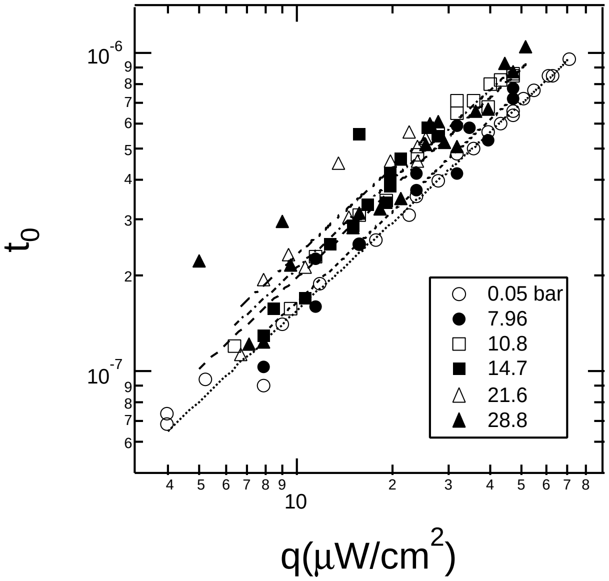

FIG. 5. The parameter t_0 of Eq. 4. The lines are fits of Eq. 5 for each P.

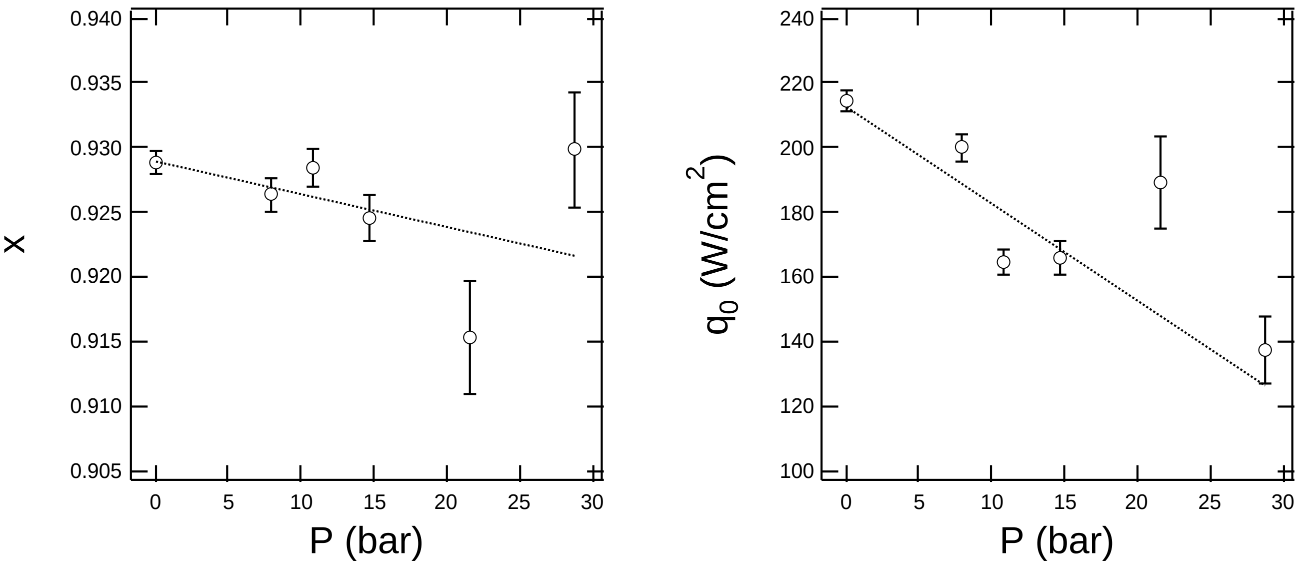

FIG. 6. The parameters x and q_o of Eq. 5 as a function of P. The straight lines are fits to the data.

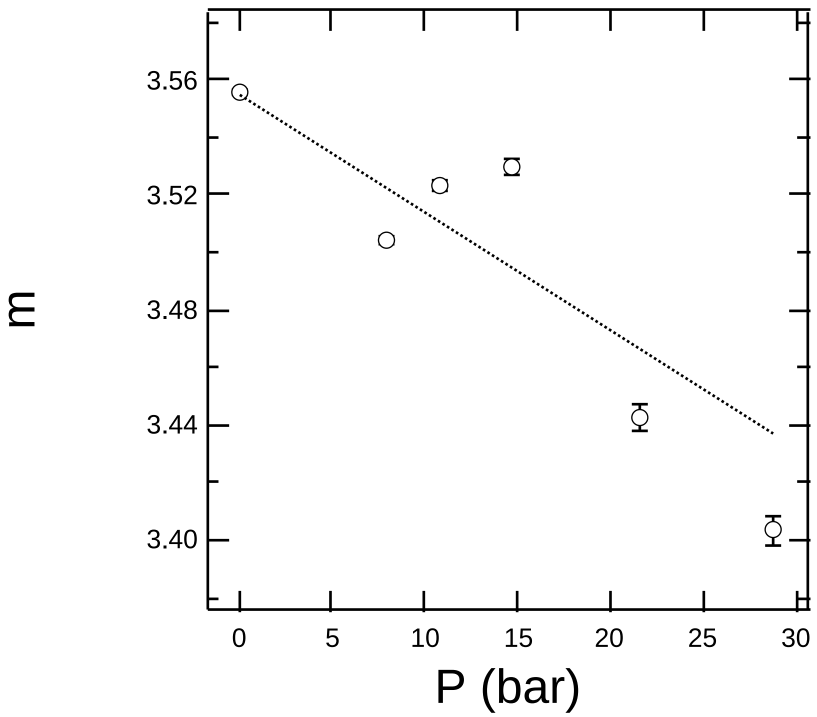

FIG. 7. The exponent m of the Gorter-Mellink mutual-friction model as a function of pressure.

$$q_0 = (215 \pm 2) - \left(\frac{2.6 \pm 1.4}{bar}\right) \times P \ . \tag{9}$$

Finally, from Eq. 6 and the measured values of $m\nu + \alpha$ and x, we obtained the results for m shown in Fig. 7. The variation of m with pressure can be described by the formula

$$m = (3.56 \pm 0.03) - \left(\frac{0.005 \pm 0.002}{bar}\right) \times P \tag{10}$$

Using simple dimensional considerations, Gorter and Mellink had argued that m should have the value 3, consistent with measurements deep in the superfluid phase. Measurements closer to T_λ, including the present ones, indicate that $m > 3$ near the transition.

B. $T_c(Q, P)$ Analysis

We now explain the procedure used to extract $T_c(q, P)$ from data like those in Fig. 2. As noted in Ref. [6], the existence of thermal dissipation below $T_c(q, P)$ for large q presents a challenge in selecting $T_c(q, P)$ because the transition appears "rounded". Now, however,

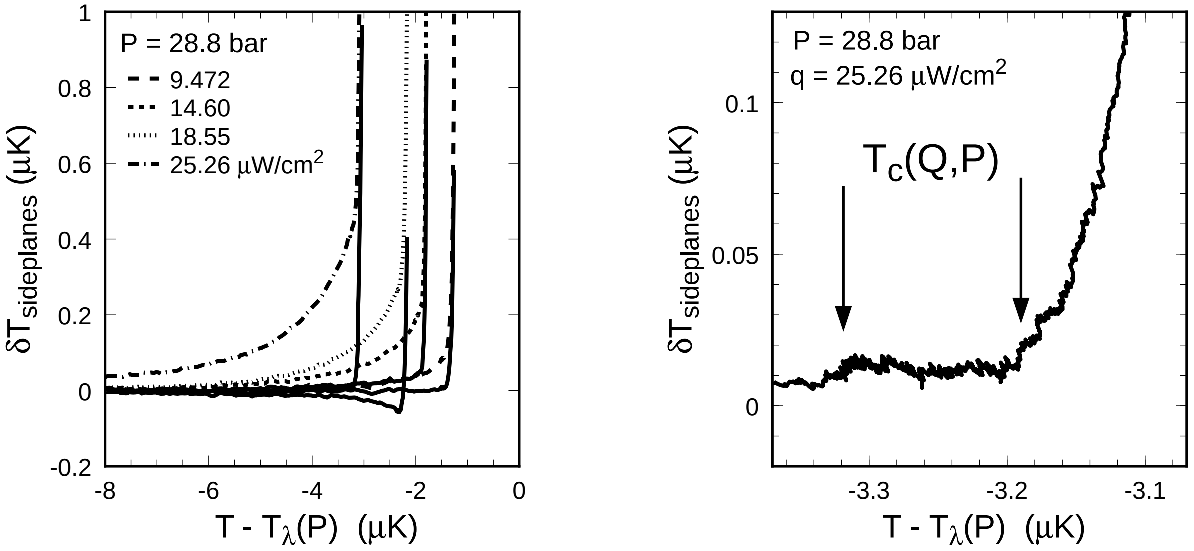

FIG. 8. Left: the temperature difference δT between sideplanes before (broken trace) and after (adjacent solid trace) mutual friction subtraction as a function of the fluid temperature at the bottom side plane. Right: An expanded view. The arrows show the temperatures at which $T_c(q,P)$ arrived at the cell bottom (left arrow) and at the cell side bottom (right arrow).

having determined the behavior of $R(t,q,P)$ near $T_\lambda(P)$, we may remove its contribution to δT. The residual signature in δT of the onset of dissipation is much sharper. It can be used to determine $T_c(q,P)$ with good resolution.

The data shown on the left hand side of Fig. 8 is taken at 28.8 bar. The abcissa is the fluid temperature measured by the bottom sideplane thermometer. Each of the broken lines represent a temperature difference δT between the sideplane thermometers for a particular q. Associated with each broken line is a solid line which represents the temperature difference δT after the contribution from mutual friction was subtracted. The mutual friction model did not fit the data perfectly as is obvious from the ramps at 14.60 and 18.55 μW/cm^2. However it worked remarkably well for some of the runs, as is clear from the ramps at 9.47 and 25.26 μW/cm^2.

After the mutual-friction subtraction, the residual increase in δT provides a sharp signature of $T_c(q,P)$. The right-hand side of Fig. 8 gives a closer look at the 25.26μW/cm^2 run. Starting from the left of the figure, the first arrow points to the temperature at which

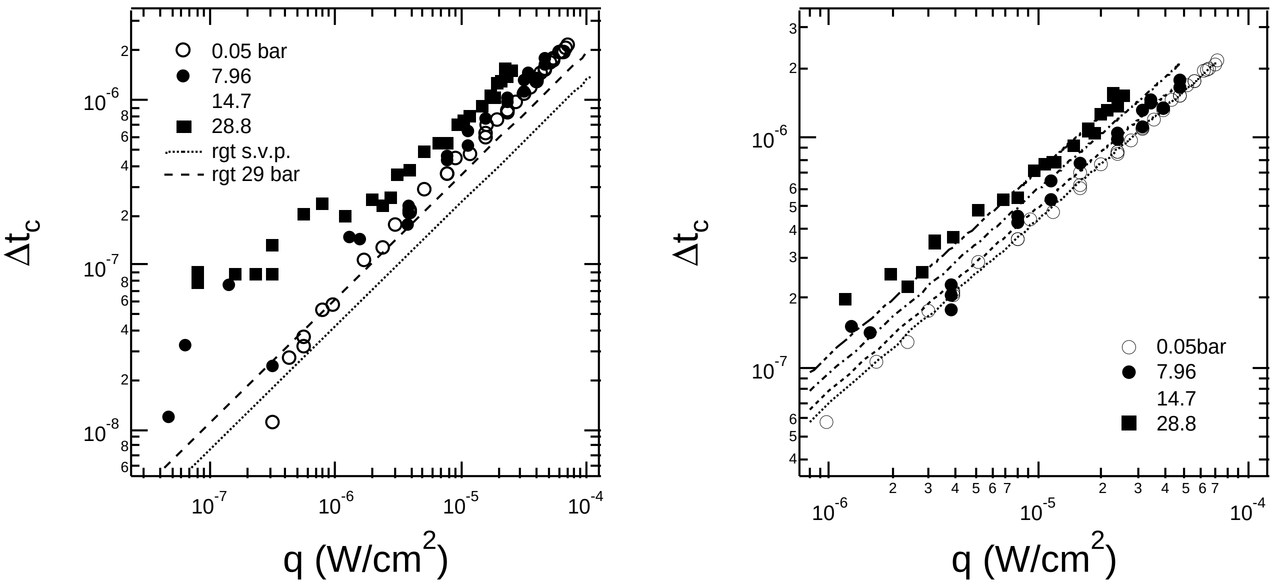

FIG. 9. Left: The depression of the critical temperature as a function of q and P and theoretical predictions [7] at $P = 0.05$ and 28 bar. Right: An expanded view in the high-q region and fits of Eq. 11 to the data.

the cell bottom reached $T_c(q, P)$. This is apparent from the increase in the density of data points—the ramp rate slows down due to the development of a highly dissipative He I layer at the cell bottom. The second arrow points to the region where δT has begun to develop between the sideplanes: the bottom sideplane has reached $T_c(q, P)$. In order to avoid possible effects of the copper-He^4 boundary upon the transition, this temperature was used to determine $T_c(q, P)$.

In Fig. 9 we show the results for $\Delta t_c(q, P) \equiv 1 - T_c(q, P)/T_\lambda(P)$ and the theoretical predictions from Ref. [7]. A power law of the form

$$\Delta t_c(Q, P) = (q/\Delta_0)^y \quad . \tag{11}$$

may be fit to the data. This fit describes the data remarkably well at large q. At small q and at high pressure, there are deviations as well as more scatter. However, there exists a discrepancy between the measured and predicted values of $\Delta t_c(q, P)$ which is much larger than any experimental uncertainties. This was observed in previous experiments [6]. Interestingly, the pressure dependence of $\Delta t_c(q, P)$ predicted by the theory is consistent with the

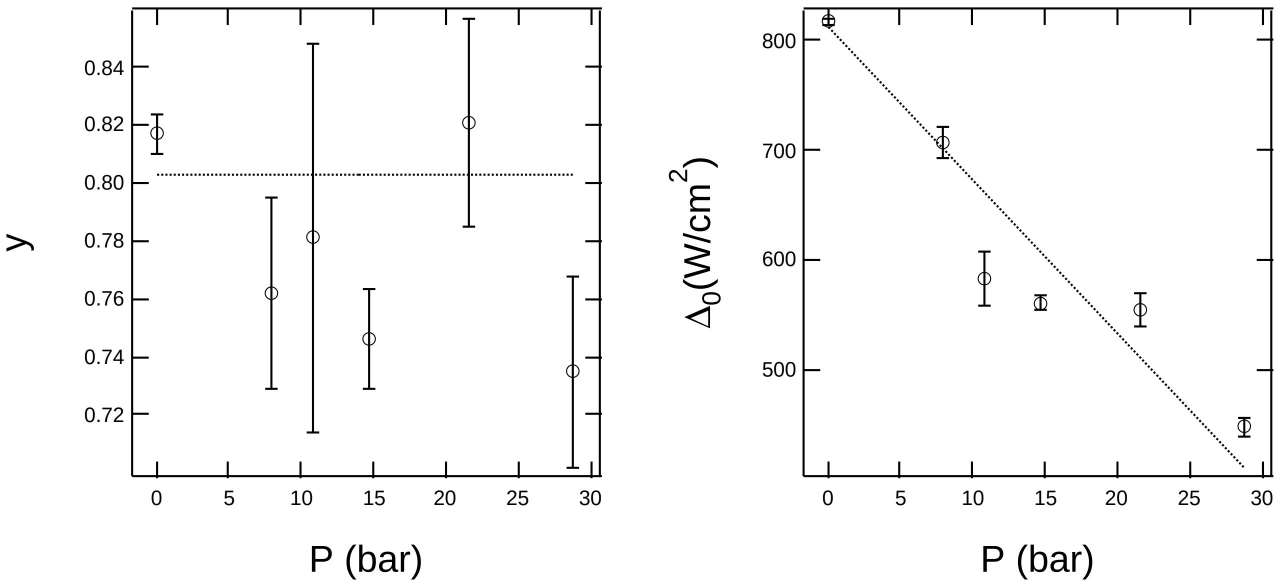

FIG. 10. Left: The parameter y of Eq. 11 as a function of pressure (circles), and the average value $y = 0.803$ (horizontal line). Right: The parameter Δ_0 of Eq. 11 obtained from a fit of Eq. 12 to the data when x is fixed at 0.803.

measurements.

Shown on the left hand side of Fig. 10 is the parameter y obtained from fitting Eq. 11 to the data at various pressures. The 0.05 bar exponent $y = 0.817$ agrees with previous results at saturated vapor pressure [6] which yielded $x = 0.813$. At high pressures, y falls a bit lower. To proceed, we assumed that y, in accordance with theoretical predictions, is pressure independent, fixed y at the pressure-averaged value $y = 0.803$, and repeated the fit to extract the amplitude Δ_0. The result clearly decreases with pressure, as shown in Fig. 10. A linear fit yields

$$\Delta_0 = (812 \pm 3) - \left(\frac{13.9 \pm 0.3}{bar}\right) \times P \ . \tag{12}$$

IV. ACKNOWLEDGMENT

This work was supported by NASA through Grant No. NAG3-1847.

REFERENCES

[1] C.J. Gorter and J.H. Mellink, Physica **15**, 285 (1949).

[2] H. Baddar, G. Ahlers, K. Kuehn, H. Fu, J. Low Temp. Phys. **119**, 00 (2000).

[3] D.F. Brewer and D.O. Edwards, Phil. Mag. **6**, 775 (1961).

[4] F. London, *Superfluids* (Wiley, New York, 1954) Vol.2.

[5] A. Singsaas and G. Ahlers, Phys. Rev. B **29**, 4951 (1984).

[6] R.V. Duncan, G. Ahlers, and V. Steinberg, Phys. Rev. Lett. **60**, 1522 (1988).

[7] R. Haussmann, Phys. Rev. B, **60**, 12349, (1999).

[8] K.G. Wilson and M.E. Fisher, Phys. Rev. Lett., **28**, 240, (1972).

[9] P.C. Martin, E.D. Siggia and H.A. Rose, Phys. Rev. A, **8**, 423, (1973).

Nonequilibrium and non-uniform near-critical states

Alexander Patashinski
Northwestern University

Scale invariance of critical fluctuations determines the structure of near-critical states appearing when the regime of critical point is perturbed by a temperature or other thermodynamic coordinates shift or by external conditions that violate the uniformity or equilibrium in the system. Critical exponents, universal amplitudes and other predictions of the theory for the equilibrium uniform states are confirmed by the experiment. A much more severe test of the physical picture underlying the scaling theory and the renormalization group is the response of the critical system to perturbations of non-equilibrium nature (perturbations out of the thermodynamic plane). The nonequilibrium near-critical state attracted little attention from experimental physicists partially because of absence of theoretical predictions and clarifications of optimal experimental situations. The number of possible nonequilibrium and/or non-uniform states is infinite, and the first step here is to find situations that may serve as a standard set for the experimental study of non-uniform and nonequilibrium criticality. We present the results of a study of selected situations and effects in non-equilibrium near-critical state proposed for experimental study in microgravity, including relaxation following a rapid homogeneous change of pressure/temperature and fluctuations and boundary effects in systems with a temperature gradient.

Review: Impact of the Space Radiation Environment on Experiments of the Fundamental Physics Discipline, Energy Deposition by Neutrons and Solar Energetic Particles, and a Proposed Direct Measurement

STP Boyd, RV Duncan, University of New Mexico
WA Holmes, Jet Propulsion Laboratory, Caltech

The "laboratory environment" in space really has two new features for physics experiments: microgravity and radiation. In the Fundamental Physics Discipline we generally concentrate on the microgravity, but the penetrating components of the space radiation environment are unavoidable, and have proven capable of strongly perturbing precision measurements. To avoid making expensive mistakes, it is useful to improve our understanding of the space radiation environment and its effects on physics experiments. As a component of the DYNAMX experiment we have an ongoing effort to understand and estimate the effects of the space radiation environment on precision physics experiments. We review the basics of the space radiation environment, how the physics of "heating" differs from both the physics of standard radiation dosimetry and from "biological effectiveness," and our present estimations of the heating to be seen on the ISS orbit. New considerations of the impact of neutrons and solar energetic particles will be presented. We discuss the unique capabilities afforded by cryogenic radiation measurements and a proposed plan for a dedicated small "add-on" experiment (CCRAD) to measure and monitor the space radiation environment and its effects during cryogenic experiments of the Fundamental Physics Discipline.

A Continuous, Sorption-Pumped
^{3}He Cooler for Space

Pat Roach, NASA Ames Research Center

Abstract

For reaching temperatures below 1 K in space, it is natural to think of ^{3}He coolers, which can cool to below 0.3 K. In order to maximize the duty cycle it is desirable to have a cooler that operates continuously. A method is presented for achieving this using two sorption-pumped ^{3}He coolers operating alternately. The thermal switching required is performed with ^{3}He heat pipes that are configured to act as thermal diodes. Such a ^{3}He cooler can be the basis of a continuous dilution cooler reaching 0.05 K; a continuous dilution cooler can be the basis of an adiabatic demagnetization refrigerator that can reach 0.002 K.

A Continuous ^{3}He Cooler

Figure 1 is a schematic of a continuous ^{3}He cooler. It consists of two pots of liquid ^{3}He that can be pumped by canisters of charcoal. On the right side of Fig. 1 is shown a ^{3}He pot that is condensing ^{3}He that is being driven out of its charcoal by heating the charcoal to 40 K. A heat sink at 2 K provides cooling to condense the liquid. On the left of Fig. 1 is a pot that is at 0.4 K. Its charcoal pump is cooled to 10 K by exchange gas coupling the inner charcoal canister to the 10 K heat sink. At 10 K the charcoal will pump the ^{3}He very effectively and cools the attached pot to 0.4 K by evaporative cooling. The pots will be tested on the ground with a porous matrix of copper in them. This matrix is needed in

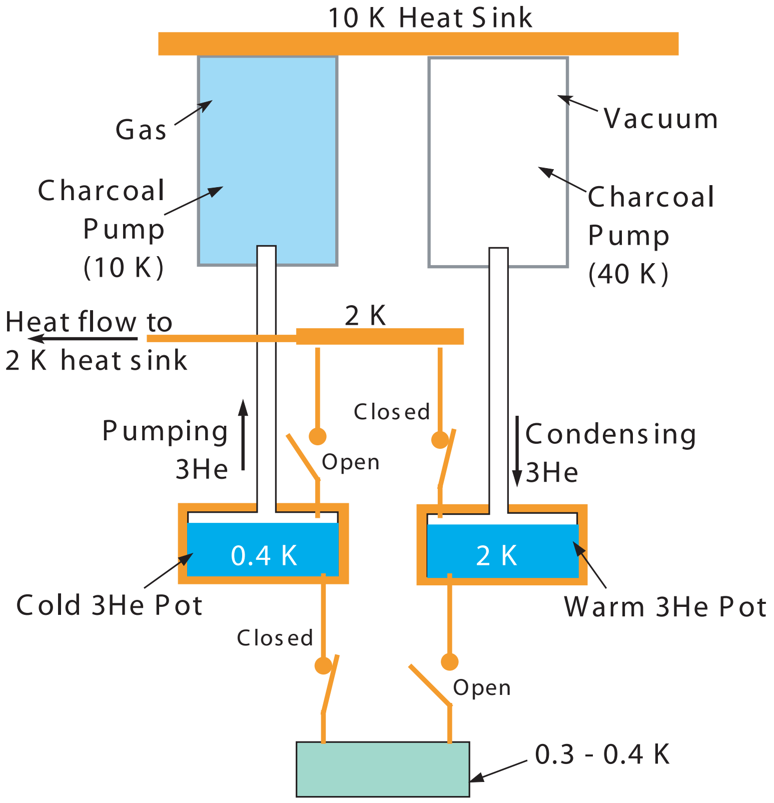
10 K Heat Sink
Gas
Vacuum
Charcoal Pump (10 K)
Charcoal Pump (40 K)
Heat flow to 2 K heat sink
2 K
Closed
Open
Pumping 3He
Condensing 3He
0.4 K
2 K
Cold 3He Pot
Warm 3He Pot
Closed
Open
0.3 - 0.4 K

Fig. 1. A continuous ^{3}He cooler.

A New Low Temperature Device for High Resolution, In Situ Measurement and Control of Submicron Gaps

Tamar More, Clifford Dax, Joseph Niemela

Department of Physics,
University of Oregon,
Eugene, OR 97403

Gary Ihas

Center for Ultra Low Temperature Research,
P.O. Box 118440, University of Florida,
Gainesville, FL 32611

abstract

We have developed a device to investigate finite-size scaling of the thermal expansion coefficient in liquid helium near the lambda transition. Motivated by the need for a range of well known, uniform, sub-micron gaps with constant surface conditions, we have built a variable-gap parallel-plate capacitor that can be adjusted in situ. We measure the gap at three points using laser interferometry. A careful choice of the material and thickness of the reflecting surfaces results in asymmetric fringes, for which both exceptional sensitivity and a high contrast ratio can be achieved simultaneously. Both the gap size and its uniformity are actively controlled using voice coil actuators. This design has a number of additional benefits: the gap can be kept closed until low temperature use, data can be collected for all gaps with no thermal cycling, and no spacers are needed to establish the gap.

INTRODUCTION

The boundary conditions and physics that pertain to a solid/fluid or fluid/vacuum interface are an important problem throughout condensed matter science. In general, this area is difficult to study because the fluid properties are affected only a few angstroms from the interface. This is not the case near a phase transition, where the correlation length diverges as the transition is approached. A study of the boundary layer, made macroscopic by the approach to the phase transition, is possible in such systems.

Renormalization group (RG) theory leads to very general concepts of universality and scaling, which apply to all phase transitions. Since these predictions are exact for any physical system of a given class, this situation is begging that very precise measurements be made to test this theory. Under intense scrutiny for decades, the lambda transition in helium, a line of critical points, has been the archetype used to develop and test the theory as applied to phase transitions. In particular, much experimental work has been done to test scaling theory in a system that is passing from bulk, or 3 dimensional behavior, to the 2 dimensional behavior of a slab geometry (see Mehta and Gasparini and references therein). And, recently, theories have predicted exact results for confined liquid helium (see Sutter, Schmolke, and Huhn). The scaling depends on the thickness of the helium slab, and most experiments investigate one or at most 4 thicknesses. In addition, the lambda transition temperature is a function of pressure. Here we present an apparatus in which the thickness d may be varied continuously, in situ, from 100 Angstroms to 30 microns.

To test scaling, we wish to measure a quantity that diverges as the phase transition is approached. Such quantities include the thermodynamic response functions: heat capacity Cp, isobaric thermal expansion coefficient, or isothermal compressibility. After considering which parameter is most easily measured without experimental artifact, which will complement the measurements already done and being planned for space, and which might be the next best candidate for flight, we chose a capacitor technique to measure the dielectric constant. Capacitance measurements are very precise and are not susceptible to the addenda problems that plague heat capacity measurements. The dielectric constant can be converted to density with the Clausius-Mossotti relation, and the derivative of the density with respect to temperature at constant pressure to the expansion coefficient. The expansion coefficient, in turn, is related to the heat capacity.

Our first attempt to study this problem involved using two very precisely made, small-gap capacitors with the gap fixed by spacers, but these proved unreliable, often shorting on cool-down. Since the gap was fixed, a series of capacitors and experimental runs were needed to investigate size effects. This was a very expensive and time-consuming course to pursue and the smallest gap that was achieved was 2 microns. In addition, the sample cell was subject to inevitable changes in surface conditions between runs, providing an unknown and uncontrolled parameter in the measurements. These travails led to a completely new approach to the apparatus. A capacitor has been designed whose gap may be varied without need for disassembly, while maintaining a very precise level of parallelism. Furthermore, the gap may be changed while the apparatus is cold and filled with helium. One advantage of this design is that the capacitor can be parked with a very small gap. This small gap will act as a filter to keep dust out while the capacitor is being transported to, and mounted on, the cryostat. Other advantages, discussed elsewhere, also make this new capacitor design very exciting.

The gap is formed by two highly polished fused silica plates, the lower one movable and the upper one fixed. Coarse height and tilt adjustments may be made before the cell is sealed via 3 screws; in operation, the gap is determined and maintained parallel by a feedback system of 3 servo-actuators. The feedback is provided by measurements of interference fringes produced by 3 Fabry-Perot interferometers, one above each actuator. A thick Au film on the upper surface of the lower (movable) plate serves as one of the Fabry-Perot mirrors and as one of the capacitor electrodes. On the upper plate are the partially reflecting Fabry-Perot mirrors and a set of electrodes.

To maintain parallelism and correct spacing (gap), the light from a 670 nm laser beam is split into 3 beams. Each beam then passes through a diplexer, which is simply a Cr/Au mirror with a pinhole. The light travels through the multimode fiber optics and is focused onto the interferometer mirrors. The beams then reflects back into the fiber optics. When they return to the diplexers, most of the light reflects into photo diodes, as shown. This signal is used to control the current to the coils.

SCHEMATIC OF
ADJUSTABLE-GAP
CAPACITOR.

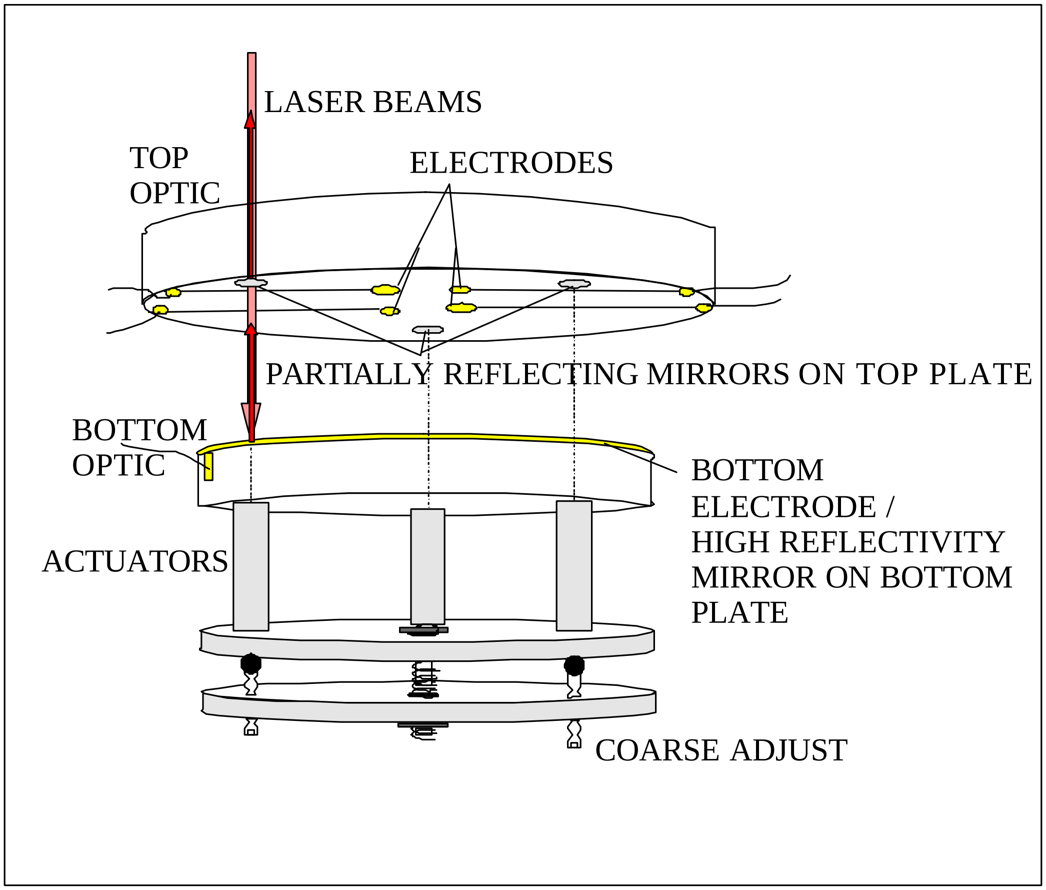
LASER BEAMS
TOP
OPTIC
ELECTRODES
PARTIALLY REFLECTING MIRRORS ON TOP PLATE
BOTTOM
OPTIC
BOTTOM
ELECTRODE /
HIGH REFLECTIVITY
MIRROR ON BOTTOM
PLATE
ACTUATORS
COARSE ADJUST

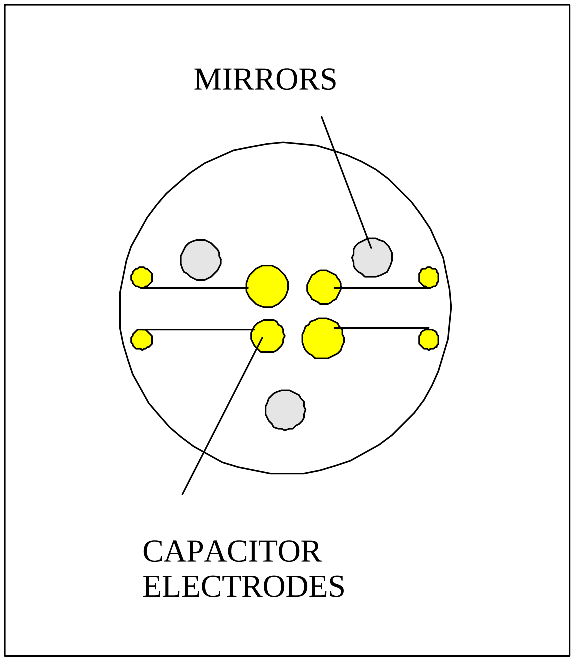
MIRRORS
CAPACITOR
ELECTRODES

VIEW OF UPPER OPTIC

ELECTRODES AND MIRRORS
ARE DEPOSITED ON
FUSED SILICA PLATES.

INTERFERENCE OF LASER
BEAMS REFLECTING AT
MIRRORS PROVIDES
FEEDBACK TOACTUATORS.

COARSE ADJUSTMENTS
ARE MADE AT ROOM
TEMPERATURE
BEFORE SEALING THE
CELL.

Here are some photos of the device:

Bottom part of cell with bottom optic and coil assembly installed

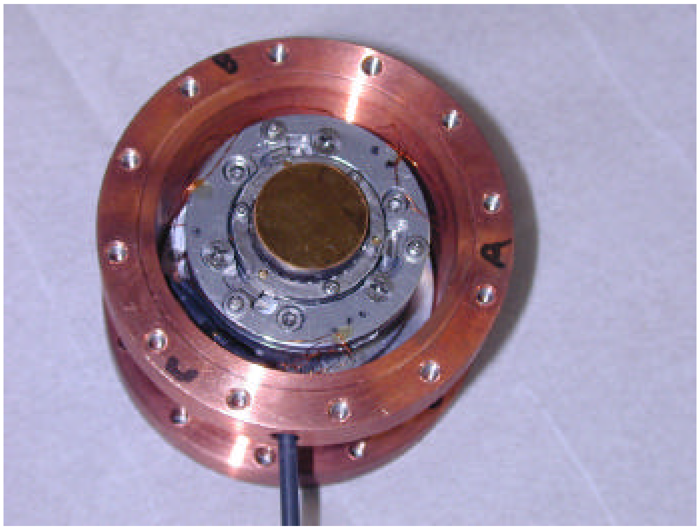

Closed cell with fiber optics

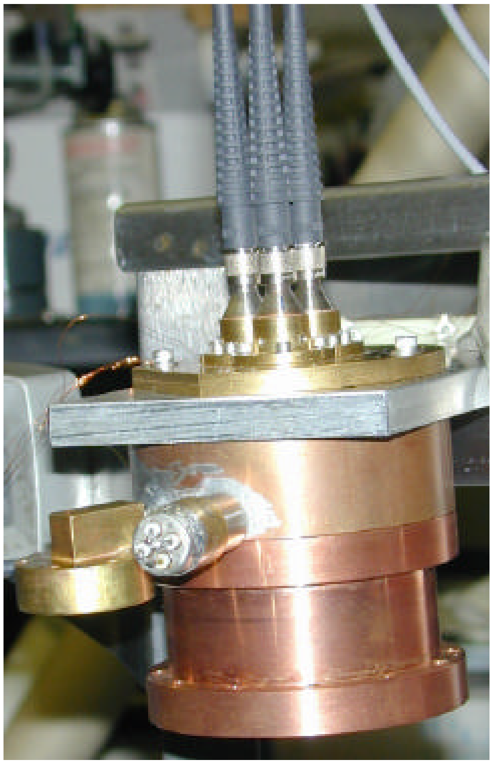

Coarse adjust

Magnets and holder

Bottom optic assembly

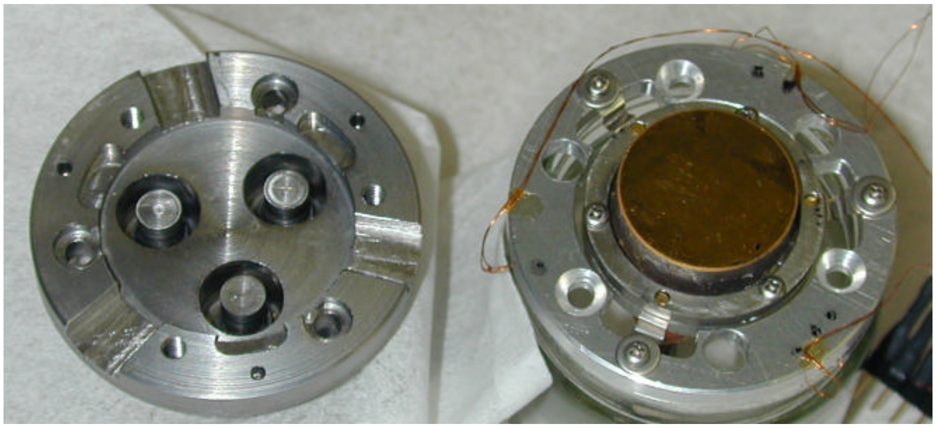

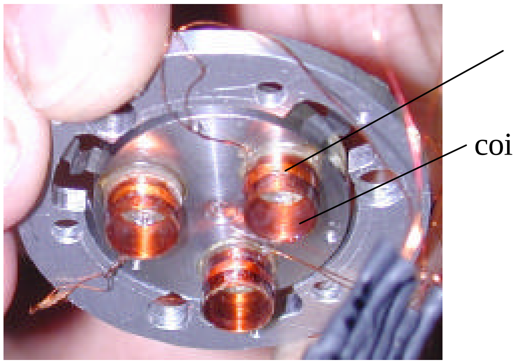
magnetic damping
coils

OPTICAL ENGINE

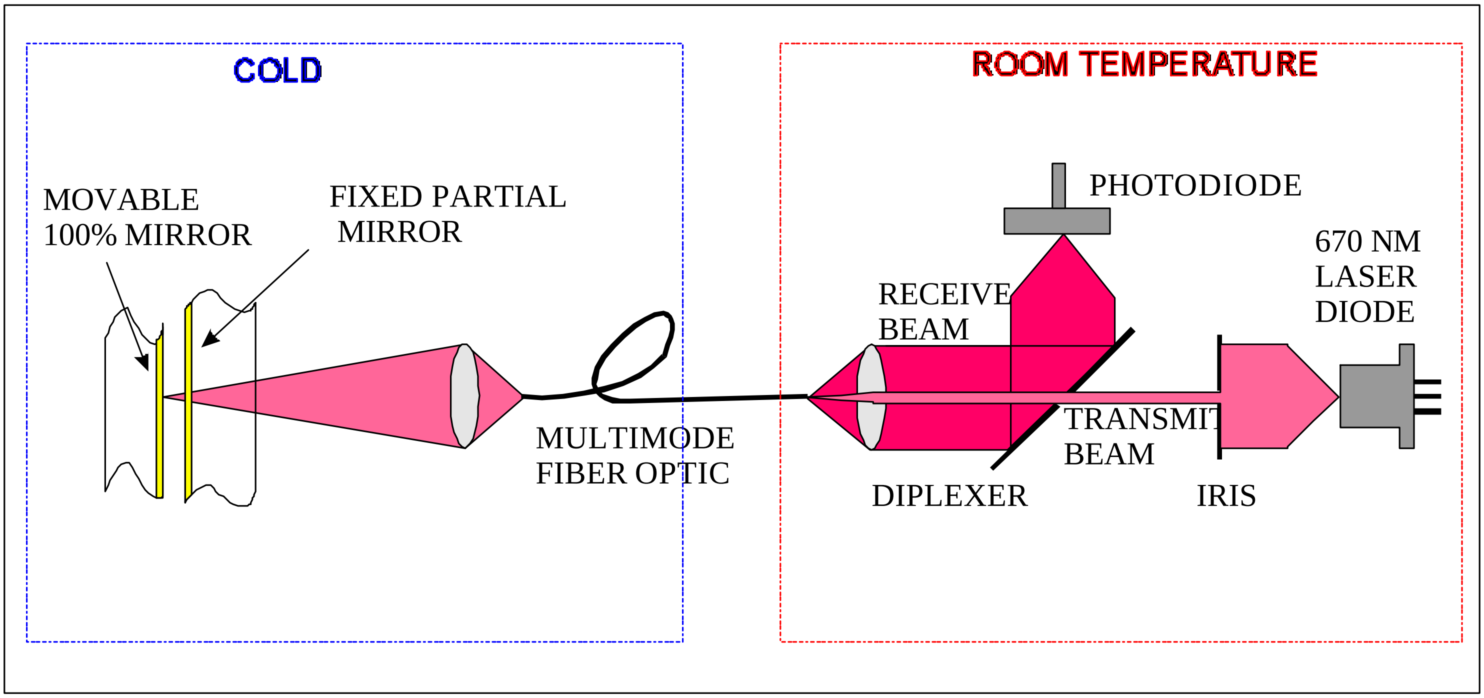
COLD
ROOM TEMPERATURE
MOVABLE 100% MIRROR
FIXED PARTIAL MIRROR
MULTIMODE FIBER OPTIC
PHOTODIODE
670 NM LASER DIODE
RECEIVE BEAM
TRANSMIT BEAM
DIPLEXER
IRIS

- Light from a 670 nm laser beam is split into 3 beams.

- Each beam passes through a diplexer, which is simply a Cr/Au mirror with a pinhole.

- The light travels through the multimode fiber optics

- It is then focused onto the interferometer mirrors.

- The beams then reflects back into the fiber optics.

- When they return to the diplexers, most of the light reflects into photo diodes.

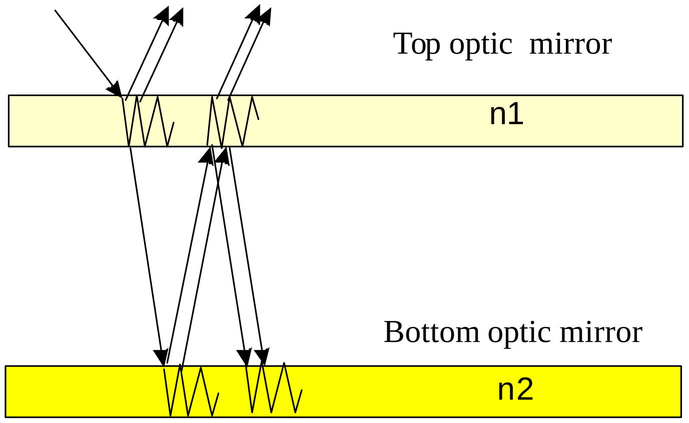

Absorption in the films forming the mirrors produces an asymmetry in the reflected interference fringes.

A steep gradient and high contrast ratio are key to achieving precise control of the gap.

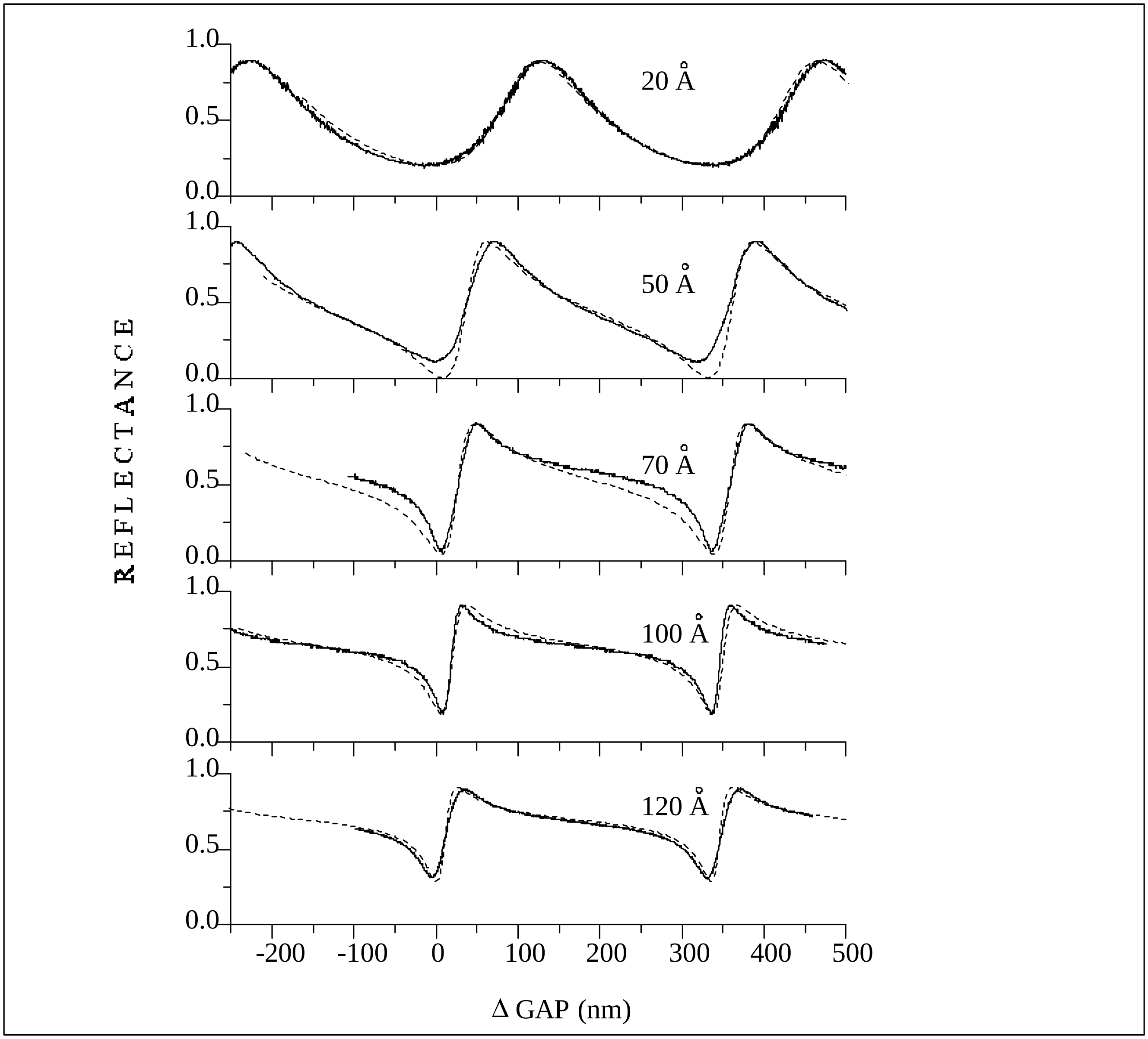

measurements (solid line) and calculation of reflectance as function of change in gap for aluminum (n1=1.8+8.0i) on top optic and gold (n2=0.16+8.8i) on bottom optic. Thickness of aluminum film is indicated on each plot.

A number of options for actuators exist.

These include
- Piezo-electric stacks,
- Voice-coils,
- Magneto-strictive devices,
- Pressure transducers,
- etc.

Initially, we used piezo-electric stacks.

We are currently developing a device with voice-coil actuators.

PIEZOELECTRIC ACTUATORS

In our first design, we used piezoelectrics stacks as actuators. Our stacks are approximately 5 cm tall and have a stroke of 40 µm at 100 V at room temperature, but only 1µm at 4.2 K.

advantages:

These are voltage-driven devices with an extremely high impedence.
There is a direct relationship between voltage and position.
They are mechanically connected to the optical mount.

disadvantages:

The stroke at 4.2 K is only 1mm (lever and flexture system increased the motion at the optic to 6 mm).
They are tall.
They are expensive.

Schematic of cell with piezoelectric actuators

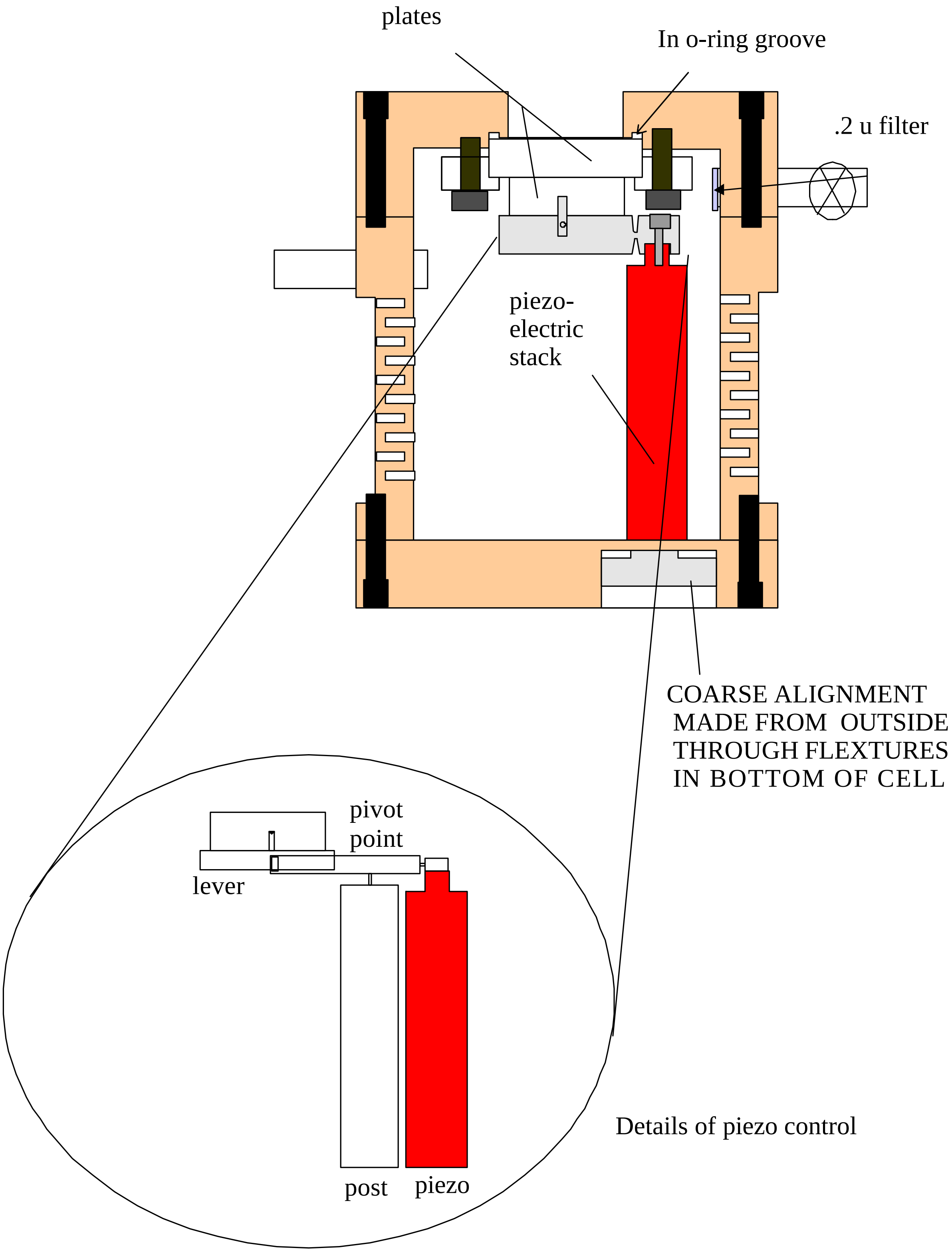
plates
In o-ring groove
.2 u filter
piezo-
electric
stack
COARSE ALIGNMENT
MADE FROM OUTSIDE
THROUGH FLEXTURES
IN BOTTOM OF CELL
pivot
point
lever
post
piezo
Details of piezo control

VOICE COIL ACTUATORS

In our current design, we use voice coils as actuators. These currently have a stroke of 75 µm at 200 mA at both room temperature and 4.2 K. It should be possible to increase the stroke per unit current by optimizing the design further (increase the number of turns, change the magnets, decrease the magnet-coil gap).

advantages:

The range of motion is much greater than with the piezos.
The coils are only about 1 cm tall, so the cell can be much smaller.
The coils are simple and inexpensive to make.

disadvantages:

The current directly controls force, rather than position.
When not actively controlled, this design is more susceptible to vibration.
Cross-coupling is greater than with the piezos.

Schematic of cell with voice coil actuators

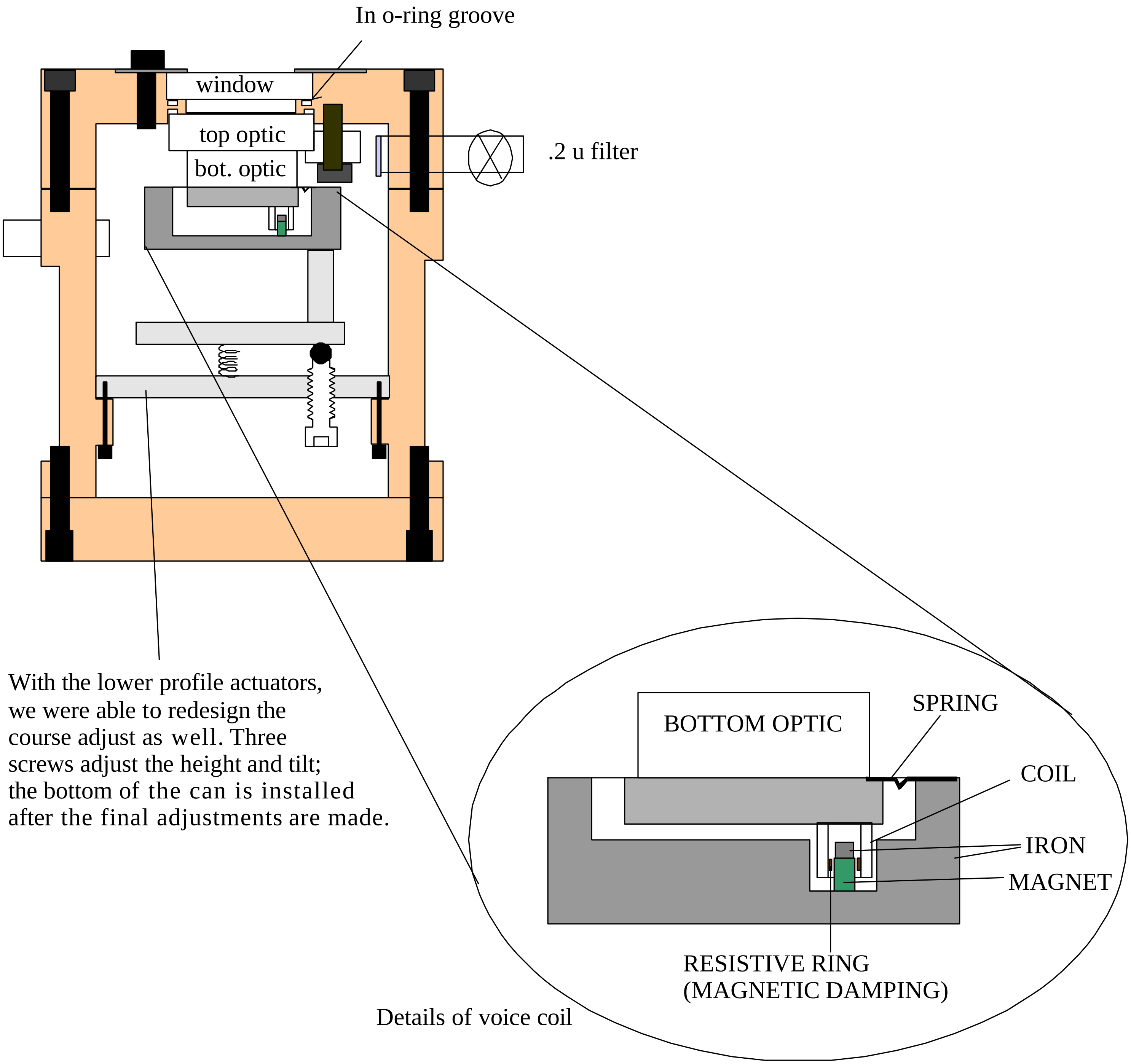
In o-ring groove
window
top optic
bot. optic
.2 u filter
BOTTOM OPTIC
SPRING
COIL
IRON
MAGNET
RESISTIVE RING
(MAGNETIC DAMPING)

With the lower profile actuators, we were able to redesign the course adjust as well. Three screws adjust the height and tilt; the bottom of the can is installed after the final adjustments are made.

Details of voice coil

CONTROL ALGORITHM

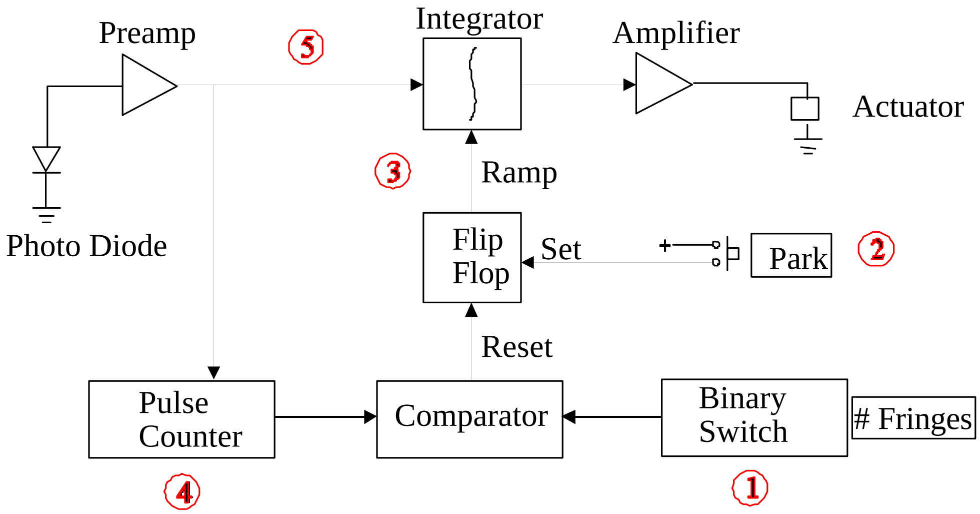
Preamp
⑤
Integrator
Amplifier
Actuator
Photo Diode
③
Ramp
Flip Flop
Set
Park
②
Reset
Pulse Counter
Comparator
Binary Switch
# Fringes
④
①

① The desired gap, in units of fringes (335 nm), is set.

② The bottom plate is moved up until it touches the upper plate.

③ A ramp current applied to the coils (or voltage to the piezos) lowers the bottom plate.

④ This produces an oscillating signal at the photo diode. A pulse counter keeps track of the number of oscillations (fringes).

⑤ When the number of fringes corresponding to the desired gap have been recorded, the feed back loop is closed. The current in the coil (voltage of the piezo) is controlled to maintain the photo diode signal at a constant intensity.

Photo diode output with the feedback loop closed
using the piezo-electric stack actuators at room temperature.

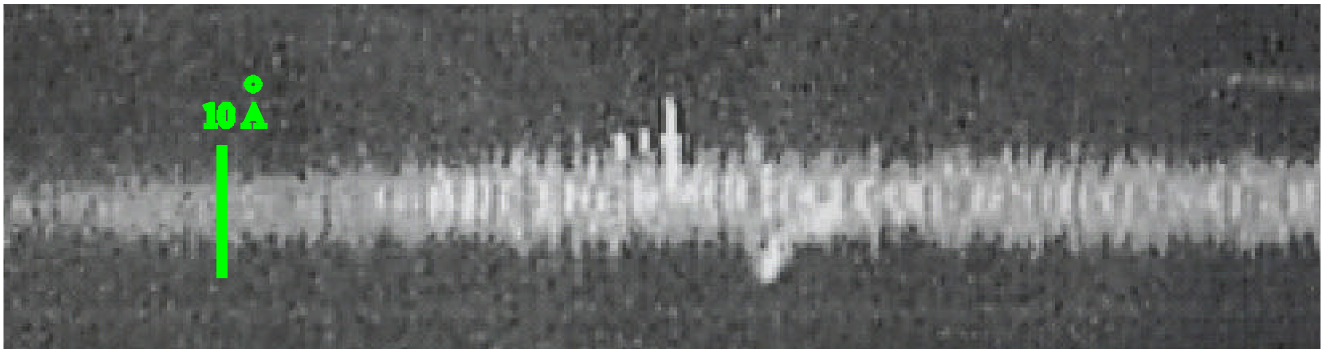

CONCLUSIONS

We offer improvements and innovations which will allow scaling theory to be tested in a more precise and extreme manner than ever before.

The thickness of the slab is adjustable, in situ and while cold.

The thickness of the gap can be adjusted over 2 orders of magnitude, spanning bulk to confined behavior.

The slab thickness may be varied in one cool-down, allowing a complete test of finite-size scaling theory.

The uniformity of the slab thickness (capacitor gap) is regulated using 3 optical interferometers.

The surfaces (capacitor plates) defining the helium slab will be the same for all measurements, something never achieved before.

There will be no non-helium material between the electrodes, such as spacers, avoiding problems with temperature-dependent materials masking the scaling law dependence.

Our apparatus enables us to pursue another very exciting possibility. With the gap wide, one may pool a helium film of some thickness on the lower plate. This film would then have one boundary condition determined by a solid surface and the other exposed to vacuum. Then, after measuring the dielectric constant as a function of reduced temperature, the bottom plate is moved so that the top plate contacts the helium with a gap equal to the free film thickness just investigated. The second set of measurements now taken will be able to directly determine, for the first time, the nature of the vacuum/film interface.

BIBILIOGRAPHY

S. Mehta and F. M. Gasparini, Phys. Rev. Lett. 78, 2596 (1997).

Sutter, P., Dohm, V.,Physica B 194-195, 613 (1994).

Schmolke, R., Wacker, A., Dohm, V., Frank, D., Physica B 165-166, 575 (1990).

Huhn, W., Dohm, V., Phys. Rev. Lett. 61, 1368 (1988).

J. J. Monzon and L. L. Sanchez-Soto, "Reflected fringes in a Fabry-Perot interferometer with absorbing coatings," J. Opt. Soc. Am. A 12, 132-136 (1995).

J. Holden, "Multiple-beam interferometry: intensity distribution in the reflected system," Proc. Phys. Soc. 62, 405-417 (1949).

SPECIFIC HEAT OF HELIUM CONFINED TO CYLINDERS NEAR THE LAMBDA POINT

J. A. Lipa and M. Coleman
Physics Department, Stanford University, Stanford CA 94305

We report the preliminary analysis of measurements of the specific heat of helium confined to very uniform 8-micron diameter cylinders and to 0.26 micron diameter Anopore cylinders in the temperature region near the lambda point. The data allow improved tests of the emerging theory of finite size phenomena and cross-over to lower dimensional states. We find generally good agreement with scaling using exponents derived by renormalization and other methods. We also find reasonable agreement with more detailed calculations of cross-over behavior based on explicit inclusion of boundary conditions. However some aspects of the scaling of the 8-micron data were unexpectedly poor.

INTRODUCTION

The study of bulk three-dimensional condensed matter has occupied the attention of physicists for a very long time. Less well studied are lower-dimensional systems, primarily because the techniques available are more restricted, and also because idealized systems are rather hard to prepare. In many cases, for true one or two-dimensional behavior, it is necessary to operate with sample dimensions below the nanometer range. This means that substrate interactions are often important via the action of Van der Waal's forces and other surface phenomena. The resulting properties can then be highly perturbed from their expected substrate-free values, making it very difficult to test theories of cross-over to lower-dimensional systems.

Of significant current interest[1] is the study of cross-over behavior observed in liquid helium near the lambda point, as the bulk is confined more and more tightly in one or more dimensions. The case of helium is especially important because of the ideal nature of the system, and the possibility of working with an extremely wide range of correlation lengths, from Ångstroms to tens of microns. The effective length scale can easily be varied by taking advantage of the divergence of the correlation length ξ as the superfluid transition is approached. Close enough to this transition, ξ can reach the micron scale[2], allowing measurements where substrate effects are essentially negligible. A recent flight experiment, CHEX, measured the effect of confinement to a parallel plate geometry with an average gap of 57 microns[3]. This data compared well with lower accuracy results[4] with sub-micron gaps and extended our confidence in the models of confinement. However, the existence of the Kosterlitz-Thouless transition in 2 dimensions decreases the value of all 2-dimensional data at least below the bulk transition, as it provides a mechanism for a range of potential breakdowns of scaling. The case of cylindrical confinement does not suffer from this potential defect, simplifying the comparison between scaling theory and experiment.

The development of very uniform arrays of cylindrical holes for imaging devices has opened up the possibility of working with large, regular confining dimensions where the problems with the substrate are expected to be greatly reduced. Here we report new measurements of the specific heat of helium confined to 8-micron cylindrical holes which have exceptionally uniform diameters and smooth surfaces. The results show confinement effects in the region where $\xi \geq 1$ micron, greatly exceeding the range of the Van der Waals interaction, and the scale of typical surface roughness in the holes. Also, the effects span a temperature region only a few microdegrees wide near the lambda transition, allowing the straight-forward application of asymptotic scaling in the analysis. To obtain data for a substantially different confinement length, we chose Anopore which can be obtained with a pore size close to the maximum used in previous work[5]. Some results from this system are also presented. The work described here is a continuation of an earlier effort with an improved calorimeter and also an extension to the case of helium confined to Anopore with an average pore size of 0.26 microns. Surprisingly, we find that the new 8 micron results do not compare well with other measurements in the region of the peak. Elsewhere, the comparison is reasonably good. The Anopore results are in reasonable agreement with earlier results[5] at small pore diameters.

APPARATUS

The measurements were made using a specially designed calorimeter and the standard heat pulse technique for determining heat capacity. To obtain an acceptable signal-to-noise ratio very near the transition, temperature changes were sensed using a paramagnetic salt thermometer[6] with a noise level of about $3\text{x}10^{-10}$ K/√Hz. One of the quantities of interest in the experiment is the displacement of the confined helium specific heat maximum relative to the bulk transition temperature. For 8 micron pores, this displacement is expected to be at most a few microdegrees, well beyond the precision with which the absolute temperature can be established. To measure the shift, the calorimeter was divided internally into two chambers connected by a very small passage. The design is shown schematically in figure 1. The lower chamber was tightly fitted with three microchannel plates[7] that consist of a glass matrix in which many fine circular holes have been etched, with a free volume of about 60% of the total. Electron microscope pictures show that these holes are uniform in size to ≤ 2%, and free of any visible surface roughness at magnifications up to 10^4. The height of this chamber was .85 mm. The upper chamber of the calorimeter was an annular cavity with a height of 0.75 mm, designed to give a small but clear heat capacity signal with essentially bulk behavior. This chamber also contained a valve which permitted the fill line to be evacuated after both chambers were filled, thus reducing the associated heat leak to the surroundings. The body of the calorimeter was made from high thermal conductivity copper to minimize thermal gradients during the measurements. In the temperature region studied the thermal response was usually limited by that of the thermometer and support structure to about a second. The assembly was placed in a four-stage thermal enclosure[8] which allowed very good control of the thermal environment.

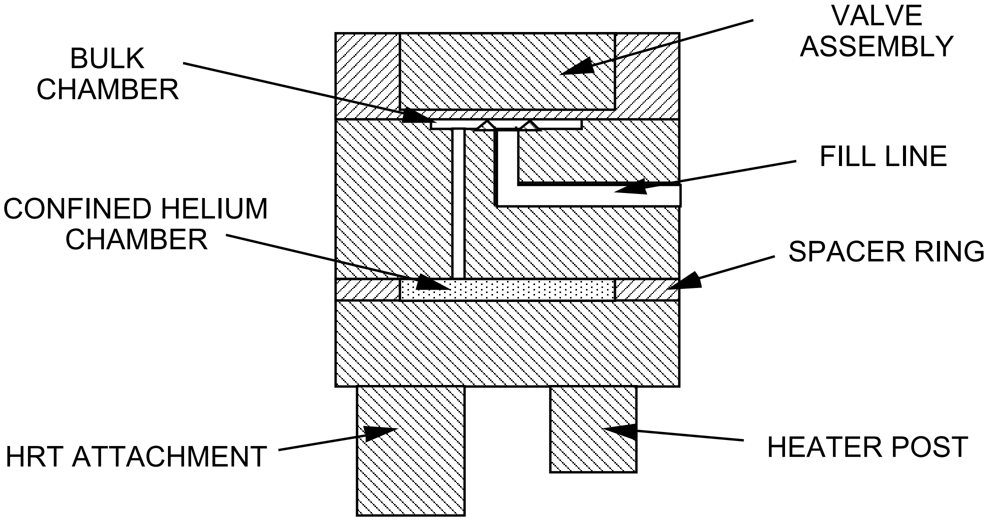

Figure 1: Schematic view of calorimeter for 8-micron sample, as described in the text. (Not to scale.)

For the Anopore measurements a similar calorimeter was used, but the bottom tank was .75 mm high, filled with 17 Anopore disks. The uniformity of the pore diameters in these disks did not approach that of the microchannel plates, but the pores appeared reasonably free from barrel distortion, which appears to be a common problem with Nucleopore holes. Digitized photographs of the surface of a fractured disk were used to determine the distribution of pore sizes. The most probable diameter was found to be 0.26 microns and the standard deviation about 10 %.

RESULTS AND ANALYSIS

The heat capacity results for the two samples showed a sharp spike corresponding to the bulk singularity in the top tank which clearly marked the transition temperature. Because of the finite slope of the lambda line, the hydrostatic pressure head between the two tanks due to the helium in the connecting pipe shifts the bulk transition temperature of the lower tank by about -1.9×10^{-6} K relative to the top. A more rounded peak was also seen which corresponded to the effect of confinement in the lower tank, and contains the information of interest here.

To analyze the confined specific heat signal in detail, we first need to remove the bulk helium contribution. Since the bulk specific heat curve is relatively well known, in principle we could simply subtract out the signal from the upper tank and obtain the lower tank signal directly. However, the exact distribution of the helium between the two tanks was not well known, due to uncertainties in the details of the geometry in the valve area. Instead, we assumed that the lower tank's heat capacity should vary smoothly in the region of the upper tank singularity, since this occurs a few microdegrees above the lower tank's bulk transition point, and subtracted out a range of trial top tank signals. Thus we sought a top tank fraction that removed essentially all traces of the bulk singularity from the combined helium signal. This approach worked well and gave rise to a smoothly rounded confined helium curve.

In the region where the confinement effects are strong the function, f_1, used to model the curve is defined by the scaling relation[9]:

$$C(t,L) - C(t_o, \infty) = L^{\alpha/\nu} f_1(x) \qquad (1)$$

where C is the specific heat, α and ν are the exponents characterizing the divergence of C and ξ respectively, $x = tL^{1/\nu}$ and $t_o = (1.43Å/L)^{1/\nu}$. The function f_1 has been calculated using Monte-Carlo techniques[10] and is shown in figure 2. The corresponding results for the two samples are also shown. It can be seen that there is fair agreement, but there are departures from the model curve in the case of the 8 micron data. For strict scaling to hold, the data sets should collapse onto a universal curve within their uncertainties. It is disappointing that the collapse for the two samples is imperfect.

It is interesting to speculate on the cause of this discrepancy. Comparison of the results with those of Chen and Gasparini[5] shows somewhat better agreement with the Anopore results. We therefore have re-evaluated the 8-micron experiment and its calibration. The primary sources of experimental error that could cause the problem are in the temperature scale calibration and the pore diameter measurement. To collapse the data by adjusting the temperature scale would require about a 50% change in the flux-to-Kelvin scale factor. Reanalysis of the records and comparison with other measurements has confirmed this scale factor to within 1%. To explain the effect as an incorrect pore diameter, the 'correct' size would have to be about 4 microns, in significant disagreement with the manufacturer's specification and our own measurements. Preliminary calculations show that the surface specific heat agrees reasonably well with the predicted value above the transition. Therefore it would appear that the correlation length behavior is as expected, at least for $t > 10^{-5}$ or so. However, this may not be the case for much smaller t. On the other hand, the CHEX results argue for a normal behavior of the correlation length to t ~ 10^{-8} or so in a parallel plate geometry. The effect of the relatively wide distribution of pore sizes with the smaller confining system might play a role. This would bias the Anopore peak towards sharper behavior than predicted, due to non-linearities, but it is hard to make this effect big enough. Another possibility is a difference in the boundary condition for helium in the microchannel plates. How this could be manifested in the presence of the solid monolayer of helium at any wall is difficult to understand. Again the CHEX results would argue against a correlation length dependent effect of this type.

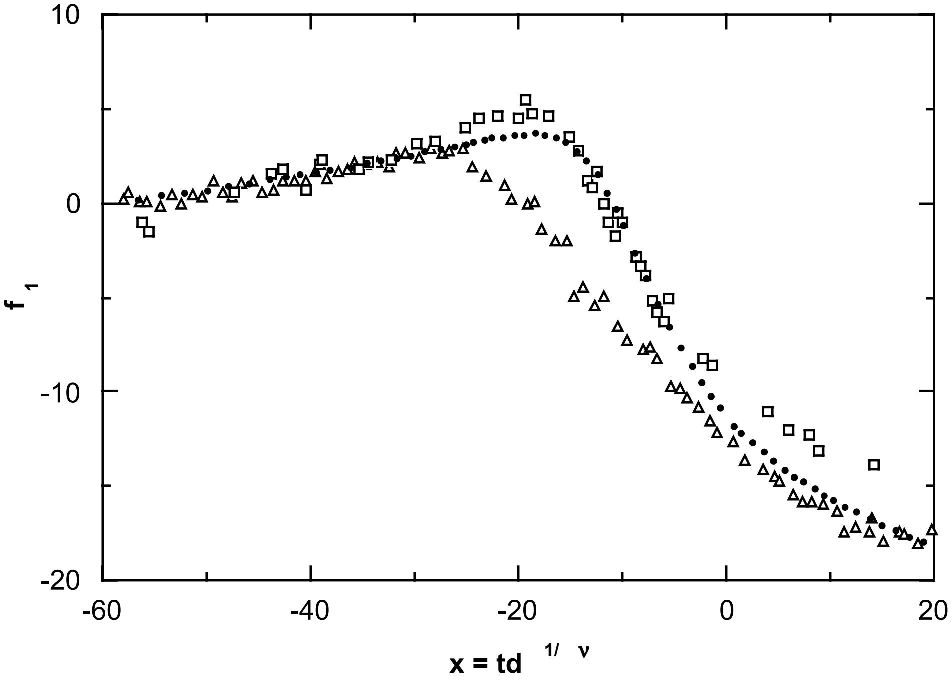

Figure 2: Scaled specific heat of the confined helium as a function of scaled temperature near the transition. Filled circles: Anopore data; squares: Monte-Carlo model; triangles: 8-micron data.

In summary it appears that most aspects of the current theoretical predictions for confinement effects are in reasonable agreement with experiment over a wide range of length scales. However, very near the heat capacity peak for large confining dimensions there is some evidence for rounding in excess of that predicted.

ACKNOWLEDGEMENTS

The work reported here was performed as an adjunct to the CHEX flight program. We wish to thank the Microgravity office of NASA for its support with contracts #JPL-957448, the Graduate Student Researchers Program of NASA for grant # NGT-51153, and D.A. Stricker and S. Kolosvari for assisting with the measurements.

REFERENCES

1. F.M. Gasparini and I. Rhee, Progr. in Low Temp. Phys., **13**, 1 (1992).
2. V. Dohm, Physica Scripta, **T49**, 46 (1993).
3. J.A. Lipa, D.R. Swanson, J.A. Nissen, Z.K. Geng, P.R. Williamson, D.A. Stricker, T.C.P. Chui, U.E. Israelsson and M. Larson, Phys. Rev. Lett., **84**, 4894 (2000).
4. S. Mehta, M.O. Kimball and F.M. Gasparini, J. Low Temp. Phys., **114**, 467 (1999).
5. T.P. Chen and F.M. Gasparini, Phys. Rev. Lett. **40**, 331 (1978).
6. See, for example, J. A. Lipa, B. C. Leslie and T. C. Wallstrom, Physica ,**107 B**, 331 (1981), or T.C.P. Chui, D.R. Swanson, M.J. Adriaans, J.A. Nissen, and J.A. Lipa, Phys. Rev. Lett. **69**, 3005 (1992).
7. Microchannel plates, made by Galileo Electro-Optics Corp., Sturbridge, Mass.
8. J.A. Lipa and T.C.P. Chui, Phys. Rev. Lett. **51**, 2291 (1983).
9. R. Schmolke, A. Wacker, V. Dohm and D. Frank, Physica B, **165** & **166**, 575 (1990).
10. N. Schultka and E. Manousakis, Phys. Rev. Lett., **75**, 2710 (1995).